

https://dspace.org/

The Positioning of electromagnetic near field hotspots within a resonant cavity for applications in microwave thermal ablation

Young, Graeme Robin

2022
https://hdl.handle.net/10539/34142

Downloaded from a DSpace repository. https://dspace.org/



WITS
UNIVERSITY

The Positioning of Electromagnetic Near Field Hotspots within a Resonant Cavity for Applications in Microwave Thermal Ablation

Author:
Graeme R. Young

A dissertation submitted to the Faculty of Engineering and the Built Environment, University of the Witwatersrand, Johannesburg, in fulfilment of the requirements for the degree of Master of Science in Engineering.

Johannesburg, 2021

Declaration

I declare that this dissertation is my own unaided work. It is being submitted to the Degree of Master of Science to the University of the Witwatersrand, Johannesburg. It has not been submitted before for any degree or examination to any other University.



6th day of December , 2021

Abstract

The investigation into moving electromagnetic near field hotspots inside a resonant cavity is presented. The investigation is focused on providing an alternative approach to thermal ablation of tumours, by inducing a hotspot over a tumour instead of using an interstitial antenna. The methodology comprised comparing various electromagnetic solvers, verifying the simulation techniques, characterising the resonance within a rectangular resonant cavity, and attempting to control the movement of its hotspots by introducing a phase shift between its sources and modifying their frequency. The effects of dielectric media of the field were also investigated. It was determined that incremental frequency shifts only progressively moved the system's hotspots between 2.6 and 2.7 GHz and phase shifting only worked between 2.55 and 2.7 GHz when the feeds were on opposite walls. At the system's eigenfrequencies, no pattern change was evident, indicating that when the chamber was resonating, the field pattern was set. Further, it was determined that the bandwidth of the characteristic modes of the system were very narrow, such that the addition of dielectric material completely altered the resonance of the system and the eigenfrequencies shifted. Therefore, the application of this method to thermal ablation, which requires high precision, accuracy and control, was deemed impractical. Future recommendations include using adjustable cavity geometry and directive microwave sources to design for specific field patterns. Additionally, it is recommended to investigate the validity of the 'reverse problem' to create a specific current distribution around the resonant cavity. This is reminiscent of the three-dimensional Green's Theorem, which would induce the desired hotspot pattern from the surrounding current distribution.

Acknowledgements

I wish to gratefully acknowledge:

My supervisors, Prof. Alan Clark and Prof. David Rubin, who were always available for consultation, able to keep me focused, who called a spade a spade when necessary and who provided invaluable feedback and encouragement.

The University of the Witwatersrand for supplying me with the resources I needed to conduct this investigation, particularly the FEKO license, which was paramount to the research.

To Dassault Systèmes for providing a student edition of CST Studio Suite, an integral program throughout the investigation; and EMWorks for providing me with a student evaluation of HFWorks.

My friends and family, for supporting me through this process.

Contents

Declaration i

Abstract ii

Acknowledgements iii

Contents vii

List of Figures x

List of Tables xi

List of Symbols xii

List of Abbreviations xiv

1 Introduction 1

1.1 Problem Statement . . . 1
1.2 Research Question . . . 2
1.3 Methodology Description . . . 3
1.4 Organization of Dissertation . . . 3

2 Background 4

2.1 Thermal Ablation . . . 4
2.1.1 Biophysics . . . 4
2.1.2 Current Procedures . . . 5
2.2 Relevant Electromagnetics . . . 7
2.2.1 Electromagnetic Waves, Fields and Radiation . . . 7
2.2.2 Electromagnetic Spectrum . . . 8
2.2.3 Antennas . . . 8
2.2.4 Impedance . . . 10

2.2.5 Near and Far Fields . . . 11
2.2.6 Array Theory . . . 13
2.2.7 Resonance and Resonant Cavities . . . 14
2.3 Microwaves . . . 15
2.3.1 Microwave Heating . . . 15
2.3.2 Dielectric Influence . . . 16
2.3.3 Microwave Ovens . . . 17
2.4 Electromagnetic Solvers . . . 17
2.4.1 Maxwell's Equations . . . 17
2.4.2 Method of Moments . . . 19
2.4.3 Fast Multipole Method . . . 19
2.4.4 Finite Element Method . . . 20
2.4.5 Finite Difference Time Domain . . . 20
2.4.6 Finite Integration Technique . . . 21
2.4.7 Eigenmode Expansion . . . 21
2.4.8 Modelling Software . . . 21

3 Methodology **26**
3.1 Software Testing . . . 26
3.1.1 Benchmark Model . . . 27
3.1.2 Results and Deliverables . . . 27
3.2 Verification . . . 28
3.2.1 Microwave Oven Model . . . 29
3.2.2 Actual Field . . . 29
3.2.3 Operating Frequency . . . 30
3.2.4 Simulated Field . . . 30
3.2.5 Results Comparison . . . 31
3.3 Cavity Characterisation . . . 31
3.3.1 Ideal Rectangular Cavity . . . 32
3.3.2 Waveguide Resonant Frequency . . . 33
3.3.3 Cavity Resonant Frequency . . . 33
3.3.4 Dielectric Influence . . . 34
3.4 Field Manipulation . . . 34
3.4.1 Frequency Shifting . . . 35
3.4.2 Phase Shifting . . . 35
3.4.3 Bandwidth . . . 36
3.5 Software Summary . . . 36

3.5.1 Benchmark . . . 36
3.5.2 Verification . . . 36
3.5.3 Characterisation . . . 37
3.5.4 Frequency Sweeping . . . 37
3.5.5 Phase Shifting . . . 38
3.5.6 Comparison . . . 38

4 Results **39**
4.1 Software Testing . . . 39
4.1.1 Comparison . . . 39
4.2 Verification . . . 41
4.2.1 Microwave Oven . . . 41
4.2.2 Microwave Oven Fields . . . 42
4.2.3 Operating Frequencies . . . 42
4.2.4 Simulated Fields . . . 45
4.2.5 Comparison . . . 46
4.2.6 Error . . . 47
4.2.7 Conclusion . . . 48
4.3 Cavity Characterisation . . . 49
4.3.1 Waveguide Resonator . . . 49
4.3.2 Cavity Resonance . . . 50
4.3.3 Bandwidth . . . 52
4.3.4 Dielectric Influence . . . 56
4.4 Hotspot Manipulation: Frequency Shifting . . . 60
4.4.1 2.6 - 2.7 GHz . . . 60
4.5 Hotspot Manipulation: Phase Shifting . . . 63
4.5.1 Same Face . . . 63
4.5.2 Adjacent Faces . . . 66
4.5.3 Opposite Faces . . . 69
4.6 Conclusion . . . 72

5 Conclusion **74**
5.1 Summary . . . 74
5.2 Research Questions . . . 75
5.3 Future Recommendations . . . 76
5.4 Conclusion . . . 77

References **78**

A NEC2 Hotspot Plotter **83**
A.1 Introduction . . . 83
A.2 NEC2 . . . 83
A.3 Working . . . 84
A.4 Interface . . . 84
A.5 I/O . . . 85
A.6 Future Recommendations . . . 86
A.7 Conclusion . . . 86
References . . . 86

B Comparison of Electromagnetic Field Solvers **87**
B.1 Introduction . . . 87
B.2 Licences and Capability . . . 87
B.3 Solver Methods . . . 88
B.4 Computer Properties . . . 89
B.5 Simulation Parameters . . . 90
B.6 Comparison Metrics . . . 91
B.7 Solution Comparison . . . 92
B.7.1 Frequency Sweep . . . 92
B.7.2 Characteristic modes . . . 93
B.8 Simulation Time . . . 99
B.9 Conclusion . . . 100
References . . . 100

Bibliography **101**

List of Figures

2.1 Electromagnetic Wave. 7
2.2 Electromagnetic Spectrum. 8
2.3 Near Field vs Far Field. 12
2.4 Near (left) and Far (right) field radiation patterns. 13
2.5 Radiation Pattern of Broadside and End-fire arrays. 14
2.6 The Hybridisation of the FEKO Solvers for their Respective Applications. 23

3.1 Waveguide Orientations. Images adapted from CST Studio. 35

4.1 Comparison of the Centre Horizontal Plane of the Benchmark Model. . . 39
4.2 Comparison of the 3D Iso-Surface of the Benchmark Model. 41
4.3 The Microwave Geometry and Simulated Hotspots at 2.45 GHz in FEKO. Images exported by FEKO. 42
4.4 The near fields inside the microwave oven as shown on thermal paper. . . 43
4.5 Process Binary Images of the Measured Near Field. 43
4.6 Logical Operations on the Binary Images. 43
4.7 Microwave Leakage with a Glass of Water. 44
4.8 Microwave Leakage with a Sheet of Polystyrene. 45
4.9 Simulated Operational Fields inside the Microwave Oven for 2.4–2.5 GHz with Styrofoam as a Dielectric. 46
4.10 Simulated Operational Fields inside the Microwave Oven for 2.33–2.35 GHz with Polystyrene as a Dielectric. 46
4.11 Comparison of the Simulated and Measured Binary Images. 47
4.12 Electric Field from the Resonant Study of the Bounded WR340 Waveguide. 50
4.13 Excitation of a Bounded WR340 Waveguide with Different Frequencies. . 50
4.14 E-Field Pattern of the Cavity at 2.386 GHz, exhibiting Mode TE_{104}. . . 52
4.15 E-Field Pattern of the Cavity exhibiting Mode TE_{303}. 52
4.16 E-Field Pattern of the Cavity at 2.651 GHz, exhibiting Mode TE_{122}. . . 53
4.17 Maximum E-field value across the Frequency Range in CST Studio. . . . 54

4.18 Accepted Power across the Frequency Range in CST Studio. 54
4.19 Radiated Power across the Frequency Range in FEKO. 54
4.20 Radiated Power at the Characteristic Modes in FEKO. 55
4.21 VSWR of Cavity with Water in CST Studio. 56
4.22 Accepted Power of Cavity with Water in CST Studio. 57
4.23 Maximum Electric Field of Cavity with Water in CST Studio. 57
4.24 Comparison of Near Fields With and Without Water in the Cavity. 59
4.25 Longitudinal Contour of Near Field Pattern at 2.6 and 2.7 GHz. 60
4.26 Plot of Field Magnitude through Top Hotspot from 2.6 GHz to 2.7 GHz. . 61
4.27 Position of Maximum along Z-Axis from Waveguide against Frequency. . . 61
4.28 Position of First Null along Z-Axis from Waveguide against Frequency. . . 62
4.29 Position of Second Null along Z-Axis from Waveguide against Frequency. 62
4.30 The Effect of Feed Phase at 2.3861 GHz for the Same Face Model. 64
4.31 The Effect of Feed Phase at 2.4478 GHz for the Same Face Model. 64
4.32 The Effect of Feed Phase at 2.5889 GHz for the Same Face Model. 65
4.33 The Effect of Feed Phase at 2.6513 GHz for the Same Face Model. 65
4.34 The Effect of Feed Phase at 2.419 GHz for the Same Face Model. 65
4.35 The Effect of Feed Phase at 2.501 GHz for the Same Face Model. 66
4.36 The Effect of Feed Phase at 2.635 GHz for the Same Face Model. 66
4.37 The Effect of Feed Phase at 2.387 GHz for the Adjacent Face Model. . . . 67
4.38 The Effect of Feed Phase at 2.455 GHz for the Adjacent Face Model. . . . 67
4.39 The Effect of Feed Phase at 2.588 GHz for the Adjacent Face Model. . . . 67
4.40 The Effect of Feed Phase at 2.644 GHz for the Adjacent Face Model. . . . 67
4.41 The Effect of Feed Phase at 2.385 GHz for the Adjacent Face Model. . . . 68
4.42 The Effect of Feed Phase at 2.421 GHz for the Adjacent Face Model. . . . 68
4.43 The Effect of Feed Phase at 2.635 GHz for the Adjacent Face Model. . . . 69
4.44 The Effect of Feed Phase at 2.387 GHz for the Opposite Face Model. . . . 70
4.45 The Effect of Feed Phase at 2.4558 GHz for the Opposite Face Model. . . 70
4.46 The Effect of Feed Phase at 2.6535 GHz for the Opposite Face Model. . . 70
4.47 The Effect of Feed Phase at 2.588 GHz for the Opposite Face Model. . . . 70
4.48 The Effect of Feed Phase at 2.421 GHz for the Opposite Face Model. . . . 71
4.49 The Effect of Feed Phase at 2.499 GHz for the Opposite Face Model. . . . 71
4.50 The Effect of Feed Phase at 2.635 GHz for the Opposite Face Model. . . . 72

A.1 Application Interface with Loaded Model and Plotted Data. 85

B.1 Comparison of CST Studio and FEKO at 2.2 GHz. 92
B.2 Comparison of CST Studio and FEKO at 2.45 GHz. 92

B.3 Comparison of CST Studio and FEKO at 2.7 GHz. 93
B.4 Radiated Power for Mode 1 in FEKO 93
B.5 Radiated Power for Mode 2 in FEKO 94
B.6 Accepted Power for Mode 1 in CST 95
B.7 Accepted Power for Mode 2 in CST 95
B.8 Accepted Power for Time Domain Solver in CST 96
B.9 Near Field Pattern for Mode 1 in FEKO. 97
B.10 Near Field Pattern for Mode 1 in CST. 97
B.11 Near Field Pattern for Mode 2 in FEKO. 97
B.12 Near Field Pattern for Mode 2 in CST. 98

List of Tables

2.1 Characterisation of some of the ionising and non-ionising regions of the electromagnetic spectrum and their process of interacting with matter. . . 9
2.2 Dissipation factors of various solvents and materials at 3 GHz and 25° C. 16
2.3 Maxwell's Equations in Differential and Integral Form 18

3.1 Dimensions of the basic rectangular cavity. 27
3.2 Characteristics of the WR340 waveguide. 32
3.3 Dimensions of the ideal rectangular cavity. 33
3.4 Summary of the Software Used for the Benchmark Section. 37
3.5 Summary of the Software Used for the Verification Section. 37
3.6 Summary of the Software Used for the Characterisation Section. 37
3.7 Summary of the Software Used for the Frequency Sweeping Section. . . . 38
3.8 Summary of the Software Used for the Phase Shifting Section. 38
3.9 Summary of the Software Used for the Software Comparison. 38

4.1 Radiated Power and Mean $\tilde{E}$ Field Comparison. 40
4.2 Resonant Modes of the WR340 Waveguide. 49
4.3 Resonant Modes of Cavity between 2.2 and 2.7 GHz 51
4.4 Frequencies at which Phase Shift was Examined. 63

B.1 Dimensions of ideal rectangular cavity. 90
B.2 Solver Times of CST Studio and FEKO. 99

List of Symbols

ρ	tissue density [kg·m^{-3}]
C_{p}	tissue specific heat capacity [J·kg^{-1}·K^{-1}]
T	temperature [K]
k	thermal conductivity [W·m^{-1}·K^{-1}]
Q_{h}	heat flux of the source of ablation [W·m^{-1}]
Q_{m}	metabolic heat flux [W·m^{-1}]
$Q_{\mathrm{p}'}$	blood perfusion heat flux [W·m^{-1}]
λ	wavelength [m]
f	frequency [Hz]
h	Planck's constant
G	antenna gain [dBi]
D	antenna directivity, essentially gain [dBi]
η	antenna efficiency
P_{rad}	power radiated by the antenna [W]
P_{in}	power input to the antenna [W]
$\theta^{\circ}_{\mathrm{HP}}$	half power beam angle in the θ direction [degrees]
$\phi^{\circ}_{\mathrm{HP}}$	half power beam angle in the ϕ direction [degrees]
A_e	effective aperture [m^2]
R	radial distance from the source [m]
L	largest physical dimension of antenna [m]
E	electric field strength [V·m^{-1}]
J	current density [A·m^{-1}]
σ	electric conductivity [S·m^{-1}]
μ_0	magnetic permeability of free space
ϵ''	dielectric loss factor
ϵ_0	permittivity of free space
ϵ'	dielectric constant
ϵ^*	relative complex permittivity

$\mathbf{E}$	electric field intensity vector [$\mathrm{V{\cdot}m^{-1}}$]
$\mathbf{B}$	magnetic flux density vector [$\mathrm{Wb{\cdot}m^{-2}}$ or T]
$\mathbf{H}$	magnetic field intensity vector [$\mathrm{A{\cdot}m^{-1}}$]
$\mathbf{D}$	electric flux density vector [$\mathrm{C{\cdot}m^{-2}}$]
$\mathbf{J}$	electric current density vector [$\mathrm{A{\cdot}m^{-2}}$]
ρ_v	electric charge density [$\mathrm{C{\cdot}m^{-2}}$]
$f_{c_{mn}}$	cut-off frequency of mode mn [Hz]
$k_{c_{mn}}$	wavenumber corresponding to mode mn
a	length of waveguide in **H** direction, or width [m]
b	length of waveguide in **E** direction, or height [m]
c	speed of light
f_{mnl}	cavity resonant frequency for mode TE_{mnl} [Hz]
k_{mnl}	wave number corresponding to mode TE_{mnl}

List of Abbreviations

AMP	Antenna Modelling Program
BEM	Boundary Element Method
BEP	Bidirectional Eigenmode Propagation
CAD	Computer Aided Design
CMA	Characteristic Mode Analysis
CPU	Central Processing Unit
EM	Electromagnetic
EME	Eigenmode Expansion
FDTD	Finite Difference Time Domain
FEM	Finite Element Method
FIT	Finite Integration Technique
FMM	Fast Multipole Method
FT	Fourier Transform
GPU	Graphics Processing Unit
HF	High Frequency
HIFU	High Intensity Focused Ultrasound
HPBW	Half Power Bandwidth
ISM	Industrial, Scientific and Medical
LA	Laser Ablation
LE-PO	Large Element Physical Optics
LPDA	Log Periodic Dipole Array
MLFMM	Multilevel Fast Multipole Method
MOD	Model Order Reduction
MoM	Method of Moments
MRI	Magnetic Resonance Imaging
MWA	Microwave Ablation
NEC	Numerical Electromagnetic Code
PEC	Perfect Electric Conductor

PO	Physical Optics
RAM	Random Access Memory
RF	Radio Frequency
RFA	Radio Frequency Ablation
RL-GO	Ray Launching Geometric Optics
SAR	Specific Absorption Rate
TE	Transverse Electric
TEM	Transverse Electromagnetic
TLM	Transmission Line Matrix
UTD	Uniform Theory of Diffraction
VNA	Vector Network Analyser
VSWR	Voltage Standing Wave Ratio

Chapter 1

Introduction

Thermal ablation of a tumour is a clinical method of neoplastic tissue destruction by inducing extreme local hyperthermia or hypothermia [1]. The procedure is like surgery in the sense that it targets the whole tumour and a small margin of regular tissue surrounding the tumour. Instead of the tissue being surgically removed, requiring cutting the patient open, the tissue is killed and then reabsorbed by the body over some time following the procedure [1].

Some sources of clinical hyperthermic ablation, such as microwave and radio frequency, use needle-like interstitial devices, which are physically inserted into the tumour, as the heat delivery mechanism. For microwave ablation, microwaves radiate from the needle-like antenna. Microwaves propagate through all types of human tissue and induce the most heat in tissues rich with polar molecules such as water [1]. Because tumours are usually quite water-dense, microwave ablation can be quite effective at destroying them. The inserted interstitial antenna, when energised, creates an electromagnetic field at microwave frequency surrounding it, which induces heat in the tissue over time. From an electromagnetic perspective, the antenna is fed with a signal at microwave frequency. The antenna resonates and radiates electromagnetic radiation according to the specific antenna's far-field radiation pattern. A simple monopole antenna is often used, resulting in a largely omnidirectional pattern, hence inducing a relatively even pocket of heat or hotspot over the desired location.

1.1 Problem Statement

The current microwave ablation method, while being less invasive than open surgery to remove tumours, is still an invasive procedure, as a device must be inserted into the body

to deliver the microwave effect to the needed area. As such, the procedure is usually relatively superficial in areas that are easily accessible percutaneously, such as the liver, the most common site in the human anatomy for microwave thermal ablation [2].

The efficacy of the procedure is therefore limited to the location and percutaneous accessibility of the patient's tumour. If it is hidden behind organs or other structures, the procedure becomes difficult and ineffective. Additionally, concerns about general surgery are not circumvented, for instance, poor clotting factors or allergies to anaesthesia etc. on the patient's behalf. Some methods of ablation, such as High-Intensity Focused Ultrasound (HIFU) eliminate these issues, however, HIFU has been shown to have various problems associated with trying to ablate tumours, such as skin burns, acoustic impedance from the lungs and heart, particularly in the thoracic area, and inefficient ultrasound transduction through bone [3].

The problem with microwave ablation arises from the need to insert an interstitial antenna into the desired tumour. The problem would be mitigated if an electromagnetic hotspot could be induced over a tumour without the need for the inserted antenna. The process could be accomplished using electromagnetic fields at microwave frequencies. At these frequencies, the radiation isn't as easily steered as with the much higher frequency X-band radiation therapy. Additionally, the size of the antenna required to narrow a beam towards a point as small as a tumour becomes impractically large. Therefore, this investigation is a resonance study, looking at the electromagnetic near fields inside a resonant cavity. Currently, there is no method for controlling the position of a microwave frequency hotspot within a resonant cavity.

1.2 Research Question

The above problem statement leads to the following research question.

"Can the position of an electromagnetic hotspot at microwave frequencies be controlled consistently and feasibly within a resonant cavity?"

This research question can be broken down into a series of sub-questions as follows:

- Can a microwave frequency electromagnetic hotspot be effectively modelled in a resonant cavity?
- Can the resonance and field pattern of the model be changed by adding another microwave source?
- Can altering the phase and frequency of each source change the electromagnetic

field pattern within the resonant cavity and hence, change the hotspot positions?

- Is the change of hotspot position consistent and feasible for the application of clinical microwave thermal ablation?

1.3 Methodology Description

The methodology used to answer the research questions is divided into four sections. Software testing, where the software packages used are tested against each other for unanimity and for their ability to effectively handle resonance problems; software verification, where simulated data is compared to data acquired through real-world testing to establish accuracy in resonance problems; characterisation of the established field in simulation to quantify characteristic modes and resonant frequencies; and field manipulation, where feed frequency and phase differences are introduced in an attempt to control the position of the hotspots inherent to a field pattern.

1.4 Organization of Dissertation

The rest of the dissertation is organized as follows. Chapter 2 pertains to the literature review and background information relevant to this investigation. Chapter 3 discusses the detailed methodology used to answer the research questions. Chapter 4 contains the results obtained and conclusion hence drawn. The conclusion is discussed in Chapter 5, along with future recommendations and a review of the research questions.

Chapter 2

Background

This chapter discusses the types of thermal ablation and their underlying physics. Electromagnetic theory on near field problems, the microwave frequency spectrum and its interactions with dielectric tissue are discussed, along with field manipulation methods including antenna and array theory. Additionally, the solver methods and modelling software to be used in the investigation, including background into how each solver methods works and their respective benefits and shortcomings, is presented.

2.1 Thermal Ablation

2.1.1 Biophysics

Thermal ablation is a method of destroying tissue by inducing hyper or hypothermia in the tissue, as a substitute for open surgery. This is a transient thermal heat transfer problem that can be described using Fourier's heat equation. Penne produced a biothermal formulation of Fourier's heat equation [4] as follows:

$$\rho C_{\mathrm{p}} \frac{\partial T}{\partial t} = k\nabla^2 T + Q_{\mathrm{h}} + Q_{\mathrm{m}} + Q_{\mathrm{p}'} \tag{2.1}$$

Where:

ρ = tissue density [kg·m^{-3}]
C_{p} = tissue specific heat capacity [J·kg^{-1}·K^{-1}]
T = temperature [K]
k = thermal conductivity [W·m^{-1}·K^{-1}]
Q_{h} = heat flux of the source of ablation [W·m^{-1}]
Q_{m} = metabolic heat flux [W·m^{-1}]
$Q_{\mathrm{p}'}$ = blood perfusion heat flux [W·m^{-1}]

High volume blood vessels in the target area can create a heat sink for the thermal energy, which *Equation (2.1)* does not account for, however, for nearby vessels with a diameter of approximately 3 mm or less, the formulation holds [5].

2.1.2 Current Procedures

There are currently many implementations of clinical thermal ablation, the most common of which being Radio Frequency Ablation (RFA), Microwave Ablation (MWA), Cryoablation, Laser Ablation (LA) and High Intensity Focused Ultrasound (HIFU). All except HIFU use interstitial antenna devices to deliver the thermal energy and all are often accompanied by an image guidance technique, such as magnetic resonance imaging (MRI) [6].

Radiofrequency

RFA, one of the most used techniques, utilises an electrode; which is connected to a radio wave generator, operating at radio frequency, and inserted directly into the target tumour, while a reference electrode is often placed on the subject's skin [1]. This is known as unipolar operation. The bipolar operation is sometimes used, where the two electrodes are placed on either side of the target tissue. When an electric current at radiofrequency is applied through the electrode, the surrounding tissue heats up as a result of resistive losses as current travels towards the reference electrode, which excites the ionic molecules in the tissue through which it passes [6].

Cryoablation

Cryoablation uses the Joule-Thomson effect, which describes gas under high pressure being forced through a porous plug or valve into an area of low pressure, causing the gas to expand and cool down [7]. This method requires a probe, which carries the required gas internally, to be inserted into the target tissue. The standard procedure utilises argon gas to cool the tumour down (to as low as -160° C) by forming an ice ball, which also clearly defines the ablation margins, and helium gas to warm the probe up again. Typically, the procedure comprises multiple cycles of freeze and thaw in the area, after which the probe is removed [6].

Laser

LA is performed by directly exposing the tissue to laser energy via a transport medium. The laser provides a monochromatic light, the wavelength of which determines the laser properties and tissue interactions, which is transported, usually through an optical fibre,

directly to the ablation site. The absorption of the laser energy by the tissue is converted to heat, which creates a temperature gradient through the surrounding tissue. The treatment can be administered in continuous mode, where low laser power is used over a longer period, or pulsed mode, where high laser power is administered intermittently [8].

Focused Ultrasound

Ultrasound energy can be delivered both internally, using interstitial devices, like RFA and MWA, or using external transducers. This makes ultrasound a very promising field. HIFU is a process that requires only external transducers, lending the ability to ablate tissue truly non-invasively. It relies on multiple ultrasonic beams converging to a focal point of heating [1]. The ablation zone is usually tiny, about the size of a grain of rice, and the process for destroying a full tumour involves overlapping many of these areas of focus to cover the entire volume of the tumour [1]. Because of this, HIFU can often take a matter of hours to complete, instead of the handful of minutes needed by the other invasive techniques, and hence, the ablation site must generally be in easily accessible areas that are not subject to any substantial movement over time; from breathing, for instance. HIFU has also been shown to have other associated problems in practice, such as skin burns and inefficient signal transduction through dense bone [3].

Microwave

MWA uses the microwave effect to induce heat in the target tissue. Like RFA, a device is inserted into the target tumour, however, in this instance, it is a microwave antenna. Electromagnetic microwaves radiate out from the interstitial antenna, creating a hotspot around the device and interacting with the surrounding tissue. Tissue containing polar molecules such as water are most affected by this method of heating, as the microwave heating effect causes the molecules to vibrate [6]. Additionally, microwave frequency electromagnetic waves propagate through all types of human tissue, in contrast to RF ablation, which relies on the impedance of the tissue for current propagation. Therefore, the entire ablation zone undergoes heating if it contains polar molecules. The main difference between RFA and MWA is the frequency. RFA operates at radio frequency and MWA operates at microwave frequency, which is much higher. Therefore, the tissues of the human body are much larger in terms of wavelength for RFA when compared to MWA. Because of this, RFA relies largely on current flow between the electrodes, whereas the probe used in MWA becomes an actual antenna instead of an electrode.

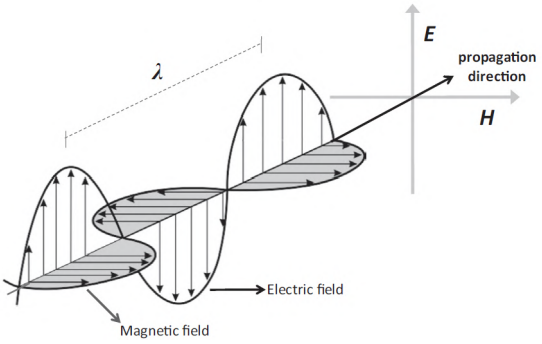

Figure 2.1: Electromagnetic Wave. Adapted from [11].

2.2 Relevant Electromagnetics

2.2.1 Electromagnetic Waves, Fields and Radiation

Microwaves are a form of electromagnetic radiation. Unlike mechanical waves, like sound, they can radiate through a vacuum, not requiring a medium to carry them, and through transmission lines, as a Transverse Electromagnetic (TEM) wave [9]. Electromagnetic waves have two components, Electric field (**E**) and Magnetic field (**H**), which act perpendicular to each other, as shown in *Figure 2.1*. These waves are characterised by their main three properties, being frequency, velocity and electric field strength. The velocity at which electromagnetic waves propagate in a vacuum, or in 'free space', is denoted by the symbol c, which is $\approx 3 \times 10^8$ m·s^{-1}, also called the speed of light in free space [10]. A fundamental factor of electromagnetic waves is its frequency and wavelength, which are related by the velocity of the wave, given in *Equation (2.2)* and the energy it carries, given by the Planck relation, *Equation (2.3)*. Electric or magnetic field strength simply refers to the magnitude of the field, often given in volts per meter (V/m) and amperes per meter (A/m).

$$\lambda = \frac{c}{f} \tag{2.2}$$

$$E = hf \tag{2.3}$$

Where:

λ = wavelength [m]

f = frequency [Hz]

h = Planck's constant $\approx 6.63 \times 10^{-34}$ m^2·kg·s^{-1}

Electromagnetic fields are simply the combination of interconnected electric and magnetic fields. Radiation is simply the fluctuation of these fields in space [12].

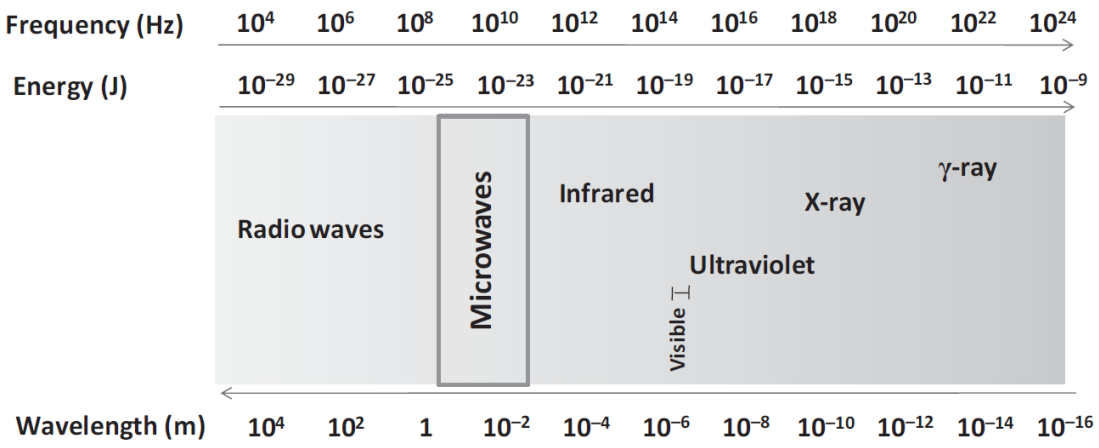

Figure 2.2: Electromagnetic Spectrum. Adapted from [11].

2.2.2 Electromagnetic Spectrum

The frequencies at which electromagnetic waves can propagate are limitless. The electromagnetic spectrum refers to the phenomena that occur as a result of an electromagnetic field oscillating within specific ranges of frequencies across the continuum of frequencies [10]. *Figure* 2.2 shows some phenomena that occur at various wavelengths. It is noteworthy that as the frequency of the wave increases, so too does the wave energy. The microwave spectrum is generally accepted as occurring between the wavelengths of 30 cm to 3 mm, or frequencies of 1 GHz to 100 GHz. The typical frequency at which microwave ovens and, incidentally, Industrial, Scientific and Medical (ISM) devices operate is 2.45 GHz, corresponding to a wavelength of $\approx$ 122 mm.

Most of the electromagnetic spectrum that we experience in our daily lives, including irradiation from the sun, forms part of the non-ionising spectra of frequencies, those below the X-ray frequencies, which are usually regarded as 'harmless'. Radiation associated with nuclear fission is ionising radiation, consisting of electromagnetic waves at a very high frequency (X-ray and above) and alpha and beta particles, resulting from the decay of radioactive material. These waves are generally highly penetrating and can cause tissue damage when absorbed [13]. It is important to note that microwave spectral frequencies are not considered ionising. *Table* 2.1 shows the spectral characteristics of some types of ionising and non-ionising radiation [11].

2.2.3 Antennas

An antenna is a structure that radiates electromagnetic energy. An *isotropic* antenna radiates electromagnetic energy equally in all directions. A useful property of antennas is directivity, which means the field is *directed*. Directivity, D is generally analogous with

Table 2.1: Characterisation of some of the ionising and non-ionising regions of the electromagnetic spectrum and their process of interacting with matter.

Radiation Type	**Frequency (Hz)**	**Energy (J)**	**Process**
Ionising			
γ-ray	$> 10^{19}$	$> 6.6 \cdot 10^{-15}$	Ionisation and nuclear effects
X-ray	$10^{16} - 10^{19}$	$6.6 \cdot 10^{-18}$ to $6.6 \cdot 10^{-15}$	Ionisation
Non-ionising			
Ultraviolet	10^{14} to 10^{16}	$6.6 \cdot 10^{-20}$ to $6.6 \cdot 10^{-18}$	Electronic transitions
Visible light	10^{14}	$6.6 \cdot 10^{-20}$	Electronic transitions
Infrared	10^{11} to 10^{14}	$6.6 \cdot 10^{-23}$ to $6.6 \cdot 10^{-20}$	Rotation of molecules and vibration of flexible bonds
Microwaves	10^{9} to 10^{11}	$6.6 \cdot 10^{-25}$ to $6.6 \cdot 10^{-23}$	Rotation of molecules

antenna gain, G, being dependant on antenna efficiency, as shown in *Equation* (2.4) [14]. For practical purposes, the efficiency, η, of an antenna is usually assumed to be 1, meaning Gain and Directivity are equivalent. This is a general assumption for high frequency (HF) and up.

$$G = \eta D \tag{2.4}$$

$$\eta = \frac{P_{rad}}{P_{in}} \tag{2.5}$$

Where:

G = antenna gain [dBi]
D = antenna directivity, essentially gain [dBi]
η = antenna efficiency
P_{rad} = power radiated by the antenna [W]
P_{in} = power input to the antenna [W]

The higher the gain in a particular direction, the more the field is directed in that solid angle, instead of radiated omnidirectionally [14]. The field pattern is manipulated by the antenna's geometric characteristics, to radiate more energy in a certain direction than in others. There are limitations on this, however. The approximation in *Equation* (2.6) [14]

shows the Half-Power Beamwidth (HPBW) of an antenna's radiation pattern compared to its gain. Here, the gain is absolute, not in logarithmic form.

$$G \approx \frac{36000}{\theta^{\circ}_{\mathrm{HP}} \phi^{\circ}_{\mathrm{HP}}} \tag{2.6}$$

Where:

$\theta^{\circ}_{\mathrm{HP}}$ = half power beam angle in the θ direction [degrees]

$\phi^{\circ}_{\mathrm{HP}}$ = half power beam angle in the ϕ direction [degrees]

This shows that the more concentrated the radiation must be, or the smaller the HPBW, the higher the gain of the antenna must be. *Equation (2.7)* [14] shows that the effective aperture of an antenna, or the space it occupies, is directly proportional to the gain of the antenna. Therefore, an antenna that could produce a radiation pattern that focuses a beam to a small enough HPBW to affect a tumour and not its surrounding tissue would require a very large gain, requiring a very large antenna.

$$A_e = \frac{G\lambda^2}{4\pi} \tag{2.7}$$

Where:

A_e = effective aperture [m^2]

For these relationships to hold, the receiver and source must be sufficiently far away, in the so-called *far field*, discussed in *Section 2.2.5*.

2.2.4 Impedance

Antenna impedance plays a large role in the operation of antennas and electromagnetic devices. An impedance mismatch involving an antenna ultimately results in signal attenuation. Therefore, antennas are ideally used in their *impedance bandwidth*, the range of frequencies where their impedance is deemed acceptable for enough energy to be radiated by the antenna instead of reflected. A common metric for quantifying this impedance bandwidth is the voltage standing wave ratio (VSWR) of an antenna. When impedances are not matched, reflection occurs and standing waves are set up so not all available power is transferred [14]. The measure of the impedance mismatch is quantified by ρ, the voltage reflection coefficient, given in *Equation (2.8)*. The lower the reflection, the better the power transmission.

$$\rho = \frac{Z_2 - Z_1}{Z_2 + Z_1} \tag{2.8}$$

VSWR is the more common way of stating impedance mismatch. It is related to the reflection coefficient as follows:

$$VSWR = \frac{1 + |\rho|}{1 - |\rho|} \tag{2.9}$$

In terms of the generated standing waves resulting from an impedance mismatch, VSWR can be calculated by dividing the maximum voltage of the envelope by the minimum voltage: V_{max}/V_{min}. VSWR is often used to describe the impedance bandwidth of an antenna. By general rule, if the VSWR ≤ 2, the antenna is considered matched and the range of frequencies where the VSWR is below 2 is the impedance bandwidth.

2.2.5 Near and Far Fields

The area surrounding an electromagnetic source, such as an antenna, is broken up into three regions: the reactive near field, the radiative near field and the far field. For small antennas, this is often approximated to a single near field far field transition point at $\lambda/2\pi$. This approximation stems from the E_θ component of the electric field radiated by an antenna. It contains three components based on $1/r^3$, $1/r^2$ and $1/r$, which respectively describe the electric field component of the reactive near field, radiative near field and far field surrounding the source.

Immediately surrounding the source, the $1/r^3$ term dominates, but as the distance from the source increases, or r increases, that term becomes smaller very quickly. The far field is described by the $1/r$ term. At $r = \lambda/2\pi$, a crossing point occurs, and the far field term becomes most dominant. Therefore, this is usually approximated as the far field transition point.

This approximation becomes difficult for physically large antennas, where it is unclear where to start measuring the distance from. Therefore, these regions are described more accurately by *Equations* (2.10), (2.11) and (2.12) [15]. *Equation* (2.10) is the transition point between the reactive and radiative near field, *Equation* (2.11) describes the radiative near field region between the reactive near field and the far field, and *Equation* (2.12) is the transition point at which the far field is dominant. They hold for all antennas including large antennas.

$$R < \sqrt{\frac{L^3}{\lambda}} \tag{2.10}$$

$$\sqrt{\frac{L^3}{\lambda}} \leq R < \frac{2L^2}{\lambda} \tag{2.11}$$

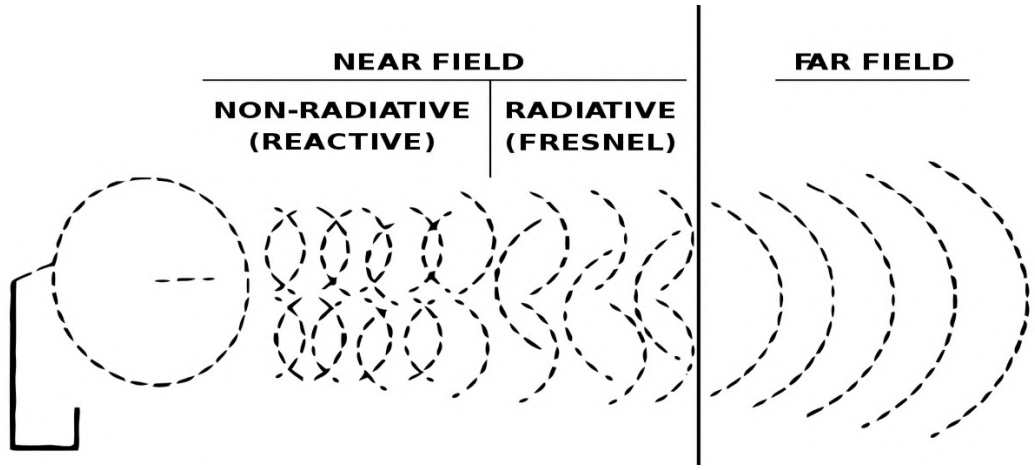

Figure 2.3: Near Field vs Far Field. Adapted from [18].

$$R \geq \frac{2L^2}{\lambda} \tag{2.12}$$

Where:

R = radial distance from the source [m]

L = largest physical dimension of antenna [m]

λ = the wavelength of the signal frequency [m]

In the reactive near field, henceforth referred to as the near field, reactive power densities dominate. In the far field, the field behaviour is predictable and approaches plane waves, whereas the near field is operationally complex and reactive, with the field pattern being far more complicated and irregular [16]. *Figure 2.3* shows a basic comparison of the wave interactions of the three regions.

In the near field, there are far more wave interactions, resulting in a non-uniform field pattern [16]. The diffraction in this region is referred to as Fresnel diffraction [17]. If the pattern is observed from the point of view of magnitude, as with standard radiation patterns, the near field pattern has small areas of increased magnitude and areas of decreased magnitude, resulting from the wave interactions, as shown on the left in *Figure 2.4*. Near field interactions make it possible to concentrate a field on a small point in space, such as over a tumour. In the far field, all common antenna relationships and design criteria start becoming applicable. Diffraction in this zone is called Fraunhofer diffraction [17].

Equation (2.12) shows that the larger the antenna becomes, the further away the near field zone is apparent. If far field radiation is to be aimed at a tumour sized object, a very narrow beamwidth is needed, resulting in a very large physical antenna, hence a far field criterion that is far away from the source, meaning an increased distance between

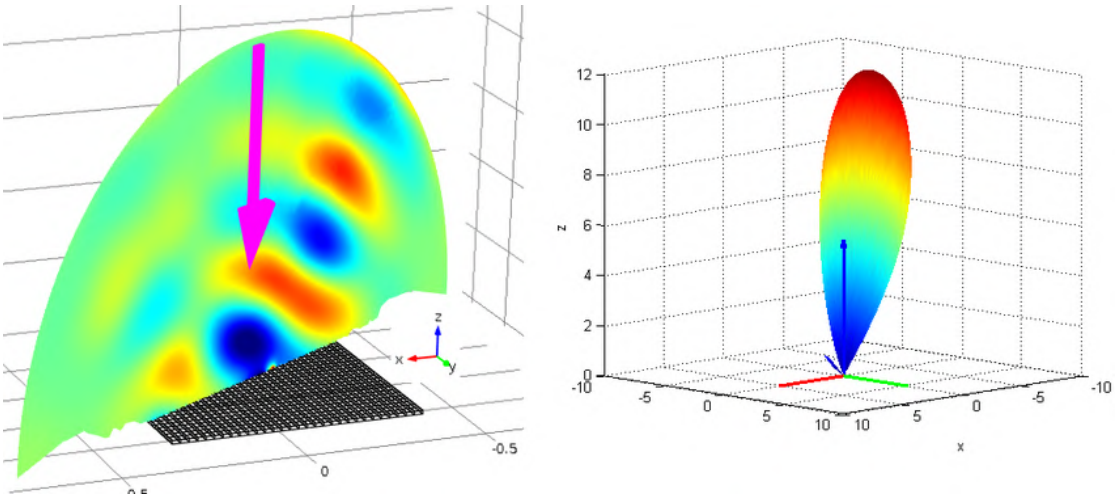

Figure 2.4: Near (left) and Far (right) field radiation patterns. Adapted from [19].

the tumour and the source. It becomes infeasible to satisfy all the required relationships while maintaining reasonable antenna size.

2.2.6 Array Theory

Array theory arises from the contribution of multiple field sources to a radiation pattern. Vector addition is performed of the field magnitude and phase at all directional points, or solid angles, surrounding the array to calculate the new radiation pattern [14]. This method is very useful in that it can increase the gain of the array by adding contributions of smaller elements instead of increasing the size of a single element. The pattern can also be manipulated by altering the phase of the feed to each element without having to alter the physical structure of the array and the array can be configured to create a broadside or end-fire pattern [20]. *Figure* 2.5 shows the utility of array theory in creating a broadside (left) and broadside/end-fire (right) array, both with enhanced gain using multiple instances of a simple point source. It also allows for the forward gain, or maximum gain, to be directed and steered without the need of changing the array's, or the antennas', physical attributes.

Array theory is useful in that it supplies a method to predict a field pattern based on the feed phase of multiple sources. It is still not feasible for tumour ablation purposes, however, as the relationships in *Equations* (2.6) and (2.7) still hold, regardless of whether the source is an array or a single antenna. The space requirements that allow for a gain large enough to narrow the beam sufficiently are still enormous, as Array Theory is applicable only in the far field.

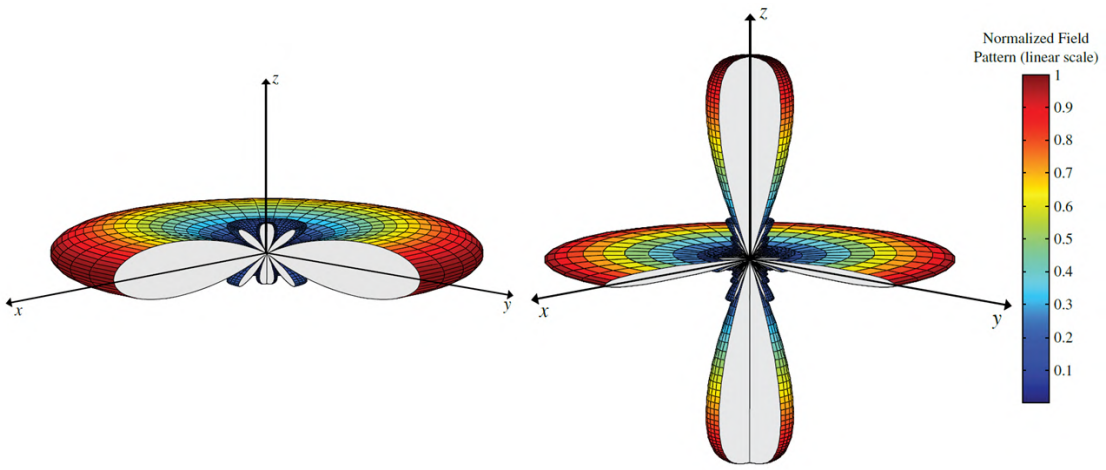

Figure 2.5: Radiation Pattern of Broadside and Endfire arrays. Adapted from [20].

2.2.7 Resonance and Resonant Cavities

Mechanical resonance refers to the greater amplitude response of a mechanical system when it oscillates with a frequency approaching its natural vibration frequency. It and 'tuned circuit' resonance demonstrates that given enough energy, even at a frequency other than the natural frequency, the system persists in resonating at that other frequency; and that the resonance bandwidth is quite narrow. In terms of antennas and antenna theory, if an antenna is fed with an appropriate frequency that falls within its bandwidth, it is said to be resonating, as in, radiating the power it is fed.

Resonance in electromagnetic terms, however, describes the sharp increase in amplitude, or magnitude, resulting from the application of an electromagnetic force or field of a specific frequency that approaches a natural frequency, or eigenfrequency, of the system upon which it acts [21]. It can also be referred to as the increased absorption that occurs when the correct combination of electromagnetic field and frequency is applied to the structure [22]. Resonant cavities are bounded resonant structures whose dimensions are comparable with, or larger than, the operating wavelength of the excitation signal. Ideally, such cavities are operated at one of their resonant modes, to achieve a resonant peak in terms of power delivery [23]. Because the cavity is, by definition, enclosed in metal, it is non-radiative and highly reactive inside the cavity, meaning the electromagnetic field patterns, or eigenfields, inside the cavity are a purely near field problem.

2.3 Microwaves

Microwaves are electromagnetic waves at microwave frequencies, as described in *Figure 2.2*. The microwave spectra of frequencies have many applications, including the microwave heating effect, the basis of microwave ovens, communication technologies, such as Bluetooth and Wi-Fi and other ISM devices.

2.3.1 Microwave Heating

Microwave heating is an effect whereby a medium absorbs electromagnetic energy to achieve rapid heating. The heating results from the conversion of electromagnetic energy at microwave frequencies to thermal energy through the agitation, or continued realignment to the field, of polar molecules such as water [24]. The magnetic permeability of most biological tissue is very similar to that of free space [25], denoted μ_0, $4\pi \times 10^{-7}$ H·m^{-1}. Therefore, biological tissue does not interact substantially with the magnetic component of electromagnetic fields and hence, heating of the tissue under the influence of a microwave field is predominantly a result of the fluctuation of the electric field.

The heating power term from *Equation (2.1)* that describes microwave heating is shown below in *Equation (2.13)*.

$$Q_{\mathrm{h}} = \mathbf{J} \cdot \mathbf{E} = \frac{J^2}{2\sigma} = \frac{\sigma E^2}{2} \tag{2.13}$$

Where:

Q_{h} = heat flux of the source of ablation [W·m^{-1}]

E = electric field strength [V·m^{-1}]

J = current density [A·m^{-1}]

And σ is the effective electric conductivity, in [S·m^{-1}], given by

$$\sigma = 2\pi f \epsilon_0 \epsilon'' \tag{2.14}$$

Where:

ϵ'' = dielectric loss factor

ϵ_0 = permittivity of free space [$\approx 8.85 \times 10^{-12}$ F·m^{-1}]

Hence, microwave power as a function of displacement and temperature is related to the electric field and can be described by *Equation (2.15)* [26].

$$P(x,T) = \frac{1}{2}\omega \epsilon_0 \epsilon'' \mathbf{E}^2 \tag{2.15}$$

2.3.2 Dielectric Influence

Different materials exhibit different affinities for converting electromagnetic field energy into heat, dependant on the material's dielectric response, a function of its dielectric characteristics [11], [27]. Each material's capacity to absorb electromagnetic energy is proportional to how well the microwaves can penetrate the material.

For reflective materials, such as metals, the penetration is zero, hence there is no absorption, whereas, for transparent materials, penetration tends to infinity [27]. When the energy is absorbed, the energy conversion into thermal energy is dependent on the dissipation factor (or loss tangent) of the material, as shown in *Equation (2.16)* [11].

$$\tan\delta = \frac{\epsilon''}{\epsilon'} \tag{2.16}$$

Where ϵ' is the dielectric constant. The relative complex permittivity, ϵ^* is given by *Equation (2.17)*.

$$\epsilon^* = \epsilon' - j\epsilon'' \tag{2.17}$$

Higher values for $\tan\delta$ translate to a higher heating capacity when microwaves are absorbed [28]. *Table 2.2*, data acquired from [11], shows the dielectric dissipation factor of some materials and solvents.

All the listed solvents have a higher affinity for microwave absorption than do the materials, hence materials are sometimes mixed with solvents to be heated more efficiently by microwave heating [11]. For all the listed substances, the dissipation factor was calculated at a frequency of 3 GHz and at 25° C, except for acetic acid and toluene, which were calculated at 2.45 GHz and 20° C.

Table 2.2: Dissipation factors of various solvents and materials at 3 GHz and 25° C.

Solvent	$\tan\delta$	**Material**	$\tan\delta$
Ethylene glycol	1	Nylon 6,6	$12.8 \cdot 10^{-3}$
Ethanol	0.25	Poly(vinyl chloride)	$5.5 \cdot 10^{-3}$
Methanol	0.64	Porcelain 4462	$1.0 \cdot 10^{-3}$
Acetic acid	0.174	Borosilicate glass	$1.06 \cdot 10^{-3}$
Water	0.157	Ceramic F66	$0.55 \cdot 10^{-3}$
0.1 mol/l NaCl	0.24	Polyethylene	$0.31 \cdot 10^{-3}$
0.5 mol/l NaCl	0.63	PTFE-PFA	$0.15 \cdot 10^{-3}$
Toluene	0.040	Fused quartz	$0.06 \cdot 10^{-3}$

In cases where the dielectric microwave absorption properties are not linear and are dependent on the temperature of the dielectric, thermal runaway can easily occur. The dielectric heats up, its affinity to absorb microwaves increases, further heating it up in a positive feedback loop.

2.3.3 Microwave Ovens

Microwave ovens are common household devices that utilise the microwave heating effect to heat food. A drawback of these ovens is that heating is non-uniform, as a result of the resonance within the cavity that causes areas of high electromagnetic field intensity and low electromagnetic intensity, or hotspots and cold spots [29], as is characteristic of near field patterns. To account for this non-uniformity, historical microwave ovens had a 'stirrer', a piece of metal that rotated, thus actively changing the near field pattern and the position of the hotspots. These days, microwave ovens often have a glass turntable at their base upon which the food is placed. The objective is to rotate the food through a non-uniform field so that different sections of the food are sporadically acted upon by a hotspot or collection of hotspots at a point in space, distributing the heating amongst the food, instead of only a small section of food continuously heating up while the rest remains cold.

The resonant near field pattern of the field inside the oven is dictated by the cavity geometry, dielectric properties of the material inside the chamber and the size and geometry of the dielectric material [24]. A microwave oven essentially describes the ability to heat a certain part of a dielectric and not others, as often happens when food is heated up. It provides an unrefined, nonspecific and imprecise mechanism for microwave thermal ablation of tissue. With microwave ovens, efforts are often made to provide wide, uniform heating of the entire dielectric, such as the addition of the turntable, instead of precise, localised heating which is needed for clinical thermal ablation in humans.

2.4 Electromagnetic Solvers

This section discusses the solution to electromagnetic problems, the various solver methods used to solve the applicable models and the simulation packages used in this investigation.

2.4.1 Maxwell's Equations

Maxwell's equations are four coupled partial differential equations, developed by James Clerk Maxwell, which form, along with the Lorentz Force Law, the basis of computational

electromagnetism. The equations provide a mathematical model for electromagnetic systems, describing how the electric and magnetic components of electromagnetic fields are generated by changing charges and currents [30]. In computational electromagnetic problems, the electric and magnetic fields must satisfy the time dependant Maxwell equations, given below:

$$\nabla \times \mathbf{E} = -\frac{\partial \mathbf{B}}{\partial t} \tag{2.18}$$

$$\nabla \times \mathbf{H} = \mathbf{J} + \frac{\partial \mathbf{D}}{\partial t} \tag{2.19}$$

$$\nabla \cdot \mathbf{D} = \rho_v \tag{2.20}$$

$$\nabla \cdot \mathbf{B} = 0 \tag{2.21}$$

Where:

$\mathbf{E}$ = electric field intensity vector [V·m^{-1}]
$\mathbf{B}$ = magnetic flux density vector [Wb·m^{-2} or T]
$\mathbf{H}$ = magnetic field intensity vector [A·m^{-1}]
$\mathbf{D}$ = electric flux density vector [C·m^{-2}]
$\mathbf{J}$ = electric current density vector [A·m^{-2}]
ρ_v = electric charge density [C·m^{-2}]

These equations are interdependent. $\mathbf{B}$ and $\mathbf{D}$ are essential for calculating $\mathbf{E}$ and $\mathbf{H}$. These equations are usually represented in differential form; however, their integral form can also be useful in certain circumstances. Both forms of the equations are shown in *Table* 2.3 [30].

Table 2.3: Maxwell's Equations in Differential and Integral Form

Differential form	**Integral form**	**Name**
$\nabla \times \mathbf{E} = -\frac{\partial \mathbf{B}}{\partial t}$	$\oint_c \mathbf{E} \cdot d\tilde{\mathbf{l}} = -\iint_s \frac{\partial \mathbf{B}}{\partial t} \cdot d\tilde{\mathbf{s}}$	Faraday's law
$\nabla \times \mathbf{H} = \mathbf{J} + \frac{\partial \mathbf{D}}{\partial t}$	$\oint_c \mathbf{H} \cdot d\tilde{\mathbf{l}} = I + \iint_s \frac{\partial \mathbf{D}}{\partial t} \cdot d\tilde{\mathbf{s}}$	Ampere's law
$\nabla \cdot \mathbf{D} = \rho_v$	$\oiint_s \mathbf{D} \cdot d\tilde{\mathbf{s}} = Q$	Gauss's law for electric charge
$\nabla \cdot \mathbf{B} = 0$	$\oiint_s \mathbf{B} \cdot d\tilde{\mathbf{s}} = 0$	Gauss's law for magnetic charge

Essentially, electromagnetic solvers or simulation packages calculate the electric and magnetic components of the electromagnetic field by solving Maxwell's equations, which generally cannot be solved analytically owing to the inherent interdependency.

2.4.2 Method of Moments

Maxwell's equations, discussed in *Section 2.4.1*, are very difficult to solve analytically. When dealing with complex antennas, three-dimensional space, large structures, or most practical purposes, they cannot be solved analytically, but they can be solved numerically. The Method of Moments (MoM) technique converts the integral equations into a linear system which can be solved numerically using a computer [31].

Essentially, the MoM solves the problem by converting integral equations into matrix equations. A noteworthy feature of the MoM is that it is a purely surface-based method, meaning that only the surface of the physical structure of the object being analysed is considered [32]. This makes the MoM very effective at dealing with perfectly conductive wire segment structures without the presence of penetrable absorbing bodies.

Additionally, the MoM is a purely frequency domain based solver method, making it efficient at solving single frequency or narrow band problems. However, for wideband problems, a fully new solution must be generated for each instance of frequency, which significantly increases solver time [32].

The procedure comprises four steps. Firstly, the structure to be modelled must be discretised into a collection of small wire segments that make up geometric primitives. The Numerical Electromagnetic Code (NEC) generally uses a grid pattern for wire segments, however, programs such as FEKO and CST Studio use triangles, because they can conform to almost any shapes' curvature and because of the very efficient triangle integration rules [33]. Secondly, expansion functions that represent the unknown current distribution along the structure and weighting functions for the segments must be chosen. Thirdly, filling the matrix using the chosen functions and solving for the unknown current distribution along the surface of the structure. Lastly, processing the calculated current distribution of the structure to find the desired characteristics of the system, including near field, far field, impedance and whatever else is required [32].

2.4.3 Fast Multipole Method

Iterative methods for solving the matrices involved in MoM computation can shorten compute time by starting with an approximation of the solution vector and attempting to minimise residuals for each iteration until the solution is sufficiently correct [31].

The Fast Multipole Method (FMM) is a method of speeding up MoM solutions instead of being its own technique. It is usually implemented as an iterative numerical algorithm that reduces the complexity of the problem. FMM uses an error-controlled approximation of the system. This allows the field interactions of a collection of particles to be evaluated as if they were a single particle [34]. The interactions between separated groups of functions can then be evaluated, allowing for the calculation of the matrix product iteratively without having to store many elements, leading to faster computing time. However, the runtime may still be high for complicated problems owing to a higher number of matrix-vector products and the fact that the solution may not converge on a correct solution easily [34].

2.4.4 Finite Element Method

The Finite Element Method (FEM) is a numerical method used to solve partial differential equations, like the Maxwell equations, by converting them into matrix equations. This process is similar to that used by the MoM, however, the partial differential form of the equations is used, instead of the integral form [35]. One of the primary features of FEM is that it can describe the essence of the problem, its geometry, dielectric bodies etc., with a degree of flexibility. This is owed to the discretisation of the domain of the problem into its so-called finite elements, which use non-uniform segments of elements, which can easily describe complex structures [36].

FEM resembles how MoM solves the problem in that they both convert a differential or integral equation into algebraic matrix equations. However, a key difference is that FEM is based on the principle of minimising the energy of the system [36] and uses sparse matrices which are solved iteratively, instead of the MoM's full matrices which are solved traditionally, using Gaussian elimination or LU decomposition. This makes FEM a slightly faster solver method and is more suited to 3D complex structures and the introduction of penetrable bodies, such as dielectrics. Essentially, FEM is a better method for solving volumetric problems, whereas MoM is ideally used for skeletal situations.

2.4.5 Finite Difference Time Domain

The Finite Difference Time Domain (FDTD) method of electromagnetic simulation provides a direct integration of Maxwell's time dependant differential equations, discussed in *Section 2.4.1*. Since FDTD uses volumetric data instead of surface data, it is very effective at modelling complex 3D structures [37]. The main difference between this method and MoM and FEM is the fact that it is a time domain technique instead of a

frequency domain technique [37]. This makes large frequency ranges very easy to handle, as, in a single time domain simulation, a response of the system to a wide range of frequencies can be decomposed using Fourier Transform (FT) techniques.

With FDTD, the space of the solution is divided into uniform mesh cells, comprising 3D voxels instead of surface triangles or tetrahedrons. For each mesh cell, the electric and magnetic field components are defined, as with FEM, however, instead of developing a matrix equation, the fields are staggered in space and moved through time, allowing for a direct field solution in time to be calculated [37]. In other words, for each iteration in time, the field components are determined and stored for that instance of time. After which, the frequency domain's spectral components can be calculated using FT.

2.4.6 Finite Integration Technique

The Finite Integration Technique (FIT) is another spatial discretisation method to numerically solve electromagnetic problems. It is very similar to FDTD in terms of how the field is solved. The main difference is that the FIT solves the integral form of time dependant differential equations, whereas FDTD solves the differential form. Hence, FIT can yield results in both the time and frequency spectral domains [38].

2.4.7 Eigenmode Expansion

Eigenmode Expansion (EME) is a computational electromagnetics method, alternatively called the Mode Matching Technique or the Bidirectional Eigenmode Propagation (BEP) method [39], used to calculate the various resonant frequencies and corresponding electromagnetic field pattern, or eigenmodes, of a structure, without the need of an excitation signal [40]. It is a linear frequency domain method of solving Maxwell's equations.

The approach is ideally suited for bounded cavities and waveguides as it can deal with cavity segments of arbitrary length without needing to reallocate memory as length increases [39]. Additionally, mismatch and impedance are of no concern as there is no excitation signal. This method is suited for finding resonant frequencies of bounded cavities fed with waveguides, however, it cannot deal with phase shifting of sources.

2.4.8 Modelling Software

This section introduces the relevant software packages used in this investigation and their utilisation of the various electromagnetic solver methods.

FEKO

FEKO [41] is a comprehensive electromagnetic solver that utilises multiple solution methods, each ideally suited to different applications, for electromagnetic field analysis. The University of the Witwatersrand provided a full license to access FEKO and all its features. FEKO supports full-wave frequency domain and time domain, as well as asymptotic solution methods [42]. Additionally, it features a characteristic mode analysis (CMA) configuration, which determines the dominance of the current modes on the structure.

- Full-wave frequency domain
  - Method of moments (MoM)
  - Finite element method (FEM)
  - Multilevel fast multipole method (MLFMM)
- Full-wave time domain
  - Finite difference time domain (FDTD)
- Asymptotic
  - Physical optics (PO)
  - Large element physical optics (LE-PO)
  - Ray launching geometric optics (RL-GO)
  - Uniform theory of diffraction (UTD)

Only, MoM, FEM, MLFMM, a type of FMM, FDTD and CMA are relevant to this investigation. There are also options to solve problems using the hybridisation of different solvers. *Figure* 2.6 shows the applications of the various solvers. FEKO comes with its own comprehensive CAD modelling application, used to create structures, discretise them and set up the simulation. There is also a comprehensive post-processor used to view the results of the simulation. This all makes FEKO ideally suited to the needs of this investigation.

FEKO can make use of a waveguide port, making the feeding of resonant cavities easier. For this investigation, the only solutions methods that were utilised were MoM and MLFMM. FEM was excluded as it can only be used in FEKO to solve dielectric media and cannot handle PEC boundaries in free space. FDTD was excluded as it cannot utilise the waveguide port method of feeding the structure.

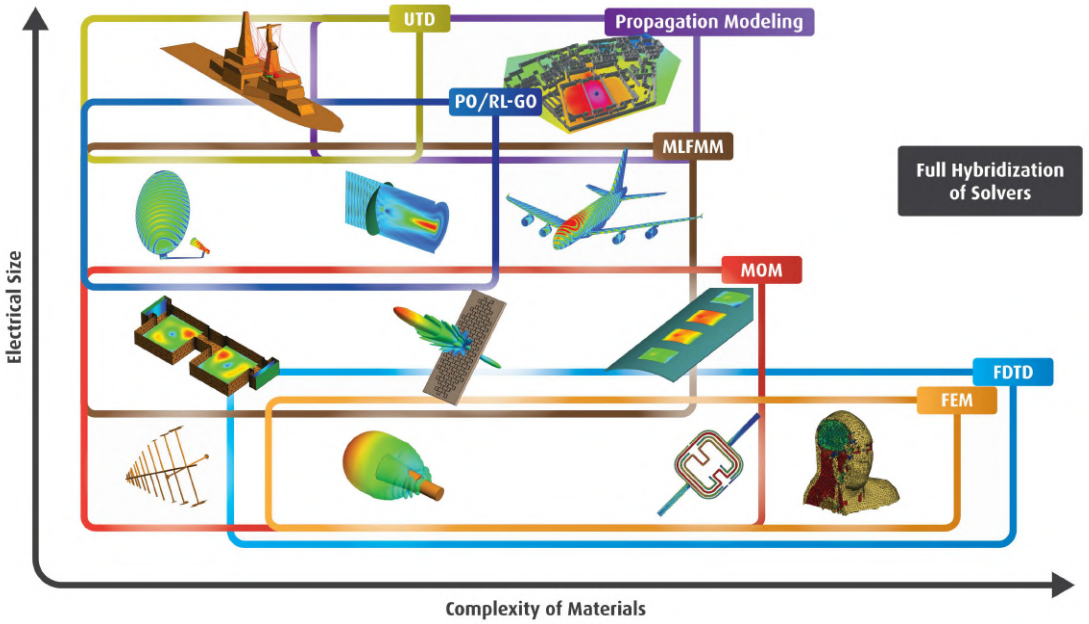

Figure 2.6: The Hybridisation of the FEKO Solvers for their Respective Applications. Image adapted from [42].

CST Studio Suite Student

CST Studio Suite [43] is a high-performance 3D electromagnetic analysis software package, developed by Dassault Systèmes, for designing, analysing and optimising electromagnetic fields, components and systems. CST offers a free student version with a variety of limitations on mesh sizes, available solvers and export and import capabilities. Additionally, a watermark is always present, and it cannot be used commercially.

Like FEKO, CST has the capability of utilising many individual or multiple electromagnetic solver methods. Unlike FEKO, where each solver method can explicitly be selected, CST utilises many different solver platforms, based on the needed application. The program has five main classes of solver, namely High Frequency, Low Frequency, Multiphysics, Particles, and EMC and EDA [40]. High Frequency, the solver platform relevant to this investigation can be broken down into a series of solver methods, as follows:

- Asymptotic
- Eigenmode
- Filter Designer 2D
- Filter Designer 3D
- Frequency Domain

- Integral Equation
- Multilayer
- Time Domain
- Hybrid Solver Task

In the student edition, only Frequency Domain, Time Domain and a selection of static and thermal solvers are available. The frequency domain solver is based on FEM, including a model order reduction (MOD) feature to speed up the simulation time of resonant structures. The time domain solver utilises the FIT solver and the transmission line matrix (TLM) solver, which is not relevant to this investigation. The combination of FEM and FIT solver methods makes CST very efficient at wideband frequency sweeps.

CST Suite Students Edition does not include an implementation of the Boundary Element Method (BEM), so there is no MoM or FMM solver included. These implementations are part of the Multilayer and Integral Equation solvers, which are only available with the full version of CST. However, the frequency and time domain solvers available are sufficient for the simulation needed in this investigation.

CST comes native with comprehensive CAD and post-processing modules, making it easy to create, mesh and simulate models, and process the results. Additionally, for microwave problems, it features the ability to use a waveguide port, which launches a plane wave of the appropriate frequency down the waveguide.

HFWorks

HFWorks [44] is the high frequency software solution from EMWorks. It can carry out S-parameter, antenna and resonance studies. A research evaluation license was provided by EMWorks for the investigation. It features three different solution studies depending on what is being simulated: S-Parameters, Resonance and Antennas. It uses the FEM solver model.

HFWorks was utilised solely for its resonance study feature, which uses an eigenmode solver to determine the resonant frequencies of the system and the corresponding electric near fields, eliminating the need to feed the structure at all, as it determines the natural resonance of the structure. This provides a useful characterisation of the resonance of the cavity.

Numerical Electromagnetic Code

The Numerical Electromagnetic Code (NEC) is based on a previous method of moments code for thin wires, the Antenna Modelling Program (AMP). It can model antennas in free space, over a perfectly conducting ground plane, or lossy material [45]. The program provides a purely MoM solution to the Maxwell equations.

SuperNEC [46], developed by The University of the Witwatersrand and Poynting Software (Pty) Ltd, provides a C++ based MoM-UTD hybrid code, based on the FORTRAN program, NEC2 [46]. While NEC2 is simply a simulation engine, requiring a text file input and outputting another text file, SuperNEC provides a rudimentary interface for generating a set of predetermined structures, or assemblies. The interface uses the native Structure Interpolation and Gridding (SIG) approach to generate NEC input files. The list of predetermined models is limited. However, new assemblies can be created manually, or through a guide inherent to SuperNEC [46].

The NEC approach is limited, as only purely MoM solutions are available, meaning high simulation times for broadband sweeps. Additionally, SuperNEC cannot utilise the waveguide port structure excitation approach adopted by FEKO and CST Studio, which launches a plane wave from a waveguide face. Instead, a single wire feed must be used. Additionally, the complexity of structures is not easily modelled, as each model is in essence a collection of manually placed interconnecting wires. However, for MoM based rectangular resonance problems, SuperNEC provides a suitable simulation platform.

Matlab

MATLAB is a widely used programming and numerical computing platform, developed by MathWorks [47]. It provides an easy method of dealing with NEC problems, like creating assemblies, creating and editing NEC input files, programming relevant post-processing applications. Additionally, output data from FEKO and CST Studio can be further refined into a meaningful relationship, providing a useful tool for this investigation.

Chapter 3

Methodology

This chapter presents the methodology used to answer the research questions in this investigation. The methodology was divided into four sections.

Section 3.1 discusses the method used to test the various electromagnetic simulation programs against each other for a standard rectangular resonant cavity.

Section 3.2 discusses the verification of the simulation software by creating a model of a microwave oven and comparing its simulated fields to the fields that were inherent in the physical oven.

Thereafter, a new resonant cavity model was created based on documented standard waveguide behaviour. This model was characterised in *Section* 3.3. The characterisation included a resonance study, which calculated the cavity's eigenfrequencies and corresponding eigenfields, an analytical calculation of its characteristic modes, and various near field simulations. The system's sensitivity to dielectric influence is also presented, as well as its frequency bandwidth.

Section 3.4 pertains to the manipulation of the field pattern inside the new rectangular cavity to move the hotspots by frequency and phase shifting. An additional section, *Section* 3.5 summarises the software used for each area of the investigation.

3.1 Software Testing

An array of software packages was used to simulate the electromagnetic near field inside a basic rectangular cavity with a rectangular waveguide input. The programs were CST Studio Suite Student Edition, FEKO, HFWorks and SuperNEC, all of which use slightly different solver methods to calculate the fields and offer slightly different pros and cons.

There were two reasons for this approach. Firstly, to lend some diversity relating to how the model is solved; FEM, FMM, MoM and FDTD were all used. Secondly, numerical instability frequently occurs when simulating resonance owing to the peaking amplitude over a very narrow bandwidth. The various programs and techniques exhibit different tolerances around resonance.

The various solver methods and programs were discussed in depth in *Section 2.4*. For this investigation, FEKO was used to conduct MoM and FMM simulation, SuperNEC was used for MoM simulation, CST Studio was used for FEM and FDTD, or FIT simulation and HFWorks was used to conduct resonance studies on the structures using its EME solver.

This section discusses the benchmark model used to initially evaluate each program and how the programs' outputs were compared. HFWorks was excluded from the comparison as it was not used for any near field simulations, only to characterise the resonance of the waveguide.

3.1.1 Benchmark Model

The benchmark model geometry was based on a standard microwave frequency feed of 2.45 GHz, giving a wavelength of ≈ 122 mm. The cavity was set to a $2\lambda \times 2\lambda \times 1\lambda$ rectangle, with no specific design procedures being employed, as the model only functioned to compare outputs between the programs. The feed was a standard waveguide, centred on the front wall of the cavity, designed to the common convention of $0.6\lambda \times 0.3\lambda$ in cross-section. The waveguide length was set to 1λ long. The metric dimensions of the model are shown in *Table 3.1*. This model functioned to establish similarity between the different simulation platforms and solver methods.

Table 3.1: Dimensions of the basic rectangular cavity.

	Cavity	**Waveguide**
Width (mm)	244.73	73.42
Length (mm)	244.73	122.37
Height (mm)	122.37	36.71

3.1.2 Results and Deliverables

The respective software packages had to essentially simulate the same benchmark to establish a comparison between their outputs. The benchmark model was a rectangular cavity described by the dimensions given in *Table 3.1*. The electric near field inside the cavity section of the model was simulated at 2.45 GHz using the following settings.

The frequency domain solver was used in CST, standard MoM was used in FEKO, and standard MoM was used in SuperNEC. These are the default solvers for each software. In SuperNEC, two models were created, one with the single wavelength waveguide and another with a waveguide two wavelengths long, to try inducing a plane wave at the waveguide opening. For CST and FEKO, this was not necessary as they can both employ a waveguide port as a feed, which launches a plane wave anyway.

The material and boundary conditions were set in each case such that a vacuum, free space, was evident inside the cavity and the metallic walls of the cavity were modelled as a perfect electric conductor (PEC). Four representations of the electric near field data were examined to establish a comparison. These were: three 2D contour slices of the data on the XY, XZ and YZ planes directly through the centre of the model, and an iso-surface 3D plot of the data. In CST and FEKO, these outputs are easily generated, however, SuperNEC has no iso-surface plotting implementation. Therefore, an application based in MATLAB was written to receive an NEC output file, extract and plot the iso-surface data from it. Appendix A describes the working of the application.

Additionally, all programs use slightly different feed methods, so near field amplitude comparison would not be applicable. While CST and FEKO both use a waveguide port, CST's port is based on scattering parameters, while FEKO's is based on the input voltage. SuperNEC uses a voltage source attached to a monopole. Therefore, the patterns were compared relative to each of their respective maximum and minimum values. Additionally, where possible, input power from each port was compared to demonstrate the different feed methods. In each case, the frequency sweep at which resonance was examined was 2.2 - 2.7 GHz, given a 500 MHz bandwidth centred around 2.45 GHz. Appendix B shows a comparison of all applicable solvers available to all the programs.

3.2 Verification

This section describes the method used to verify the simulated results. The method constituted creating a model of a physical microwave oven and comparing the electric near field pattern of the simulated model with that of the actual oven. The method used to obtain planar field data from within the microwave oven is discussed. In simulation, FEKO was used to simulate the internal electric near field of the model and attempts were made to match the simulated data with the measured data.

3.2.1 Microwave Oven Model

A microwave oven, the Defy DMO 383 Microwave Oven, was obtained and was used to verify the simulation software where possible. The oven has internal rectangular dimensions of $301 \times 311 \times 202$ mm according to the manual. The geometry, however, is not rectangular, containing many lofts, bevels and indents. The complex geometry was measured, where possible, and a CAD model was generated using Autodesk Inventor [48], which makes educational licenses available for students. Instead of a standard waveguide feed, the oven's magnetron uses a monopole antenna to pump energy into a small chamber of $85 \times 70 \times 30$ mm which opens into the main cavity through a rectangular hole of 69×56 mm. This model was then imported directly into FEKO.

CST Student Edition was not used as geometry import is not supported for the student edition. Additionally, a limitation of the student edition is a maximum mesh size of 20 000 tetrahedrons for the frequency domain solver and 100 000 voxels for the time domain solver, both of which were exceeded by the complex geometry. SuperNEC was not used owing to the difficulty in creating an input NEC file that described complicated geometry accurately. A dry run of the model was simulated at 2.45 GHz using MoM in FEKO to find the hotspots of the system.

3.2.2 Actual Field

The actual field inside the microwave was found using thermal paper, the same that is often found in till slips. The paper changes colour from white to black in the presence of heat. Since microwaves interact with polar molecules, like water, the paper was dampened so the heating of the water on the paper would induce heat in the paper itself. Strips of paper were layered on sheets of polystyrene, using masking tape as an adhesive, to create a 'plane' upon which the electric field could act. Polystyrene was selected for its lightness, rigidity, inability to absorb water and warp under its influence, and low dielectric permittivity, meaning it will not largely interact with and alter the electric field.

These sheets were wet and placed inside the microwave oven individually, after which the oven was turned on for 30 seconds. The experiment was conducted 12 times. The paper would darken in areas of high electric field intensity and remain white in low areas, thus creating a visual pattern to compare with. Since the magnetron inside the microwave tends to shift in frequency during use, many different field patterns were created. Therefore, areas of consistent overlap were looked for to be used as the dominant hotspots of the system.

3.2.3 Operating Frequency

As mentioned previously, the frequency of the energy delivered by a magnetron in a microwave oven can vary over time. As discussed in [49], this change in operational frequency is influenced by many factors, including the effects of 'pulling' and 'pushing' on the magnetron owing to changes in the power reflected to the magnetron and the cathode current in the magnetron. The presence of an absorbing body could influence the reflected power as it absorbs microwave energy and its subsequent affinity to absorb more energy could change. Therefore, the operational frequency or frequencies of the microwave had to be determined. This was accomplished through measurement.

A spectrum analyser, the Anritsu MS2036A VNA Master, supplied by Wits University, which can operate as both a spectrum analyser and a Vector Network Analyser (VNA), was used to determine the electromagnetic leakage of the microwave oven during operation. The A-Info DS-3300 Log-Periodic Dipole Array (LPDA) at Wits was used to take measurements.

The antenna has a wide band of operation, 30–3000 MHz, which suited the desired measurement frequency range of 2.2–2.7 GHz. The LPDA was initially calibrated using the VNA and the VSWR was tested in the range of 2.2–2.7 GHz to ensure the antenna was matched (VSWR$\leq$ 2) at those frequencies. Then it was placed inside the shielded anechoic chamber at Wits University and pointed at the microwave oven. A series of tests were then conducted. A glass of water was placed inside the oven to measure the frequency of the leakage with the presence of an absorbing body, and a sheet of polystyrene was placed at the base of the oven to test the 'empty' conditions which were present to measure the hotspots of the oven.

3.2.4 Simulated Field

Because polystyrene, a dielectric medium, was used to hold the thermal paper, it would be expected to interact a little with the electromagnetic field inside the cavity. Hence, a similar sheet of dielectric was added to the empty microwave model for simulation. FEKO's media library contained both polystyrene and Styrofoam, which is a trademarked term for a type of polystyrene. Three simulation instances were simulated: an empty cavity, a cavity with a sheet of polystyrene inside, and a cavity with a sheet of Styrofoam inside.

Since the microwave's magnetron tends to frequency shift during operation and the nature of simulation only allows the observation of a field of a single discreet frequency at a time, a sweep of frequencies had to be simulated. Hence, the model was simulated

using a range of 500 MHz, 2.2 GHz to 2.7 GHz, allowing for a shift of 250 MHz on either side of the central 2.45 GHz. The frequency interval was initially set to 10 MHz, resulting in 51 different simulation iterations. Each iteration was examined for similarity to the measured data on the thermal paper. Additionally, another frequency sweep with a much narrowing interval was simulated according to the results of *Section* 3.2.3.

The simulation was carried out in FEKO, using a pure MoM solution for the cavity and FEM for the dielectric sheet. The FEM solution relied on the direct sparse solver, as the iterative solver would not converge. This is also why MoM was used over MLFMM. This solver setup successfully simulated the near field data by releasing the MoM matrix from memory before solving the FEM elements. The results of this simulation can be found in *Section* 4.2.

3.2.5 Results Comparison

Owing to the nature of the experiment, the results would be largely image-driven, requiring a visual determination of accuracy. To aid this process, MATLAB was used to analyse the images and provide the means to directly compare the measured and simulated data.

Initially, all the images were cropped to an exact square and then resized so they each had an identical number of pixels. The images were then converted to *double* format, resulting in a three-dimensional numerical array. Then, they were converted to grayscale, allowing a single numerical representation of white to black colour. A threshold value was then set. Every pixel above the threshold was set to 0, or black, and every pixel below the threshold was set to 1, white, resulting in a binary image. Following this, MATLAB's image processing toolbox was used to fill in the small holes in each image that arose from the warping of the paper and to pad each array with zeros, so they would have a thin black border. Then the logical OR and logical AND operators were applied to the images, to generate two images; one of which showed all possible hotspots from all the images and the other showed the hotspots that were evident in all the images and overlapped. The same process was applied to the FEKO generated simulation images for a variety of frequencies and a like for like comparison was possible.

3.3 Cavity Characterisation

This section discusses the formulation of a new rectangular resonant cavity model designed to 'ideal' specifications. A standard waveguide design was used as a starting point for the cavity. The cavity was characterised in terms of its resonance and a frequency sweep was simulated to determine the effects of a waveguide feed.

3.3.1 Ideal Rectangular Cavity

A simple rectangular cavity was designed based on documented waveguide behaviour. The rectangular waveguide was selected owing to its easy geometry, well-documented characteristics and the fact that simulation of rectangular structures is memory inexpensive owing to easy meshing. Standard waveguide WR340 [50] exhibits the characteristics shown in *Table* 3.2. These were ideally suited for microwave problems.

Table 3.2: Characteristics of the WR340 waveguide.

Recommended frequency band (GHz)	2.20–3.30
Cut-off frequency of lowest order mode (GHz)	1.736
Cut-off frequency of highest order mode (GHz)	3.471
Dimensions [w×h] (mm)	86.36×43.18

The following equations, taken from [51], were used to verify the waveguide cut-off frequencies for waveguide operating in mode TE_{mn}.

$$f_{c_{mn}} = \frac{c}{2\pi} k_{c_{mn}} \tag{3.1}$$

$$k_{c_{mn}} = \sqrt{\left(\frac{m\pi}{a}\right)^2 + \left(\frac{n\pi}{b}\right)^2} \tag{3.2}$$

Where:

$f_{c_{mn}}$ = cut-off frequency of mode mn [Hz]
$k_{c_{mn}}$ = wavenumber corresponding to mode mn
a = length of waveguide in **H** direction, or width [m]
b = length of waveguide in **E** direction, or height [m]
c = speed of light $\approx 2.998m \times \cdot\mathrm{s}^{-1}$

Given $a = 86.36$ mm and $b = 43.18$ mm, the cut-off frequency for mode TE_{10} was determined to be 1.7358 GHz and the cut-off frequency for the next mode, TE_{20} was 3.4715 GHz, consistent with the information in *Table* 3.2. The cavity itself was designed at triple the waveguide dimensions in all directions, with the width and length being equal. The reason behind this was to aim for a starting pattern of a 3×3 grid of hotspots, a TE_{303} mode pattern. Seeing as the waveguide excited with a TE_{10} wave at the appropriate frequency exhibits a single central hotspot, those dimensions were tripled to achieve nine local hotspots. The waveguide feed was positioned centrally on the front wall of the cavity. *Table* 3.3 shows the final dimensions of the cavity.

Table 3.3: Dimensions of the ideal rectangular cavity.

	Cavity	**Waveguide**
Width (mm)	259.08	86.36
Length (mm)	259.08	86.36
Height (mm)	129.54	43.18

3.3.2 Waveguide Resonant Frequency

Table 3.2 shows the characteristics of the standard WR340 waveguide. In HFWorks, a resonance study was conducted on a model of the waveguide to determine its eigenfrequencies. Additionally, a frequency sweep between 2.2 GHz and 3.3 GHz in CST and FEKO was conducted to observe a near field pattern that changes with frequency within the waveguide. Since the waveguide was excited with TE_{10} mode, a single electric field hotspot was expected to be evident in the waveguide in the **H** direction. The frequency of excitation determines how the waveguide resonates, or the number of hotspots evident along the length of the waveguide.

3.3.3 Cavity Resonant Frequency

Like the waveguide, a resonant cavity exhibits certain eigenfrequencies at which the structure resonates naturally. Additionally, the electric near field characteristics within the chamber are dependent on its operational frequency. The dominant resonant modes of the cavity were determined analytically using *Equation* (3.3) [52].

$$f_{mnl} = \frac{ck_{mnl}}{2\pi\sqrt{\mu_r\epsilon_r}} \tag{3.3a}$$

$$k_{mnl} = \sqrt{\left(\frac{m\pi}{a}\right)^2 + \left(\frac{n\pi}{b}\right)^2 + \left(\frac{l\pi}{d}\right)^2} \tag{3.3b}$$

Where:

f_{mnl} = cavity resonant frequency for mode TE_{mnl} [Hz]

k_{mnl} = wave number corresponding to mode TE_{mnl}

c = speed of light $\approx 2.998m \times \cdot s^{-1}$

a, b, d = dimensions of the cavity [m]

And

$$\frac{1}{\sqrt{\mu_r\epsilon_r}} = 1$$

for a cavity containing free space. This equation can be used also for structures such as waveguides, however, waveguides are often used as feed and hence, are not completely bounded.

Only one of the mode numbers, which must be positive integers, can be set at zero at a time [53]. *Equation (3.3)* was used iteratively to determine the resonant modes in the range of 2.2 to 2.7 GHz. This range was used as microwave ovens are centred around 2.45 GHz. The range gives a 250 MHz width on either side of this centre frequency. Additionally, this range is encompassed in the recommended range of the WR340 waveguide, being 2.2 to 3.3 GHz. These modes are descriptive of an empty resonant cavity, as the presence of a dielectric body within the cavity detunes the resonance and coupling within the cavity [54]. A frequency sweep, requesting the internal near fields of the cavity with the excited waveguide as power input, was conducted in CST and FEKO.

3.3.4 Dielectric Influence

Since the presence of dielectric media influences the resonance of a system [54], the cavity would have to be re-examined after the addition of a body of dielectric. Since microwaves operate best on polar molecules like water, a cylinder of water was placed centrally inside the cavity. Thereafter, another frequency sweep between 2.2 and 2.7 GHz, again with an excited waveguide as a feed, was conducted. Because the water can absorb the electromagnetic energy and convert it to heat, the energy generated by the source can be absorbed instead of reflected, so a reasonable VSWR was expected from this simulation, making it possible to obtain the operating bandwidth of the system in terms of VSWR.

3.4 Field Manipulation

This section described the methodology used to manipulate the fields within the resonant cavity models to move the internal hotspots. The method revolved around investigating the effects of slight changes in frequency on the hotspots, and the effect of the feed phase on the hotspots. To investigate the feed phase, a second excited waveguide was added and a phase difference between the sources was introduced. The second waveguide was added in three different orientations, as shown in *Figure 3.1*.

The change in hotspot position was examined, instead of the complete change of field pattern, as the investigation requires the controlled movement of a defined hotspot. In each case, the cavity was examined empty, without any dielectric body present. If hotspot movement could be achieved in free space, it serves as a proof of concept which could be extended to encompassing entities of different dielectric characteristics.

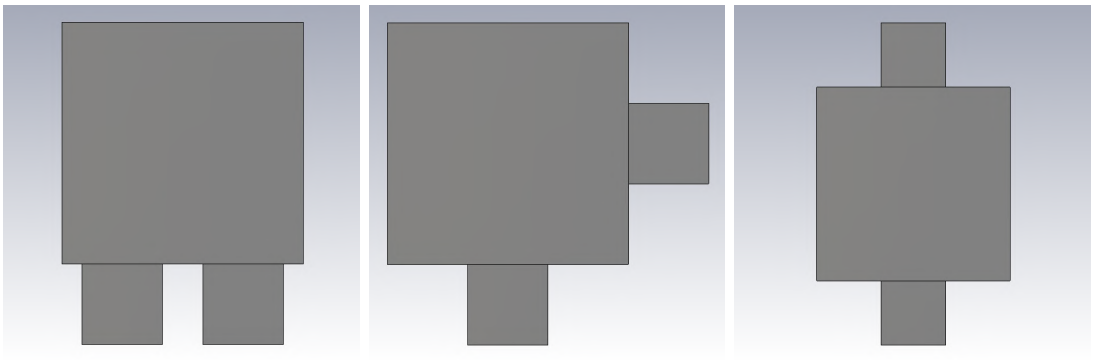

(a) Same face. (b) Adjacent faces. (c) Opposite faces.

Figure 3.1: Waveguide Orientations. Images adapted from CST Studio.

3.4.1 Frequency Shifting

As discussed in *Section* 3.3.2, the frequency applied to a waveguide determines how it, and subsequently the resonant cavity it feeds, resonate. The frequency of the eigenfield determines the nature of the field pattern and the position of the hotspots. For the model with a single excited waveguide feed, a new frequency sweep between 2.2 GHz and 2.7 GHz was conducted with intervals of 1 MHz using the MLFMM solver in FEKO and using the FIT and FEM solvers in CST.

The hotspot positions were observed for a range of frequency steps surrounding each of the cavities' dominant eigenfrequencies as well as directly between the resonant modes. Additionally, the maximum field strength and input power were observed at each frequency to determine the location of any resonant peaks. Where necessary, new simulations were conducted with a finer step interval to increase precision.

3.4.2 Phase Shifting

In cases where multiple waveguide feeds were evident, the phase of each waveguide feed could be controlled to provide a phase difference between the sources. The waveguides could be fed in phase, exactly out of phase, or with any phase difference in between. The geometric positions of the waveguides relative to each other could also introduce physical phase differences. Again, a frequency shift between 2.2 and 2.7 GHz, with a step of 1 MHz was conducted for each of the three models. Additionally, an incremental phase difference was introduced between the waveguides with a step of 15°, starting at 0° and ending at 345°, resulting in 24 iterations, each describing a different phase shift.

The introduction of multiple phase shifts excluded the possibility of using the FDTD or FIT solver, as only one phased feed could be simulated at a time. Therefore, only the FEM solver in CST was used along with the MLFMM solver in FEKO. Again, each phase

iteration at each eigenfrequency was examined, along with discreet frequency points in between each resonant mode. For this method, the feed frequency was held constant while only the feed phases were changed, to investigate any hotspot movement as a result of phase shifting of the feeds.

3.4.3 Bandwidth

The frequency bandwidth at which the resonant cavity resonates was investigated. A wide bandwidth infers that small changes in frequency around the resonant frequency will not affect the near field pattern inside the cavity and the structure will still resonate. A narrow bandwidth implies that if the frequency changes slightly, the near field pattern is likely to change, or the cavity may not resonate at all. Additionally, the characteristic modes of the empty cavity were compared to that of a cavity containing dielectric. This investigation facilitates an understanding of the effect of dielectric bodies. The presence of dielectric matter may shift the resonant frequency of the chamber. If the cavity can be fed by a single frequency, and the resonant frequency of the cavity is shifted outside the bandwidth, the cavity may not resonate when the dielectric is present. This presents major implications to the feasibility of this investigation applying to thermal ablation of tumours, where dielectric influence is variable and extremely important.

3.5 Software Summary

This section describes the software packages and their respective solvers used in each section of the investigation. The information is summarised for each section.

3.5.1 Benchmark

This section entailed the comparison of the simulation results of each program for a standard benchmark model. The default solver settings were used for each program. SuperNEC and FEKO were both utilised with their MoM solver and CST's frequency domain solver, which uses FEM, was utilised, as summarised in *Table 3.4*. HFWorks was not used.

3.5.2 Verification

This section entailed verifying the simulation results by comparing the near field simulations to a real-world microwave oven's measured near field data. Only FEKO was used for this method. It was used in hybrid mode, combining its MoM and FEM solvers, as shown in *Table 3.5*.

Table 3.4: Summary of the Software Used for the Benchmark Section.

	Solver				
Software	MoM	FMM	FEM	FDTD/FIT	EME
SuperNEC	•				
FEKO	•				
CST Studio			•		
HFWorks					

Table 3.5: Summary of the Software Used for the Verification Section.

	Solver				
Software	MoM	FMM	FEM	FDTD/FIT	EME
SuperNEC					
FEKO	•		•		
CST Studio					
HFWorks					

3.5.3 Characterisation

This section entailed creating a new 'ideal' model of a resonant cavity and characterising it. This focused mainly on resonance. For this, FEKO, CST Studio and HFWorks were used. FEKO's MoM and MLFMM solvers were used to simulate the near fields inside the waveguide and cavity. CST used its frequency domain (FEM) and time domain (FIT) solvers on the cavity and HFWork performed a resonance study on the waveguide. This information is summarised in *Table* 3.6.

Table 3.6: Summary of the Software Used for the Characterisation Section.

	Solver				
Software	MoM	FMM	FEM	FDTD/FIT	EME
SuperNEC					
FEKO	•	•			
CST Studio			•	•	
HFWorks					•

3.5.4 Frequency Sweeping

This section entailed conducting a broadband frequency sweep of the cavity with narrow frequency steps. Therefore, FEKO's FMM solver, MLFMM was used as it is faster than the MoM solver, demonstrated in *Appendix* B. CST's frequency domain (FEM) and time domain (FIT) solvers were used, as their simulation times are both low. *Table* 3.7

shows this data. SuperNEC and HFWorks were not used in this section.

Table 3.7: Summary of the Software Used for the Frequency Sweeping Section.

	Solver				
Software	MoM	FMM	FEM	FDTD/FIT	EME
SuperNEC					
FEKO		•			
CST Studio			•	•	
HFWorks					

3.5.5 Phase Shifting

This section involved introducing feed phase differences between multiple waveguide sources. This eliminated all time domain solvers. FEKO's MLFMM solver was used instead of MoM, owing to the simulation speed, and the frequency domain solver was used in CST Studio.

Table 3.8: Summary of the Software Used for the Phase Shifting Section.

	Solver				
Software	MoM	FMM	FEM	FDTD/FIT	EME
SuperNEC					
FEKO		•			
CST Studio			•		
HFWorks					

3.5.6 Comparison

This section compared the results obtained by CST Studio and FEKO. Therefore, all applicable solvers available to the two programs were used. HFWorks and SuperNEC were not used as they were not the predominant programs used for the investigation.

Table 3.9: Summary of the Software Used for the Software Comparison.

	Solver				
Software	MoM	FMM	FEM	FDTD/FIT	EME
SuperNEC					
FEKO	•	•			
CST Studio			•	•	
HFWorks					

Chapter 4

Results

The findings of the methodology, outlined in Chapter 3, are presented in this chapter, along with conclusions linking them to the research questions.

4.1 Software Testing

This section presents the comparison of the output from simulation in the three software packages: CST Studio Students Edition, FEKO and SuperNEC.

4.1.1 Comparison

A standard benchmark model was created in all three software packages, as discussed in *Section 3.1*. *Figure 4.1* shows a comparison between the results obtained by the three software packages in the horizontal contour plane through the centre of the model.

While clearly CST Studio, *Figure 4.1a*, and FEKO, *Figure 4.1b*, yield largely identical results, the similar SuperNEC model exhibits slightly different results, as shown in *Figure 4.1c*.

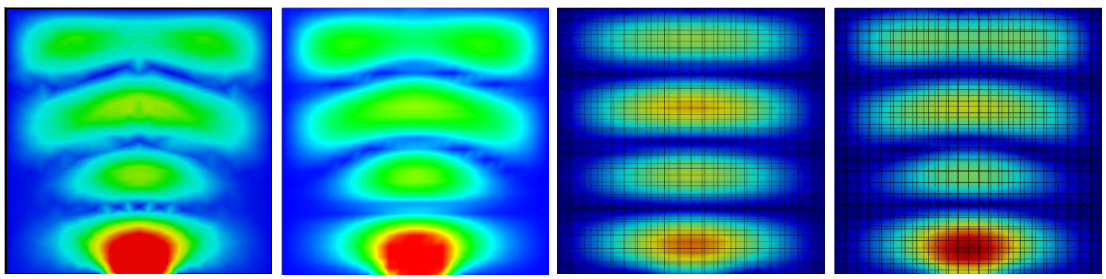

(a) CST Studio (b) FEKO (c) SuperNEC (a) (d) SuperNEC (b)

Figure 4.1: Comparison of the Centre Horizontal Plane of the Benchmark Model.

This could be because SuperNEC must utilise a monopole feed to excite the waveguide instead of a waveguide port. The difference is that a waveguide port launches a plane wave whereas a monopole antenna does not. To rectify this, another model in SuperNEC was created with a waveguide elongated by an extra wavelength to allow the wave launched by the monopole to become more plane. This simulation is shown in *Figure 4.1d*, which is more like the CST and FEKO simulations, indicating the elongated waveguide at least partly solves the problem. Note that the plane wave waveguide port source used in the simulation is not practically realisable, it is simply a simulation device used for ease. To realise a plane wave, the SuperNEC method of elongating a waveguide can be used.

Important to note is the threshold used in each model. For both CST Studio and FEKO, a colourmap maximum of 200 V/m was used, whereas in SuperNEC (a), a maximum of 75 V/m was used and in SuperNEC (b), a maximum of 15 V/m was used, indicating a scaling difference, possibly owing to the different feed mechanisms. To verify this, the input power and the average field strength in each simulation was checked. *Table 4.1* compares these values. CST was not considered as it was deemed very similar to the FEKO simulation based on the field pattern.

Table 4.1: Radiated Power and Mean $\tilde{E}$ Field Comparison.

	Mean Field (V/m)	**Input Power (W)**
FEKO	57.823	0.202
SuperNEC (a)	20.909	2.929×10^{-3}
SuperNEC (b)	11.600	8.511×10^{-4}

FEKO and SuperNEC both produced an output file from which necessary data was easily extracted. The table clearly shows the impact of the feed mechanism, as there are different mean values and radiated power values for each simulation. It was also able to consider the power and field ratios of each simulation. The FEKO to SuperNEC radiated power ratio could be calculated by simply dividing FEKO's radiated power by NEC's. Since voltage has a square relationship with power, to compute the electric field ratios, FEKO's average electric field was divided by NEC's and squared.

This yielded a FEKO to NEC radiated power ratio of $\approx 69:1$ and an average electric field ratio of $\approx 7.6:1$ for SuperNEC (a), indicating the power-to-voltage ratio of $\approx 9.1:1$. For SuperNEC (b), the FEKO to NEC power ratio was $\approx 238:1$ and the average electric field ratio was $\approx 24.8:1$, indicating a power-to-voltage ratio of $\approx 9.6:1$. In both cases the value was between 9 and 10, demonstrating the clear scaling factor implicit in the feed mechanism.

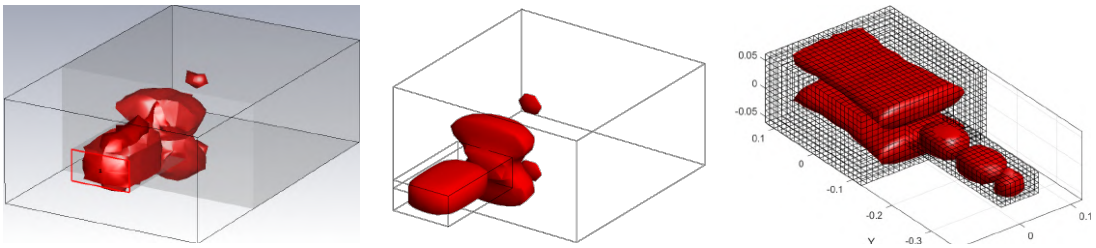

(a) CST Studio (b) FEKO (c) SuperNEC

Figure 4.2: Comparison of the 3D Iso-Surface of the Benchmark Model.

Figure 4.2 shows the 'hotspots' of the field using the inherent iso-surface plotter in CST and FEKO and the written MATLAB program for the NEC result. Again, it is apparent that CST Studio and FEKO yield the same result, whereas SuperNEC simulates a different one, despite the elongated waveguide. It appears the resonance in the SuperNEC model is slightly shifted, yielding a slightly different field pattern, again possibly owing to the feed method. Additionally, the iso-surface threshold value for both CST and FEKO was set to 180 V/m, whereas in SuperNEC was set to 18 V/m, highlighting again the scaling differences.

Hence, it was concluded to proceed with only CST Studio and FEKO as simulation platforms for the remainder of the investigation owing in part to the comparative simplicity of editing the model's geometry, and to the apparent 'tweaking' required in SuperNEC to match the simulation results.

4.2 Verification

The results of the methodology used to verify the simulation are presented. The actual electromagnetic fields inside the microwave oven were compared with the simulated fields inside the model in FEKO.

4.2.1 Microwave Oven

The model of the microwave oven, created in Autodesk Inventor and imported to FEKO, then meshed and solved, is shown in *Figure* 4.3, which also shows the 3D iso-surface hotspots at 2.45 GHz within the cavity. The iso-surface threshold value was set to 25% of the maximum, resulting in 150 V/m. The geometry shown is an approximate depiction of the inner cavity. The outer casing was not included as the inner cavity is completely bounded.

To measure the model, the outer casing was removed from the microwave and the internal cavity dimensions were measured as accurately as possible, after which the CAD model

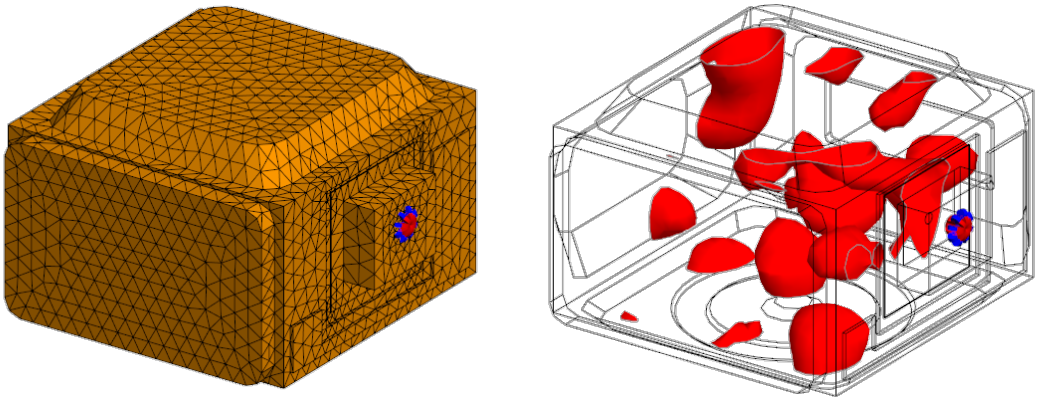

(a) Microwave Geometry and Mesh in FEKO. (b) Simulated Hotspots in the Microwave.

Figure 4.3: The Microwave Geometry and Simulated Hotspots at 2.45 GHz in FEKO. Images exported by FEKO.

was created. Certain features, such as the curved edges, had to be removed from the CAD model to allow for a reasonable mesh density, so the solver matrix did not exceed available memory.

4.2.2 Microwave Oven Fields

As described in *Section* 3.2, the near field pattern inside the microwave oven was determined by using thermal paper attached to a slab of polystyrene and dampened with water. Multiple tests were conducted and *Figure* 4.4 shows the results of the three clearest iterations. The figure is orientated with the bottom of the images corresponding to the front of the microwave oven, by the door, and the right of the images corresponding to the waveguide port. Each slab was heated for 30 seconds in the microwave. Slight variation in the results occurred owing to the slight variation in the operating frequency of the magnetron as well as at the random warping of the paper when wet.

The images were then imported into MATLAB to undergo image processing to create square binary images. The binary images corresponding to the images in *Figure* 4.4 are shown in *Figure* 4.5. The logical OR and AND operations were then applied to the images, yielding the results in *Figure* 4.6

4.2.3 Operating Frequencies

The operational frequency range of the microwave oven was determined by measuring its electromagnetic leakage in a shielded anechoic chamber. The microwave was tested with a glass of water in it and with the slab of polystyrene in it to examine the shift when an absorbing body was present and to simulate the conditions of hotspot measurement.



Figure 4.4: The near fields inside the microwave oven as shown on thermal paper.



Figure 4.5: Process Binary Images of the Measured Near Field.

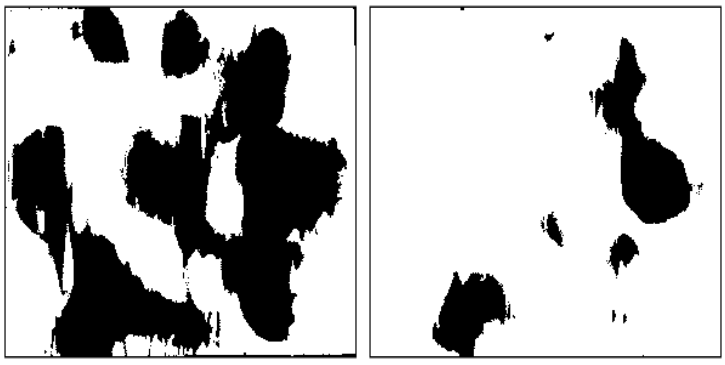

(a) Logical OR Operator (b) Logical AND Operator

Figure 4.6: Logical Operations on the Binary Images.

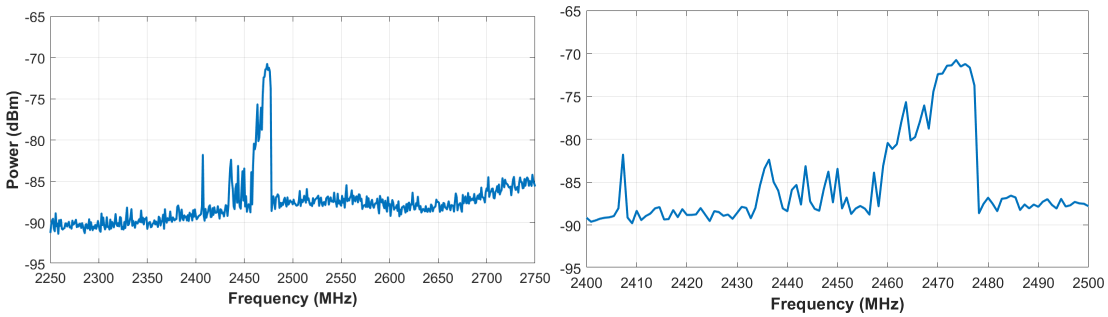

Figure 4.7: Microwave Leakage with a Glass of Water.

Since the power spikes would shift through frequency, the spectrum analyser was set to trace and hold the maximum value of the envelope instead of a continuous sweep.

Multiple microwave orientations were used, and multiple iterations of resolution bandwidth (RBW) were used on the spectrum analyser. The tests where the front of the microwave was facing the LPDA and an RBW of 300 kHz was used yielded the clearest results. The frequency range was set to 2.25–2.75 GHz, centred around 2.5 GHz as this was simply easier to set up than 2.2–2.7 GHz. These results are shown in *Figures* 4.7 and 4.8.

There are multiple frequencies at which the microwave oven operates. It was noted that when the glass of water was present in the microwave, the operational frequency underwent more change than when the polystyrene was placed within the oven. This resulted in a much narrower operational frequency band when only the polystyrene was present. Additionally, the glass of water heated up, indicating it was absorbing microwave energy, whereas the polystyrene sheet did not, meaning it did not absorb the microwave energy and convert it to heat. Instead, with the polystyrene, the top and sides of the oven became quite warm.

From the images, it was determined that with the presence of a dielectric body, the microwave operates anywhere between 2.43 GHz and 2.48 GHz, but predominantly in the range of 2.46–2.48 GHz. There was a minor spike in the 2.40–2.41 GHz range, which could be an outlier from other sources as it does not appear consistently. Without an absorbing body, the operational frequencies are localised entirely to the 2.46–2.47 GHz range. Therefore, in FEKO, the range of 2.4–2.5 GHz was simulated with a frequency increment of 1 MHz to try to pinpoint the pattern at the operational frequencies while providing some leeway on either side of the measured band.

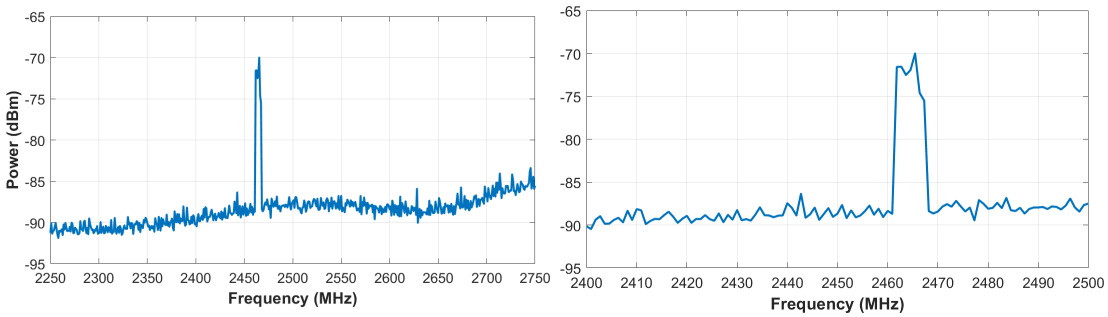

Figure 4.8: Microwave Leakage with a Sheet of Polystyrene.

4.2.4 Simulated Fields

Setting up Model and Solver

Since the empty cavity itself has a complicated geometry, even after removing the small, curved edges and insignificant geometric features, the attempts to speed up simulation time by using MFLMM instead of pure MoM failed because the iterative process would not converge, even when allowing for additional stabilisation.

Multiple runs were performed to account for the presence of the dielectric body inside the microwave: the lack of any dielectric, the presence of a polystyrene sheet, and the presence of a Styrofoam sheet. With the addition of the dielectric, an entirely MoM solution proved to be problematic owing to impractical memory requirements. The simulation required too much memory and needed to allocate out of core memory on the hard drive to solve the problem, which was not supported for dielectric solvers in FEKO.

Pairing MoM with FEM by solving the structure using MoM and the dielectric using a decoupled iterative FEM solver, as described in [55], did not work as the FEM iterations would not converge. The final solution was obtained by coupling the MoM solution of the cavity with the FEM dielectric solver utilising the direct sparse solver instead of an iterative process. Coarse meshing was required to remain within memory allocation and the MoM matrix had to be released from memory before the dielectric could be solved.

Results

Several simulated frequency points contained hotspots that corresponded to the measured hotspots as expected. The most applicable range was between 2.44–2.5 GHz range, which is consistent with the measured data in *Figures* 4.7 and 4.8. There were four major patterns evident within this range. These were best presented at 2.442, 2.459, 2.489 and 2.497 GHz. The corresponding patterns are shown in *Figure* 4.9. For these simulations,

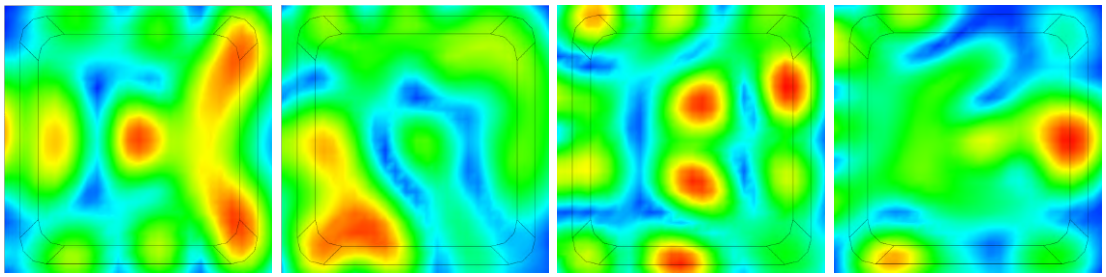

(a) 2.442 GHz (b) 2.459 GHz (c) 2.489 GHz (d) 2.497 GHz

Figure 4.9: Simulated Operational Fields inside the Microwave Oven for 2.4–2.5 GHz with Styrofoam as a Dielectric.

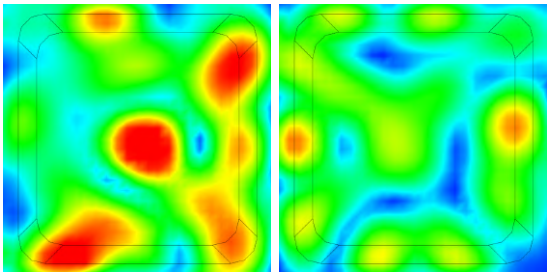

(a) 2.33 GHz (b) 2.35 GHz

Figure 4.10: Simulated Operational Fields inside the Microwave Oven for 2.33–2.35 GHz with Polystyrene as a Dielectric.

Styrofoam was the dielectric that appeared most similar to the measured results.

Incidentally, another set of frequencies were found that matched the measured data, however, they fell outside the range of 2.4–2.5 GHz. They were 2.33 and 2.35 GHz. Additionally, these patterns resulted from the polystyrene simulation, not the Styrofoam. These patterns are shown in *Figure 4.10*. It is possible that the dielectric characteristic shifted the resonant frequencies such that the operational range lowered.

4.2.5 Comparison

To compare the results, the FEKO simulations were processed in MATLAB in a similar fashion to the photographs. They were imported, resized, converted to double format, converted to grayscale, made binary around a threshold of 0.5 and padded. The logical OR operator was then applied to all the images. This was compared to the binary OR image of the measured data in *Figure 4.11*. The images appear similar and exhibit hotspots in largely the same areas, enough to verify the simulation package. Throughout the process of verifying the results, some inherent error was always present, which accounts for the slight discrepancy in *Figure 4.11*. This is discussed in *Section 4.2.6*.



(a) Styrofoam within Range. (b) Measured Image. (c) Polystyrene outside Range.

Figure 4.11: Comparison of the Simulated and Measured Binary Images.

4.2.6 Error

The slight error between the measured and simulated fields could be attributed to several reasons.

Simulation

When developing the CAD model of the microwave oven, slight error owing to approximating the dimensions could have resulted. Only a ruler and measuring tape were used to measure the dimensions of the oven which can be inaccurate on curved surfaces. Additionally, the interior geometry of the microwave was difficult to measure owing to access restrictions. It is difficult to fit and manoeuvre measuring equipment inside the cavity. This was mitigated as much as possible by removing the microwave casing and measuring the external and internal dimensions in multiple locations. Additionally, all indents in the microwave walls were measured by marking a spacer placed inside the indents to allow for easier measurement.

The metal of the cavity in FEKO was modelled as a Perfect Electrical Conductor or PEC. A good conductor, such as the metallic walls of a microwave oven, are characterised by very large electric conductivity [24]. PEC's are characterised by essentially infinite electric conductivity, with the additional boundary condition of $\mathbf{n} \times \mathbf{E} = \mathbf{0}$, meaning the tangential electric field component on the surface of the conductor is zero [56]. Therefore, the microwave oven walls are not a PEC, as it has a finite, albeit very high, conductivity; however, conventionally, electromagnetic simulation models metal as a PEC.

Lastly, in the model, all slight smooth curvatures on the edges in the microwave had to be removed and replaced by corners. This is because the mesh on the fully curved model was incredibly fine around the curvature resulting in infeasible memory requirements and simulation time. Therefore, only the major curvatures were left smooth and the minor

smooth, curved edges were replaced by sharp corners. By and large, this alteration was considered negligible to the overall pattern, as the bevels that were removed were all under the tenth-of-a-wavelength design convention in their curvature, resulting only in slight scattering at the sharp edges of the cavity. Given that for many programs, the model mesh sizes, as a rule of thumb, are maximally limited at $\lambda/10$, it is possible that the curvatures would not be evident in the mesh structure anyway.

Measurement

As with many measurements, there is always some degree of inherent error involved. Since two methods of measurement were used in this investigation, there were two areas of potential measurement error. These were the measuring of the operational frequencies of the microwave oven and the measuring the hotspots within the microwave, each with their respective errors.

To minimise measurement error while measuring the operating frequencies of the microwave, the tests were conducted in the shielded anechoic chamber at Wits. This eliminated interference from outside sources and unwanted reflection off the walls. However, because the microwave's 'start' button had to physically be pressed, I had to remain in the chamber during the measurement process, meaning the door had to remain slightly ajar. This could have potentially introduced interference from outside sources like WiFi and Bluetooth devices outside the chamber. Again. this error was deemed negligible as the interference signal would be tiny compared to the microwave energy from the oven.

Lastly, the investigation was to determine the field pattern inside the microwave. The method to determine the operating frequencies of the oven measured the external leakage of the oven. The safety features that keep the field as contained as possible could have interfered slightly with the resulting leakage spectrum.

The error of the near field testing method was largely owed to the frequency shifting of the magnetron. The phenomenon led to largely unrepeatable results. Additionally, the thermal paper appeared to exhibit the microwave heating effect and hence, turn dark, more when the wet paper was in contact with the polystyrene, instead of raised above it. Since the paper warped randomly when wet, this introduced an additional element of inconsistency. To mitigate these errors as much as possible, the experiment was conducted multiple times.

4.2.7 Conclusion

It has been demonstrated that the FEKO simulation exhibited similar hotspots to the actual microwave at a frequency range of 2.44–2.49 GHz, despite the documented in-

consistency of microwave resonant field patterns. It was concluded that FEKO is an acceptable, accurate simulation platform for resonance problems consisting of near field pattern simulations bounded by a resonant cavity. Given that CST Studio and FEKO produce the same output for similar problems, as demonstrated by *Figure* 4.1, it was concluded that both CST Studio and FEKO are appropriate.

4.3 Cavity Characterisation

The characterisation of the new 'ideal' model, its resonance characteristics and the effects of a dielectric on the field are presented in this section.

4.3.1 Waveguide Resonator

As discussed in *Section* 3.3.2, the resonance of the WR340 waveguide was determined analytically, a resonance study in HFWorks and using a frequency sweep in CST Studio and FEKO. To examine the resonance of the waveguide structure in isolation, the waveguide was bounded or enclosed, to become its own resonant cavity. Using *Equation* (3.3) in *Section* 3.3.3, it was found that the WR340 has only one dominant characteristic mode between the frequencies of 2.2 ad 3.3 GHz, which is at 2.4547 GHz, corresponding to wavenumber 51.4461 and mode TE_{101} in three dimensions.

The resonance study conducted in HFWorks agreed with the analytic data. The study calculated the first 10 modes of the system. *Table* 4.2 shows the frequency at which the first 5 modes occur. The first resonant mode is at $\approx$ 2.454 GHz, followed by the second at $\approx$ 3.877 GHz, outside of the range of 2.2–3.3 GHz. Modes 3–5 also clearly refer to the same frequency as mode 2. The resultant electric field from mode 1 is shown in *Figure* 4.12, simulated by HFWorks. The expected singular column is present.

Table 4.2: Resonant Modes of the WR340 Waveguide.

Mode Index	**Frequency (GHz)**
Mode 1	2.4539
Mode 2	3.8769
Mode 3	3.8771
Mode 4	3.8787
Mode 5	3.8799

Additionally, a frequency sweep of the closed waveguide with a waveguide feed on the one end was conducted in CST Studio and FEKO. The results, shown in *Figure* 4.13 show that the clearest, symmetrical hotspot was evident at 2.45 GHz, as expected, corresponding to the first resonant mode. Also, the near fields at 2.2, 3.3 and 2.7 GHz

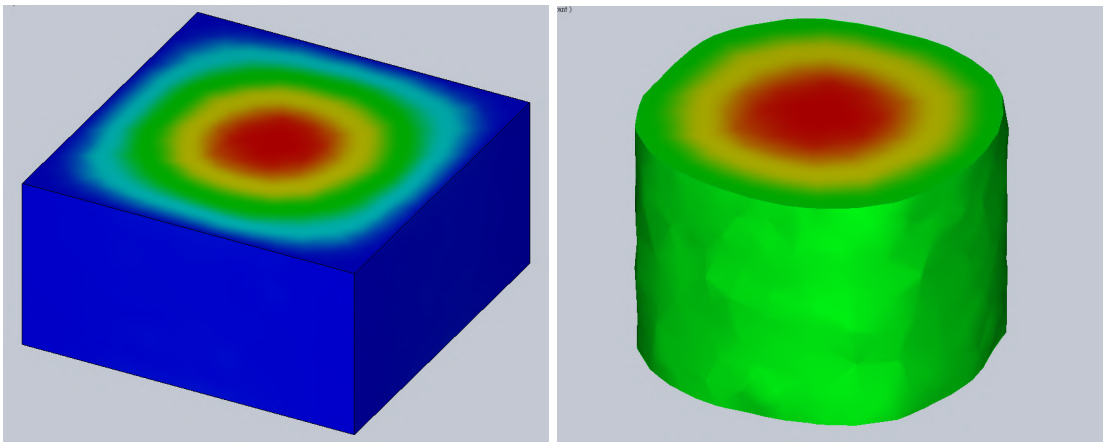

(a) No clipping (b) Iso clipping

Figure 4.12: Electric Field from the Resonant Study of the Bounded WR340 Waveguide.

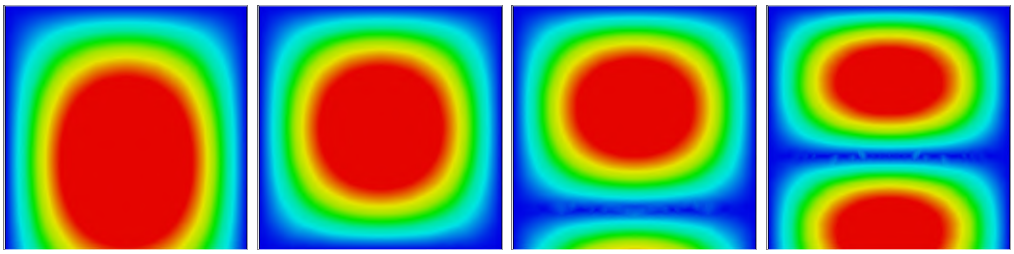

(a) 2.2 GHz (b) 2.45 GHz (c) 2.7 GHz (d) 3.3 GHz

Figure 4.13: Excitation of a Bounded WR340 Waveguide with Different Frequencies.

are shown. This demonstrates that between 2.2–2.7 GHz, the dominant mode is indeed TE_{10}, as there is a single major hotspot evident in the waveguide. At 3.3 GHz, it appears like TE_{20} starts becoming more dominant, indicating 2.2–2.7 GHz was the ideal frequency range for the waveguide.

4.3.2 Cavity Resonance

The frequency sweep of the ideal cavity between 2.2 and 2.7 GHz yielded many different patterns. Technically, the ability of the cavity to resonate relies on the waveguide resonator, as the waveguide feeds the cavity and hence, must resonate itself. Therefore, the cavity is bounded by the same frequency limitations as the waveguide. However, enclosed cavities have their own natural resonant frequencies which can be described by *Equation* (3.3) in *Section* 3.3.3.

The dominant resonant mode will tend towards the mode number combination where at least one mode number is zero [57]. *Table* 4.3 shows all 18 resonant modes that fall within the frequency range of 2.2–2.7 GHz for the selected cavity geometry.

Table 4.3: Resonant Modes of Cavity between 2.2 and 2.7 GHz

Frequency (GHz)	**Wave Number**	**TE Mode**		
		m	n	l
2.3856	49.9966	1	0	4
		4	0	1
		2	1	3
		3	1	2
		0	2	1
		1	2	0
2.4547	51.4461	3	0	3
		1	2	1
2.5875	54.2289	2	0	4
		4	0	2
		0	1	4
		4	1	0
		0	2	2
		2	2	0
2.6514	55.5681	1	1	4
		4	1	1
		1	2	2
		2	2	1

This table was generated by MATLAB which iteratively selected each mode combination that resulted in a resonant frequency that fell in the frequency range. m, n and l are integers that represent the radial, angular and longitudinal mode orders respectively. As shown, many TE modes can be represented by a single frequency and wavenumber. This could be because each dimension of the cavity is not unique, with the length and the width being equivalent, as noted in *Table 3.3*. Since length and width are equal in the model, mode parameters m and l are effectively interchangeable in the calculation in *Equation (3.3)*, creating some ambiguity in the mode numbers.

The modes can be visualised as how many hotspots are evident in each direction. The m dimension refers to the **H** direction of the waveguide, or the width of the cavity. The n direction is the **E** direction of the waveguide, or the height of the cavity, and l refers to the length or depth of the cavity.

The table shows the natural resonant frequencies of only the closed cavity, so when the cavity is fed with a rectangular waveguide, the geometry is slightly altered, so the resonant frequencies of the system can be expected to change slightly. To calculate the natural resonance of the system consisting of the cavity and the waveguide, the analytical solution becomes trickier and software packages were used to find the resonant peaks through simulating the internal electric near fields of the system.

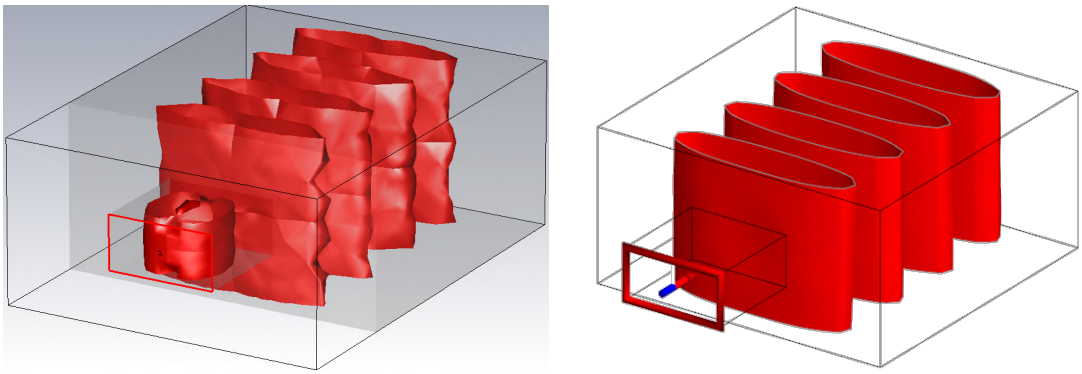

(a) CST Studio Isosurface. (b) FEKO Isosurface.

Figure 4.14: E-Field Pattern of the Cavity at 2.386 GHz, exhibiting Mode TE_{104}.

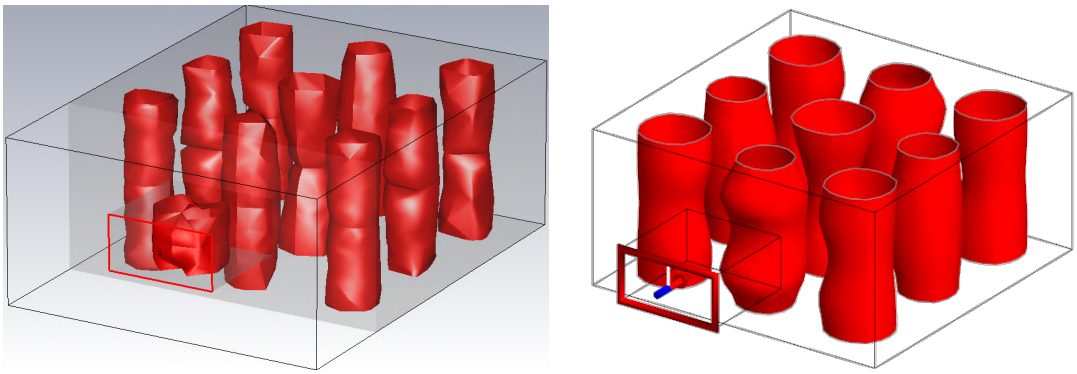

(a) CST Studio Isosurface at 2.455 GHz. (b) FEKO Isosurface at 2.454 GHz.

Figure 4.15: E-Field Pattern of the Cavity exhibiting Mode TE_{303}.

Figures 4.14, 4.15 and 4.16 show the 3D electric field within the resonant cavity at the approximate frequencies at which its various characteristic modes were expected to be found in both CST Studio and FEKO. For *Figure* 4.14, at 2.386 GHz, mode TE_{104} can clearly be seen. In *Figure* 4.15, 2.454 and 2.455 GHz, mode TE_{303} is clearly observed. In this case, CST Studio and FEKO exhibited this pattern 1 MHz apart from each other. At 2.588 GHz, no clear resonant mode that matched any of the expected modes from *Table* 3.3 was found. *Figure* 4.16, at 2.651 GHz, clearly shows mode TE_{122} as expected.

These simulations also reinforce that the programs CST Studio and FEKO yield the same results. In CST Studio, the standard FEM Frequency Domain solver was used and in FEKO, MLFMM was used.

4.3.3 Bandwidth

Because the cavity is an empty closed structure, there is nothing to 'absorb' the microwave energy, meaning a large amount of energy will be 'reflected' towards the microwave source. This means that the VSWR is always going to be high and trying to

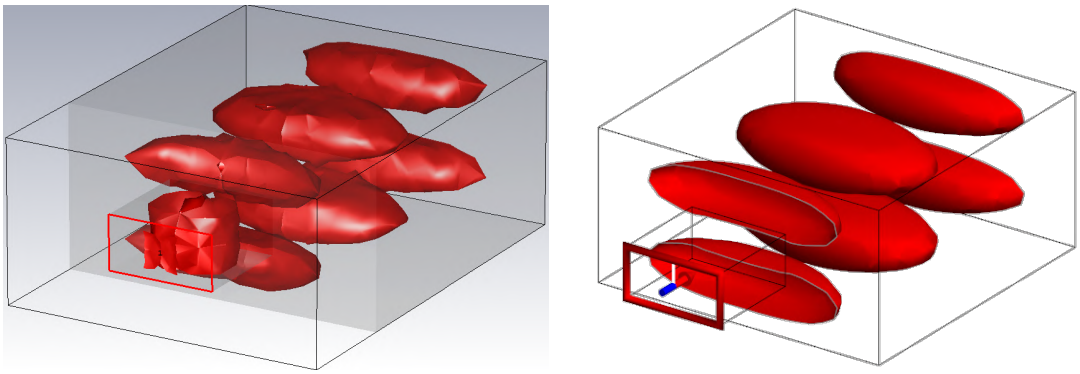

(a) CST Studio Isosurface. (b) FEKO Isosurface.

Figure 4.16: E-Field Pattern of the Cavity at 2.651 GHz, exhibiting Mode TE_{122}.

determine the resonant frequency and bandwidth based on classic VSWR ≤ 2 is impractical. Instead, the bandwidths of the eigenfrequencies, in *Table* 4.3 were determined based on how 'narrow' the frequency band was in which each mode presented. In other words, how much could the frequency be shifted and still be within the resonant peak? The bandwidth was found to be very narrow.

Frequency intervals of 100 kHz on either side of the found resonant peak were examined. This was a very fine frequency interval considering the frequency range, which is in the GHz. CST Studio has a function to plot the maximum absolute electric field strength of each simulated frequency on a 1D graph. This result lends visualisation for the location of the various resonant peaks. *Figures* 4.17 and 4.18 present the findings of this investigation. Note that the plots have been cut off at the top, as the resonant peaks dwarf the rest of the data. *Figure* 4.17 plots the global maximum field value at each simulated frequency, while *Figure* 4.18 plots the accepted power for the frequency range. Three resonant peaks were found in this frequency range. Additionally, the bandwidth of each of these peaks is very narrow. CST Studio could not simulate a finer interval than 100 kHz, so FEKO was used to investigate the individual resonant peaks.

Figure 4.19 shows the radiated power across the full frequency range. The initial simulation was conducted with an interval of 1 MHz. As shown, there is a clear resonant peak just after 2.65 GHz, corresponding to the 4th characteristic mode of the system. Modes 1 and 2 were not visible and mode 3, as discussed, was not presenting. A finer frequency interval of 50 kHz was simulated over the expected region of modes 1 and 2. These results were added to the graph and are shown as the green and red spikes, respectively. Unlike mode 4, these peaks are so narrow, they appear almost anomalous. Therefore, an even finer simulation with a resolution of 10 kHz was conducted over those modes. Each simulation was examined individually. These simulations are shown in *Figure* 4.20.

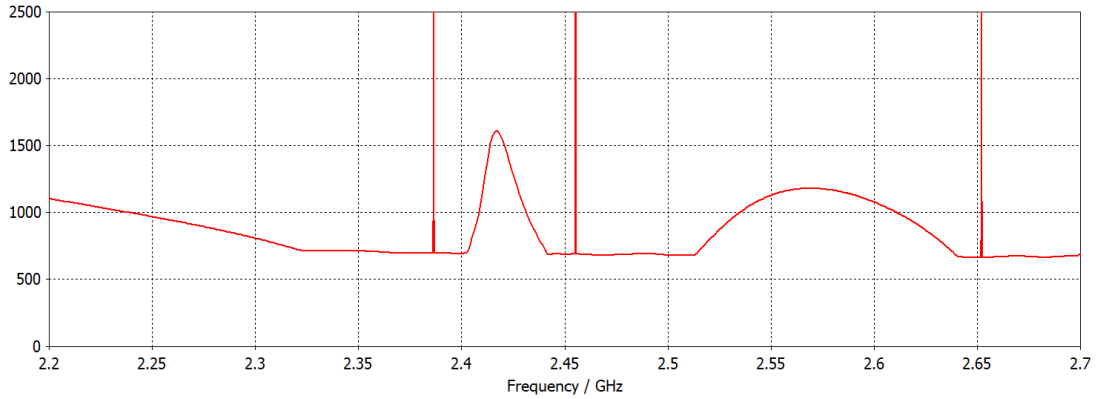

Figure 4.17: Maximum E-field value across the Frequency Range in CST Studio.

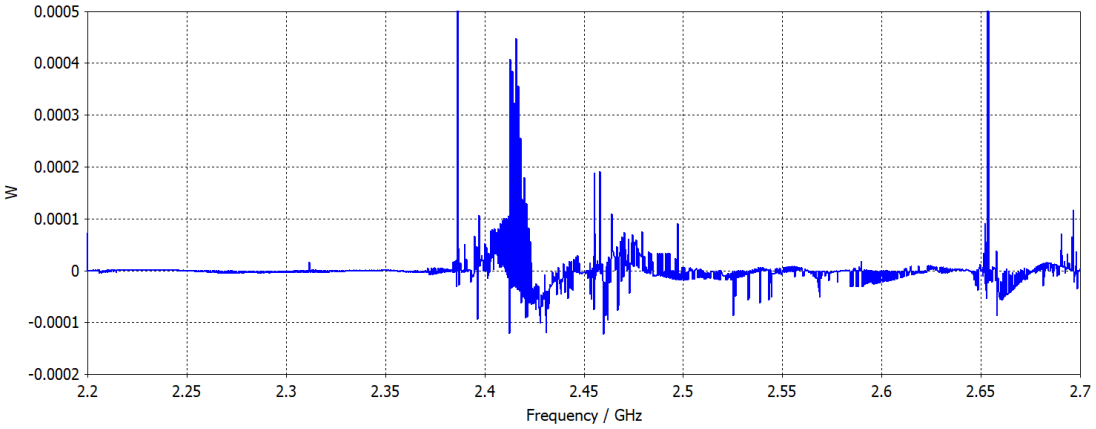

Figure 4.18: Accepted Power across the Frequency Range in CST Studio.

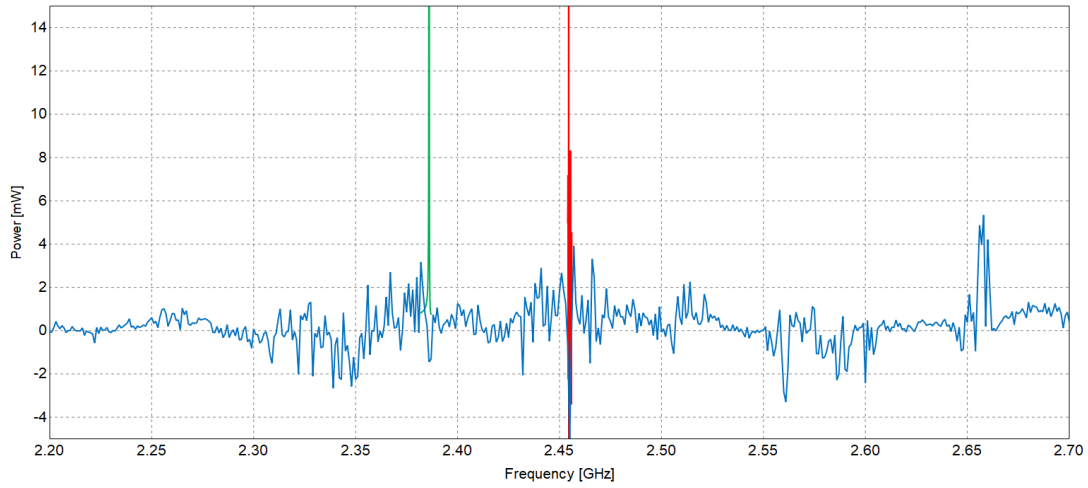

Figure 4.19: Radiated Power across the Frequency Range in FEKO.

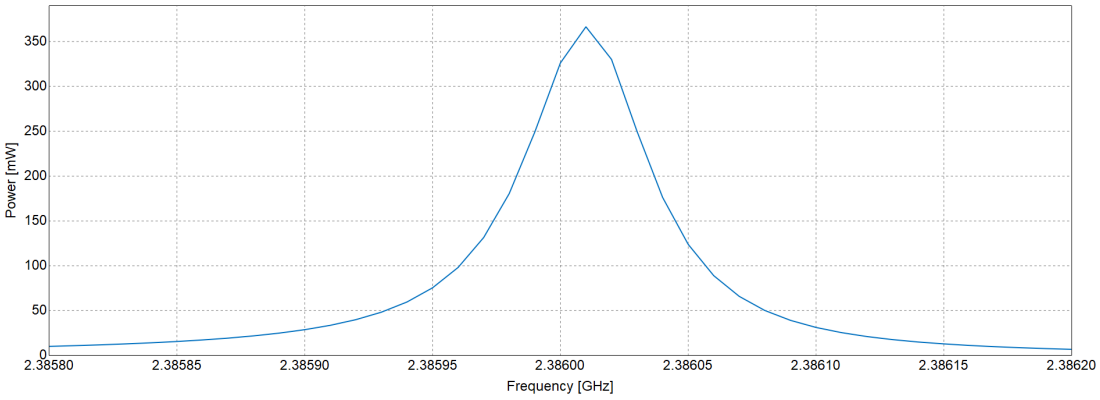

(a) Mode 1.

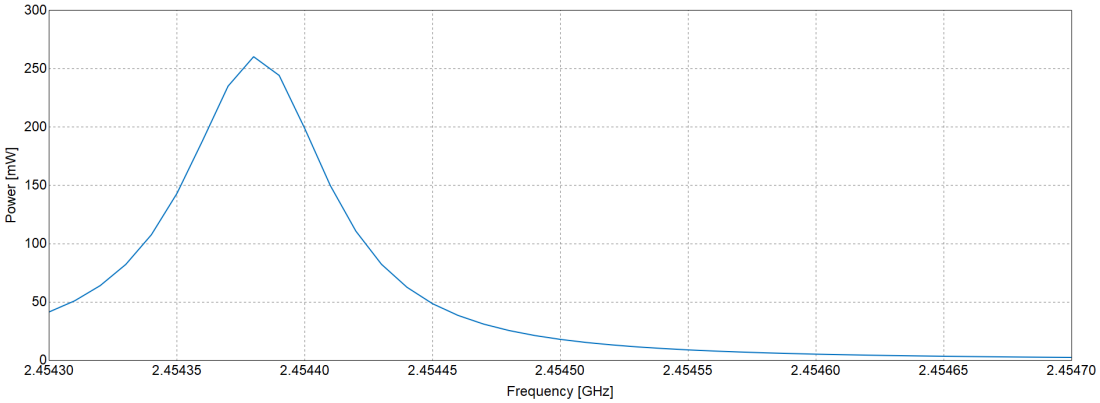

(b) Mode 2.

Figure 4.20: Radiated Power at the Characteristic Modes in FEKO.

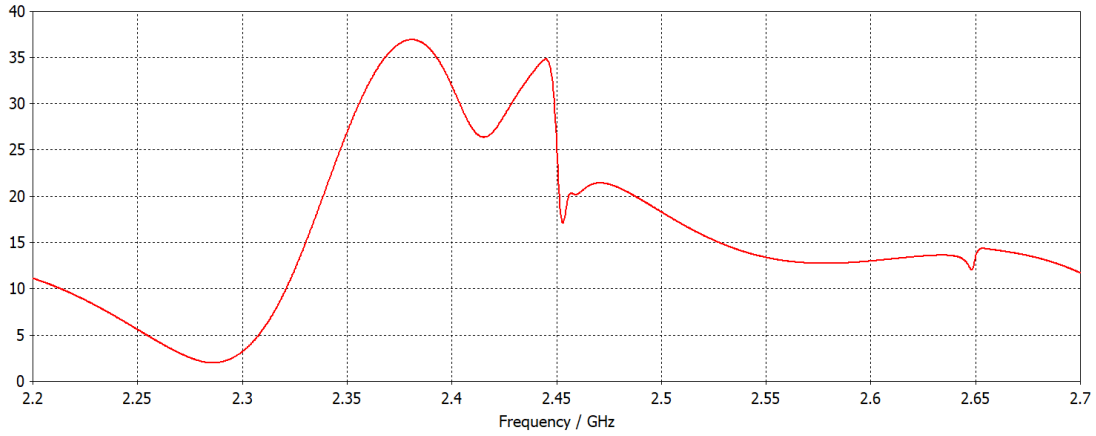

Figure 4.21: VSWR of Cavity with Water in CST Studio.

Figure 4.20 shows how narrow the bandwidth of the two modes is. In each case the entire horizontal axis represents 400 kHz. Therefore, the bandwidth of the peaks is $\approx$ 100 kHz, which is tiny in the microwave frequency spectrum. Each simulation comprised 41 data points, so the peaks are not numerical anomalies. At mode 4, in CST Studio, the bandwidth was $\approx$ 200 kHz, however, in FEKO, there appears to be a peak with many oscillations over about 10 MHz, indicating an inconsistency in the solver methods at that characteristic mode. This inconsistency could indicate a numerical anomaly in CST, or it could indicate that the peak resides in a slightly different frequency range depending on the solver method and hence, was not discovered by FEKO. Regardless, this demonstrates the incredible fine bandwidth of the resonance in the cavity.

4.3.4 Dielectric Influence

An investigation was conducted into the effect of a dielectric body on the resonance within the chamber. A new frequency sweep with the presence of a water cylinder was conducted in CST Studio. The VSWR, accepted power and maximum electric field strength were examined.

Since the water absorbs the electromagnetic energy, the VSWR was kept to a reasonable value at some frequencies, with a minimum of 1.975 and 2.286 GHz, as shown in *Figure* 4.21. The maximum accepted power of 0.446 W was also evident at this frequency, shown in *Figure* 4.22. For this simulation, all accepted power was absorbed by the dielectric. A new maximum electric field strength graph was generated and the results presented in *Figure* 4.23. This shows a maximum electric field intensity at 2.313 GHz, which corresponds approximately with the minimum VSWR and maximum accepted power. At 2.634 Ghz there is also an area of high field strength.

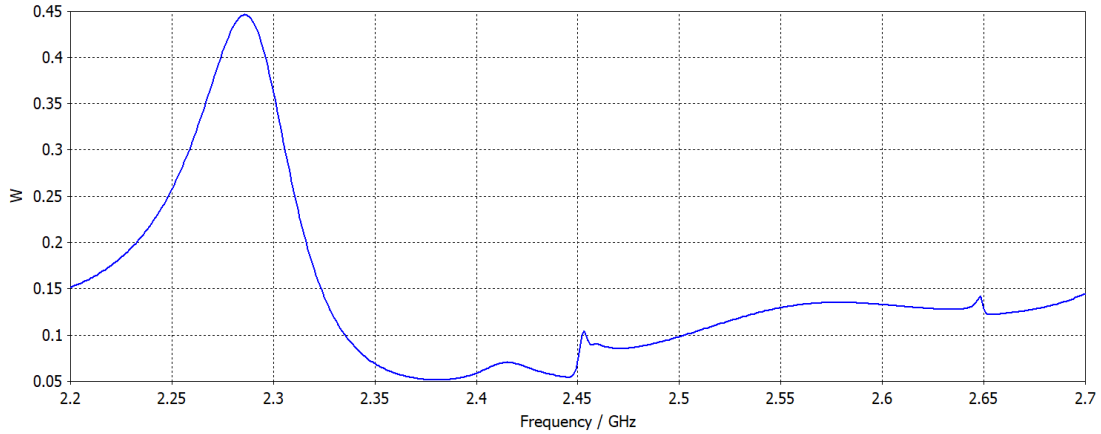

Figure 4.22: Accepted Power of Cavity with Water in CST Studio.

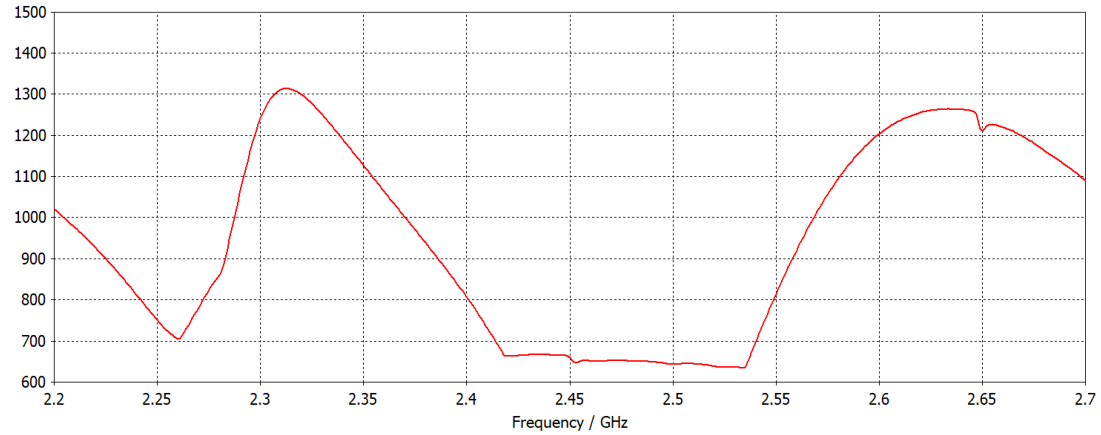

Figure 4.23: Maximum Electric Field of Cavity with Water in CST Studio.

Firstly, it is clear to see that the presence of the dielectric severely influences the behaviour of the eigenfield. Power in this case is absorbed, which warps and changes the resonance. This is initially evident from the complete lack of resonant peaks in the frequency sweep conducted. Additionally, the system is most 'stable' at 2.286 GHz, which does not correspond to any of the resonant peaks of the empty cavity or the previously calculated characteristic modes.

Figure 4.24 presents the results of an investigation into the effects of a dielectric on the near field pattern within the system. For this investigation, the near fields were examined with and without the presence of water. Additionally, the instantaneous electric field strength was compared to the average electric field strength. This investigation essentially involves the Poynting Vector, which described the directional energy flux vector of an electromagnetic field. The *instantaneous* Poynting Vector describes an instantaneous power flow resulting from an instantaneous electric and magnetic field pair. Because the cavity was fed essentially with a sinusoidal signal of a given frequency or set of frequencies, there would be an instantaneous Poynting Vector for each phase of the sinusoid. In practice, the time averaged Poynting Vector is used because the sinusoid oscillates continuously, causing the vector to likewise oscillate.

The significance of the presence of dielectric material in an instantaneous field is that the dielectric would interact with the instantaneous field. Because of the complex permittivity of water, the interaction would imply an imaginary component, j, being multiplied by the instantaneous field, which would contain both real and imaginary components. This would result in real components of the field becoming imaginary and the imaginary parts becoming real. This is the phenomenon that results in heating from the microwave heating effect discussed in *Section* 2.3.2.

Figure 4.24 shows the instantaneous interaction of the field with the water. For the images on the right, without water, the field pattern itself does not change when the instantaneous phase is changed. The absolute field strength simply increases or decreases. Therefore, the average electric field pattern is identical for each iteration of instantaneous phase, with average absolute strength. The images on the left have water in them. In those images, the field pattern itself changes slightly when the instantaneous phase changes. This is because both the magnitude *and* direction of the instantaneous field are affected by the complex dielectric, water. The average electric field is then of average field strength *and* the average field pattern. The complex permittivity of water also explains why the instantaneous absolute electric field strength with water is highest when the strength without water is lowest.

From this, it can be concluded that the resonance within resonant cavities is very sensi-

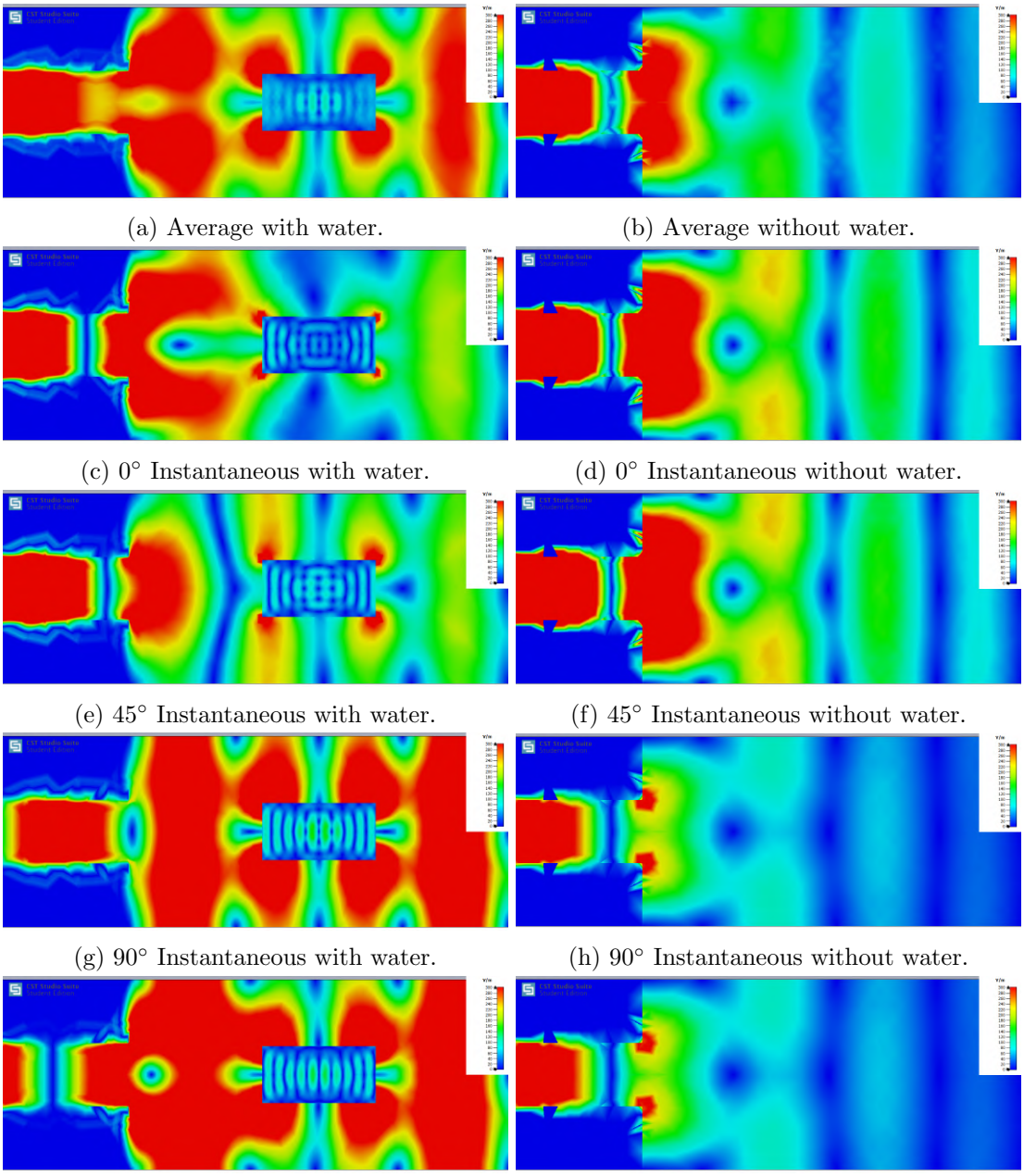

(a) Average with water.

(b) Average without water.

(c) 0° Instantaneous with water.

(d) 0° Instantaneous without water.

(e) 45° Instantaneous with water.

(f) 45° Instantaneous without water.

(g) 90° Instantaneous with water.

(h) 90° Instantaneous without water.

(i) 135° Instantaneous with water.

(j) 135° Instantaneous without water.

Figure 4.24: Comparison of Near Fields With and Without Water in the Cavity.

tive to the presence of dielectrics, which may completely change the system characteristics. Thus, the resultant fields obtained from one body of dielectric will not match the resultant fields in the presence of a different dielectric.

4.4 Hotspot Manipulation: Frequency Shifting

Given the many different patterns in simulation over the large frequency band, as evidenced by the resonant modes and eigenfrequencies, an investigation was conducted to observe the change in field pattern based on small changes in input frequency, again over a frequency range of 2.2 - 2.7 GHz. Given the very narrow bandwidth of the characteristic modes of the cavity, these discreet frequencies were infeasible to investigate. It was noted, however, from *Figure* 4.17, that from about 2.52 GHz until 2.7 GHz, the maximum field strength was relatively steady and smooth, with only the single characteristic mode at 2.6522 GHz evident within the range. Upon examination of the field patterns in the frequency band, the range of 2.6 - 2.7 GHz was selected for examination, as clear hotspot movement was evident.

4.4.1 2.6 - 2.7 GHz

In the model, the frequency span of 2.6 to 2.7 GHz exhibits a pattern with relatively high resilience, as the pattern itself does not change much, the hotspots are only shifted, as shown in *Figure* 4.25. The hotspots midway through the cavity move left to right with frequency, away from the waveguide.

A 1D line was calculated through the top hotspot from wall to wall within the cavity and the magnitude plotted in *Figure* 4.26. In the plot, the waveguide sits to the right of the graph, with the middle local maxima showing the distance of the central hotspot along the z-axis from the front wall. The hotspot shifts progressively through frequency.

In MATLAB, the position data of the local maximum was plotted against frequency and a line of best fit was generated using the polynomial fitting function with first and

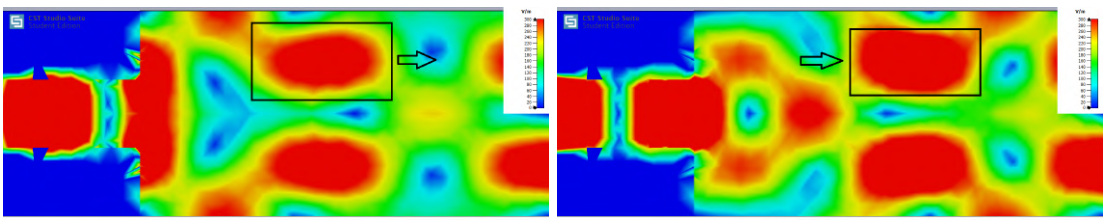

(a) 2.6 GHz (b) 2.7 GHz

Figure 4.25: Longitudinal Contour of Near Field Pattern at 2.6 and 2.7 GHz.

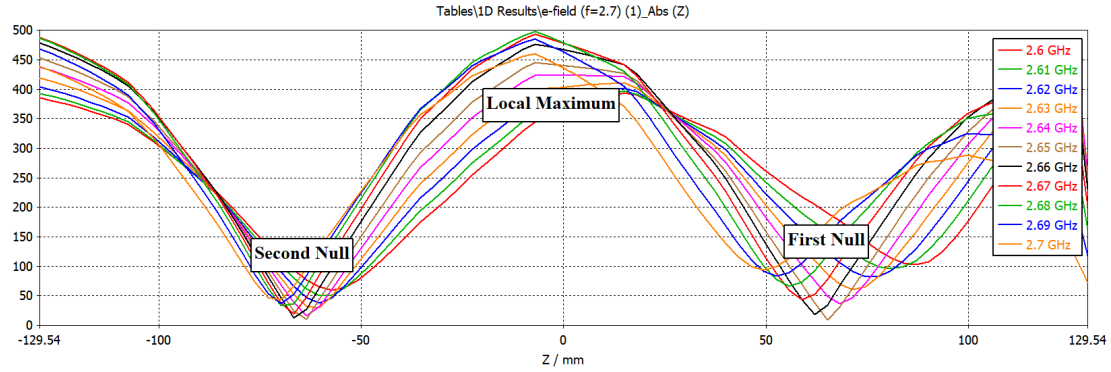

Figure 4.26: Plot of Field Magnitude through Top Hotspot from 2.6 GHz to 2.7 GHz.

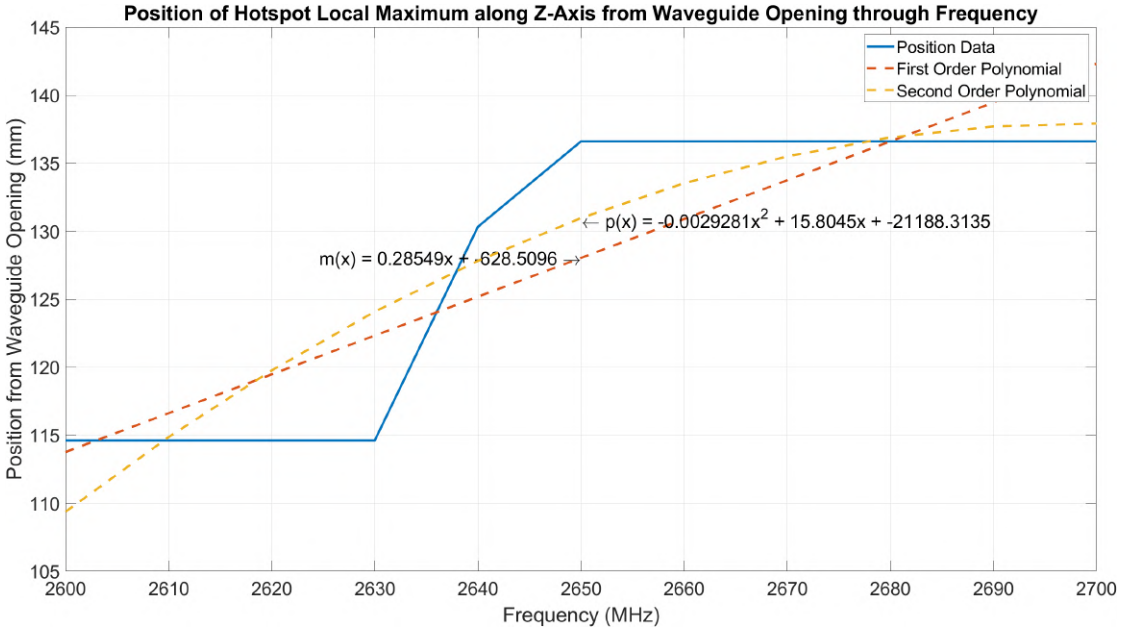

Figure 4.27: Position of Maximum along Z-Axis from Waveguide against Frequency.

second order polynomials. This plot is shown in *Figure* 4.27. The position data is rather stepped and uneven, with 'flat' sections of the curve and as such, no first or second order polynomial fits the curve well, therefore the nulls, which are far sharper, were tracked. The nulls are demarcated as 'First Null' and 'Second Null' in *Figure* 4.25. These graphs are shown in *Figures* 4.28 and 4.29.

When the nulls are tracked, the data fits very well to both first and second order polynomials, particularly the first null. This clearly shows that the hotspot moves progressively with frequency in the range of 2.6 to 2.7 GHz.

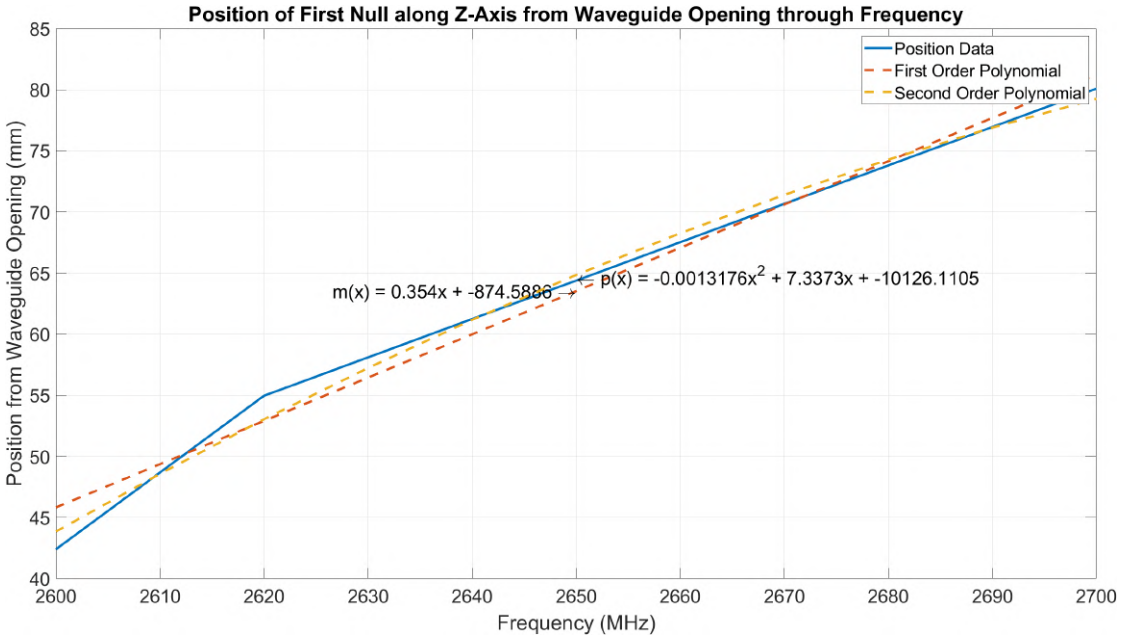

Figure 4.28: Position of First Null along Z-Axis from Waveguide against Frequency.

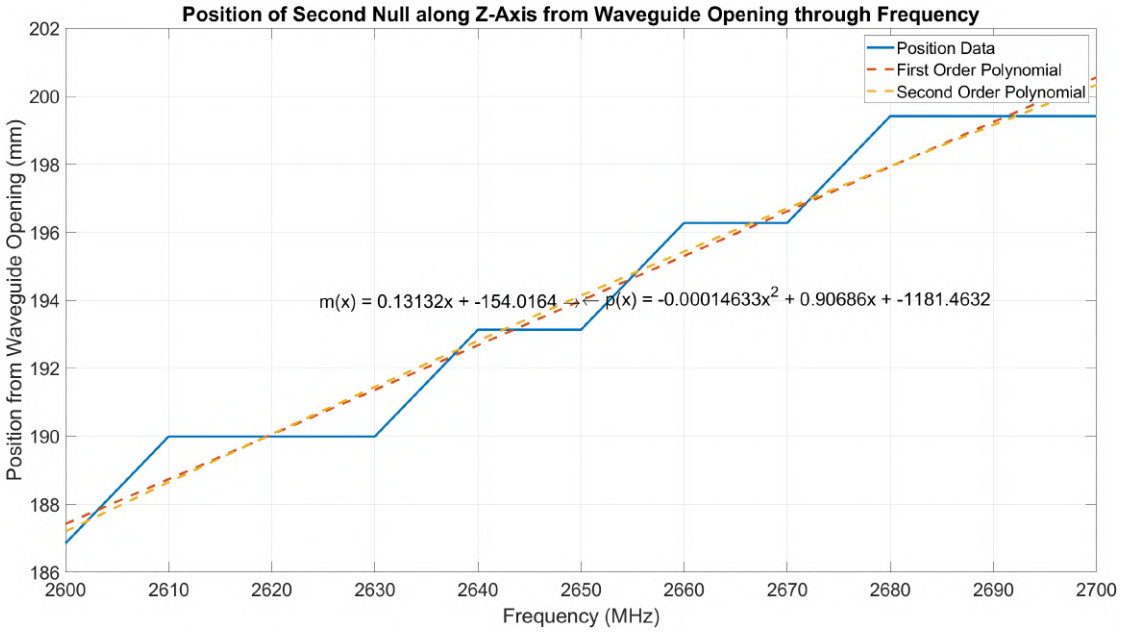

Figure 4.29: Position of Second Null along Z-Axis from Waveguide against Frequency.

4.5 Hotspot Manipulation: Phase Shifting

To investigate the influence of feed phase on hotspot placement, three models were created with various waveguide orientations, as shown in *Figure* 3.1, with waveguides on the same face, adjacent faces and opposite faces. The field patterns at each of the four resonant frequency modes, described in *Section* 4.3.2, were examined, along with three frequencies that lay in between these modes. For each of these cases, a phase shift was introduced iteratively between the sources, spanning 0° to 345°, with intervals of 15°. The presented simulations were all conducted in CST Studio owing to faster simulation time. The results were all corroborated by FEKO simulations. *Table* 4.4 summarises the frequencies used in each model in CST Studio. All images of the field patterns are displayed as a 2D contour coloured display where possible and as a 3D iso-surface where more appropriate.

Table 4.4: Frequencies at which Phase Shift was Examined.

Model	**Frequencies (GHz)**						
	Resonant Modes				Other Frequencies		
Same Wall	2.3861	2.4478	2.5889	2.6513	2.4190	2.5010	2.6350
Adjacent Walls	2.3870	2.4550	2.5880	2.6440	2.3850	2.4210	2.6350
Opposite Walls	2.3870	2.4558	2.5880	2.6535	2.4210	2.4990	2.6350

4.5.1 Same Face

Resonant Modes

Initially, the model was simulated at its resonant mode frequencies calculated in *Section* 4.3.2 and the hotspot positions analysed for each iteration of 15° of phase. At 2.3861 GHz, or mode TE_{104}, shown in *Figure* 4.30, the hotspot positions themselves did not change much through phase, except around 180°, where the single row of wide columns transforms into two rows side by side, as expected because analytically, there is $0V$ down the centre if the sources are exactly out of phase.

The pattern is mirrored around 180° and the central axis. Therefore, 270° produces a mirror of 90°, 240° produces a mirror of 120° etc. A key difference is that the absolute maximums in the field decrease in intensity drastically. If the iso-surface threshold that allows the hotspots to be seen at 180° is used at 0°, almost the entire cavity becomes a hotspot. Therefore, the hotspot positions at this frequency did not change by any material amount when the phase is increased from 0° to 180° until they disappear owing to the feed phase mismatch. The hotspots appear again gradually when the phase is increased from 180° to 360°.

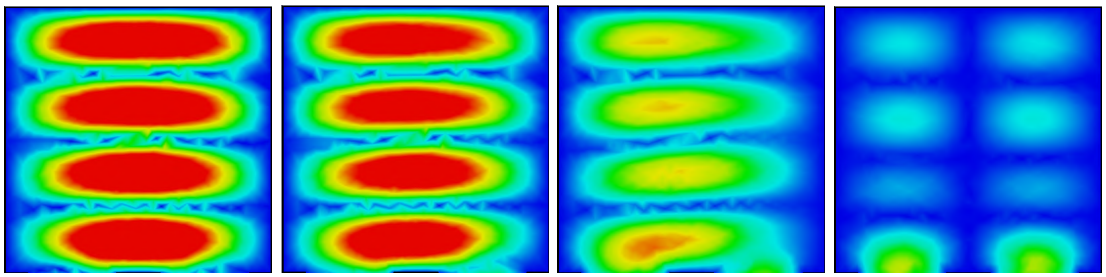

(a) 0° phase shift. (b) 60° phase shift. (c) 120° phase shift. (d) 180° phase shift.

Figure 4.30: The Effect of Feed Phase at 2.3861 GHz for the Same Face Model.

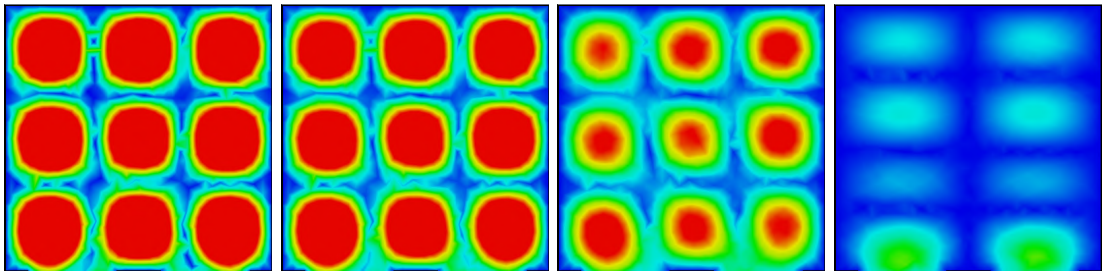

(a) 0° phase shift. (b) 60° phase shift. (c) 120° phase shift. (d) 180° phase shift.

Figure 4.31: The Effect of Feed Phase at 2.4478 GHz for the Same Face Model.

The same is true for the mode TE_{303} at 2.4478 GHz, shown in *Figure* 4.31 and for mode TE_{204} at 2.6513 GHz, in *Figure* 4.33. The hotspots do not change position until they disappear and then reappear again. At 2.4478 GHz and 180°, the pattern is almost identical to the pattern evident at 2.3861 GHz.

At 2.6513 GHz, however, the hotspots at 180° are in the same positions as they are throughout all phase and are only at a much lower magnitude. At 2.5889 GHz, shown in *Figure* 4.32, the field behaves differently. The resonant mode TE_{204} is only evident when there is a 180° phase shift between the sources. In this instance, as the phase shifts away from 180° to 0° and 360°, the hotspots disappear. In this case, the inverse of the previous two modes occurs, with the hotspots becoming more pronounced the closer to 180° the phase shift becomes. Again, the absolute maximum changes such that in essence, the hotspots cannot be tracked as they simply disappear. Therefore, at all the resonant modes evident in the system, the introduction of phase difference has no impact on hotspot placement, only on the field intensity.

Other Frequencies

At 2.419 GHz, a similar situation occurs where the hotspot positions do not undergo substantial change with source phase difference. The field intensity simply drops. This is shown in *Figure* 4.34. At 2.501 GHz, in *Figure* 4.35, there is a very slight movement

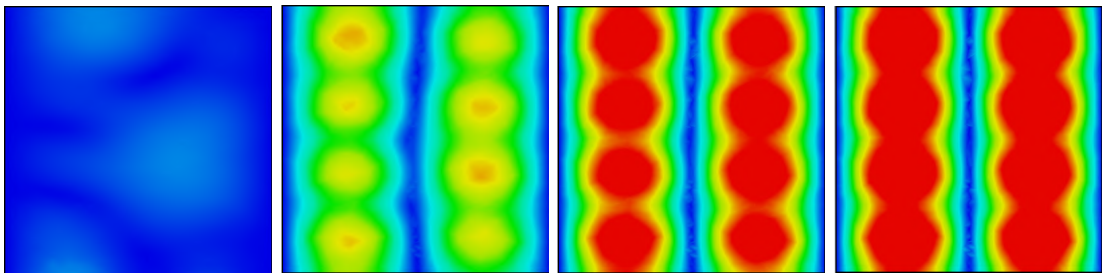

(a) 0° phase shift. (b) 60° phase shift. (c) 120° phase shift. (d) 180° phase shift.

Figure 4.32: The Effect of Feed Phase at 2.5889 GHz for the Same Face Model.

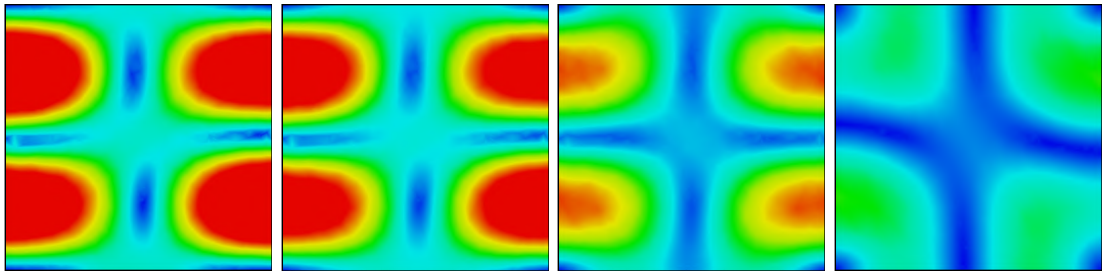

(a) 0° phase shift. (b) 60° phase shift. (c) 120° phase shift. (d) 180° phase shift.

Figure 4.33: The Effect of Feed Phase at 2.6513 GHz for the Same Face Model.

of the hotspot closest to the sources towards the leading waveguide, but the movement is negligible compared to the drop in field intensity through phase shift. At 2.635 GHz, the field intensity does not drop when the phase difference is altered, nor is there any evident hotspot movement. Instead, the hotspot configuration at 0° blends gradually into a completely new configuration at 180° phase difference, exhibiting no linear hotspot movement, as shown in *Figure 4.36*. Again, the conclusion can be drawn that the introduction of a phase difference does not move the position of a hotspot. Even at 2.635 GHz, where the placement is altered. In this case, the entire orientation of the hotspots is altered, which does not allow for controlled movement of the hotspot.

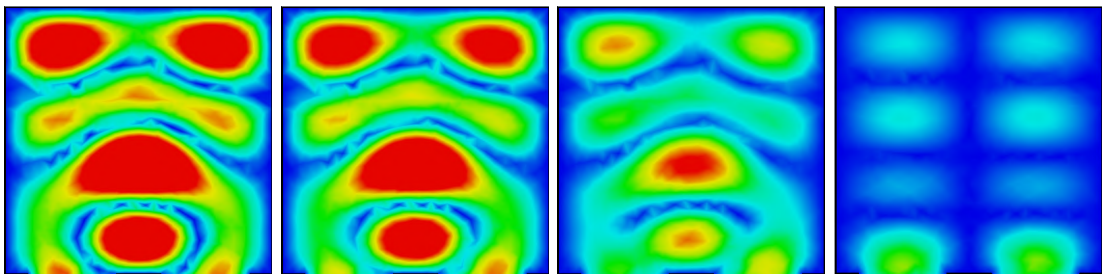

(a) 0° phase shift. (b) 60° phase shift. (c) 120° phase shift. (d) 180° phase shift.

Figure 4.34: The Effect of Feed Phase at 2.419 GHz for the Same Face Model.

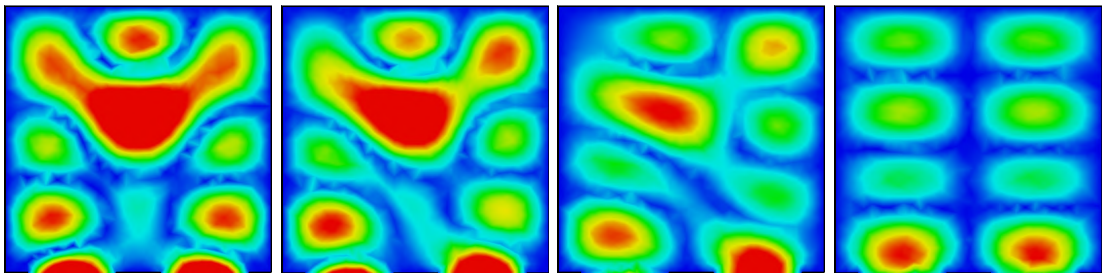

(a) 0° phase shift. (b) 60° phase shift. (c) 120° phase shift. (d) 180° phase shift.

Figure 4.35: The Effect of Feed Phase at 2.501 GHz for the Same Face Model.

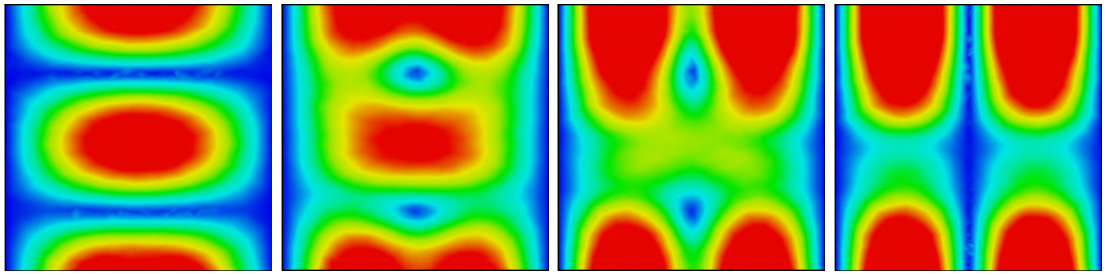

(a) 0° phase shift. (b) 60° phase shift. (c) 120° phase shift. (d) 180° phase shift.

Figure 4.36: The Effect of Feed Phase at 2.635 GHz for the Same Face Model.

4.5.2 Adjacent Faces

Resonant Modes

Again, the four resonant modes were investigated first. At 2.387 GHz, mode TE_{120} is evident. When the phase is shifted, almost no change in hotspot position is observed. The patterns at 0°, 60°, 120° and 180° are almost completely identical, as seen in *Figure* 4.37.

At 2.445 GHz, TE_{303} mode is evident when 0° phase difference is applied, shown in *Figure* 4.38. When the phase shift is altered, the hotspots do not disappear but transform gradually into mode TE_{121}, which is fully evident at 180° phase. This can be seen in *Figure* 4.38. These patterns, being representations of two different characteristic modes, are radically different, making it difficult to track the position of a single hotspot through phase. Rather, nine horizontally spaced, 'column' shaped hotspots transform into two vertically stacked, 'sheet' like hotspots.

At 2.588 GHz, there is a central hotspot in evidence, which changes size very slightly around its central position when the feed phase is changed, with no evidence of meaningful hotspot movement, as shown in *Figure* 4.39. At 2.644, displayed in *Figure* 4.40, the hotspot configurations change completely when the input phase difference is changed. No movement of a single hotspot is evident.

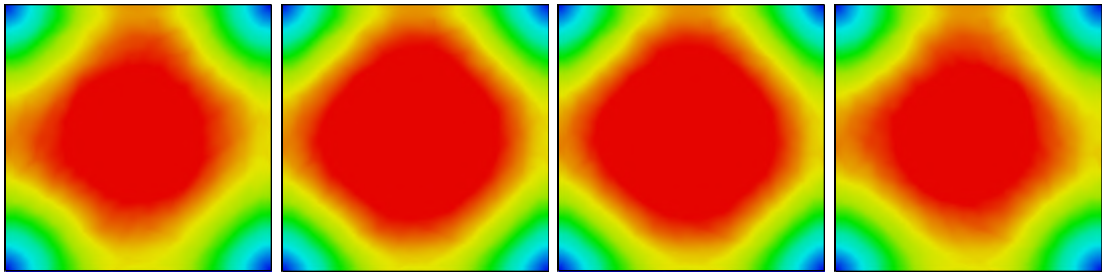

(a) 0° phase shift. (b) 60° phase shift. (c) 120° phase shift. (d) 180° phase shift.

Figure 4.37: The Effect of Feed Phase at 2.387 GHz for the Adjacent Face Model.

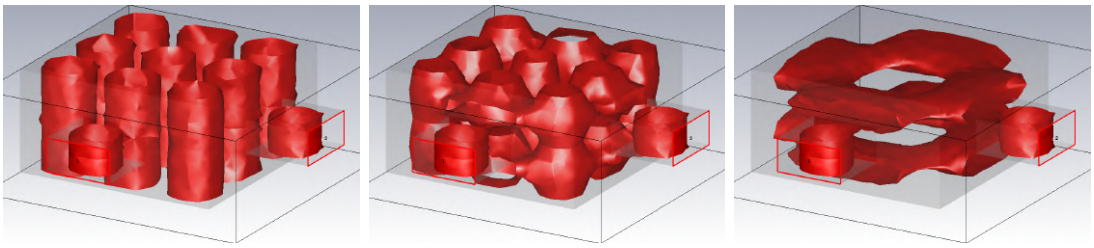

(a) 0° phase shift. (b) 90° phase shift. (c) 180° phase shift.

Figure 4.38: The Effect of Feed Phase at 2.455 GHz for the Adjacent Face Model.

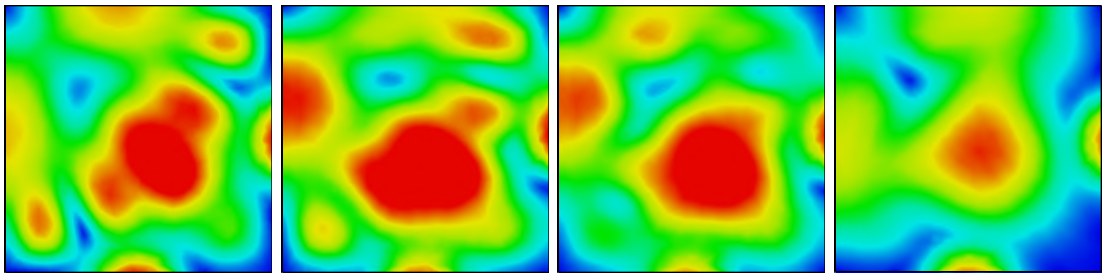

(a) 0° phase shift. (b) 60° phase shift. (c) 120° phase shift. (d) 180° phase shift.

Figure 4.39: The Effect of Feed Phase at 2.588 GHz for the Adjacent Face Model.

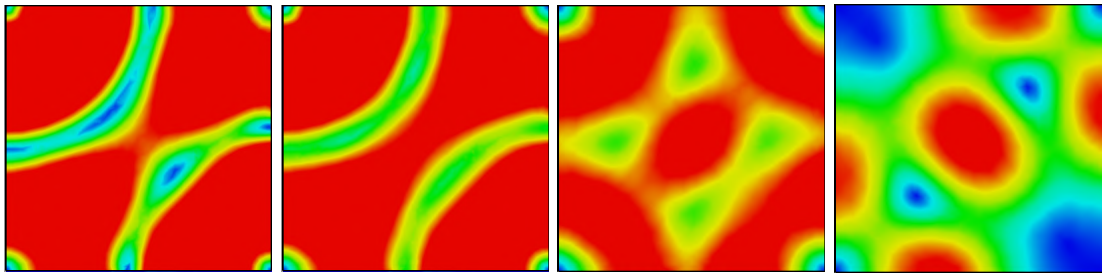

(a) 0° phase shift. (b) 60° phase shift. (c) 120° phase shift. (d) 180° phase shift.

Figure 4.40: The Effect of Feed Phase at 2.644 GHz for the Adjacent Face Model.

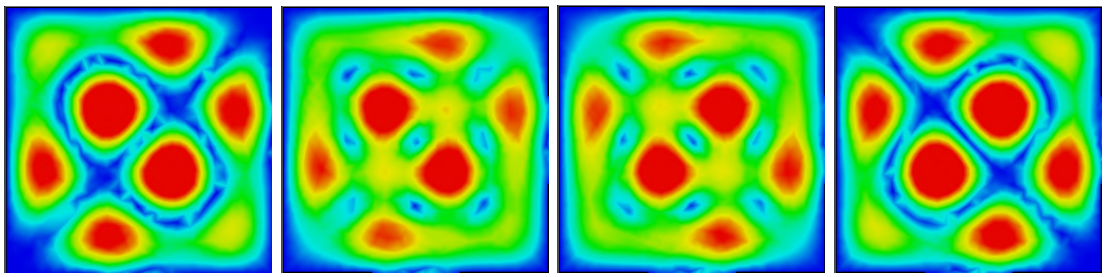

(a) 0° phase shift. (b) 60° phase shift. (c) 120° phase shift. (d) 180° phase shift.

Figure 4.41: The Effect of Feed Phase at 2.385 GHz for the Adjacent Face Model.

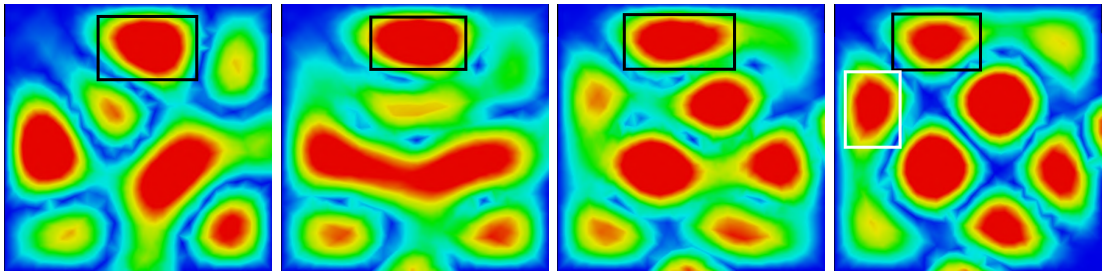

(a) 0° phase shift. (b) 60° phase shift. (c) 120° phase shift. (d) 180° phase shift.

Figure 4.42: The Effect of Feed Phase at 2.421 GHz for the Adjacent Face Model.

Other Frequencies

At 2.385 GHz, the field pattern transitions between two configurations, which are effectively duplicates of the same pattern, oriented perpendicular to each other at 0° and 180° feed phase shift. Looking at the 60° seen in *Figure* 4.41, the perpendicular patterns undergo no hotspot movement before they rotate at 90°.

At 2.421 GHz, the hotspot configuration changes when the phase is altered, as seen in *Figure* 4.42. There is some gradual movement of a hotspot, demarcated by the black box. The hotspot changes position, moving to the left when the phase difference is increased to 180°. However, the hotspot does not keep its shape the entire time and is not a major hotspot. The same movement occurs between 180° and 360° for the hotspot outlined in white, though this progression is not depicted.

At 2.635 GHz, there are two hotspots stacked vertically in the centre of the cavity. These hotspots do not move through phase but change size as the field intensity changes. They are at their maximum at 90° phase shift between the sources and at their minimum at 0° and 180° phase between the sources. As seen in *Figure* 4.43, the contour plane pattern through the cavity is almost identical at 0°, 60°, 120° and 180° phase.

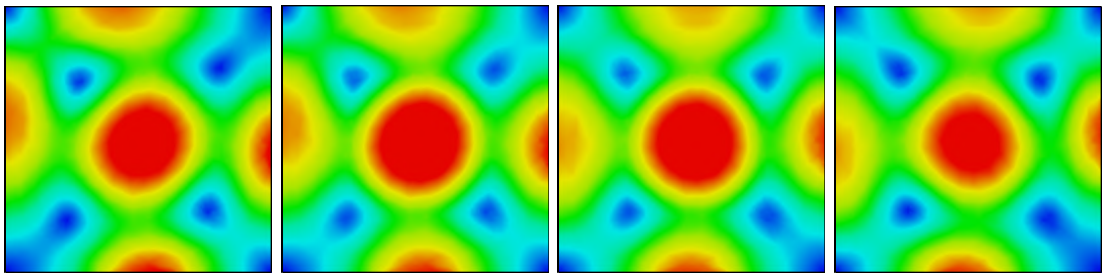

(a) 0° phase shift. (b) 60° phase shift. (c) 120° phase shift. (d) 180° phase shift.

Figure 4.43: The Effect of Feed Phase at 2.635 GHz for the Adjacent Face Model.

4.5.3 Opposite Faces

Resonant Modes

At 2.387 GHz, the characteristic TE_{104} pattern was evident at 180° phase shift between the waveguides, because the sources were facing each other and hence, were in a 180° 'geometric' phase shift to begin with, as seen in *Figure* 4.44. As before, the four hotspots do not move when the phase shift is altered, rather the field intensity decreases, and the hotspots disappear.

At 2.4558 GHz, the columns that represent TE_{303} are apparent at 0° phase difference, shown in *Figure* 4.45. At 180° phase, the columns again disappear owing to the decreased field intensity. In this case, the column closest to the lagging waveguide source disappears faster than the others and the central column does shift slightly towards the leading source as the phase is increased. However, the movement is so slight that the hotspot margins change negligibly before it disappears.

At 2.6535 GHz, TE_{122} is completely evident at 180° phase difference. The pattern hardly changes at all, and the field intensity decreases drastically away from the resonant peak when the phase shift starts deviating from 180°, as shown in *Figure* 4.46. No hotspot movement is evident.

The simulation at 2.588 GHz was the first simulation to exhibit meaningful hotspot movement depending on the introduced phase difference between the sources. Between 90° and 270° phase difference, there is a clear linear movement of the central hotspot towards the leading waveguide. *Figure* 4.47 shows the progression of the central hotspot over the 180° interval. In this case, the pattern itself is largely resilient. The shape of the hotspot does not change much, nor does the field intensity. The position of the hotspot is the key variable that changes. This was the type of hotspot progressive movement that was sought after in this investigation.

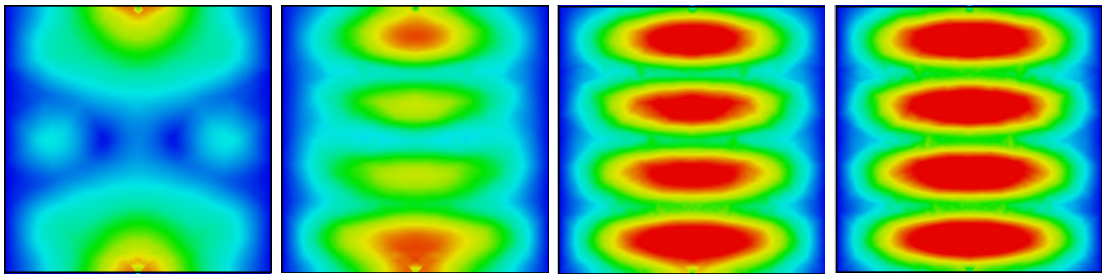

(a) 0° phase shift. (b) 60° phase shift. (c) 120° phase shift. (d) 180° phase shift.

Figure 4.44: The Effect of Feed Phase at 2.387 GHz for the Opposite Face Model.

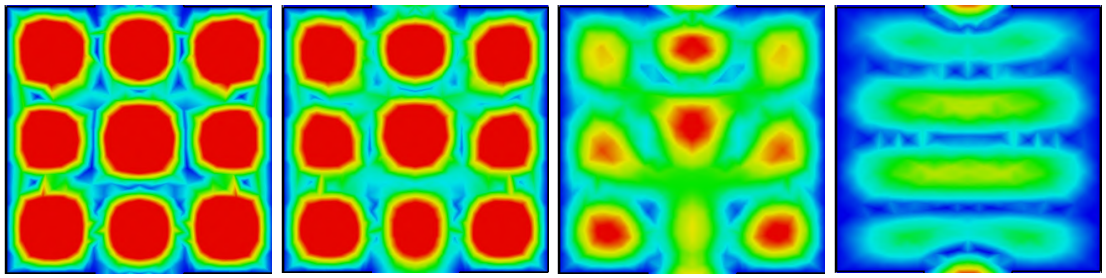

(a) 0° phase shift. (b) 60° phase shift. (c) 120° phase shift. (d) 180° phase shift.

Figure 4.45: The Effect of Feed Phase at 2.4558 GHz for the Opposite Face Model.

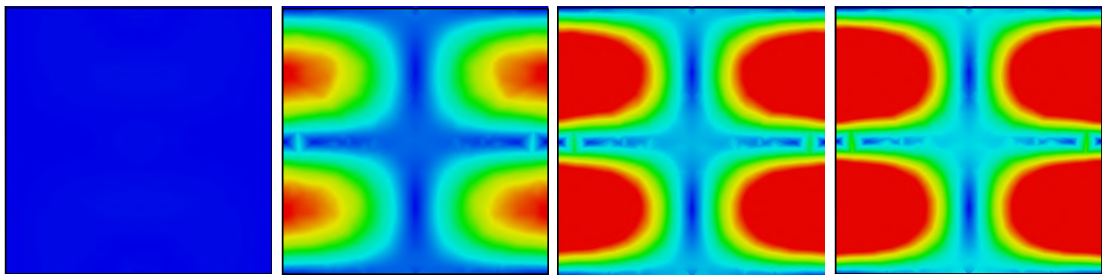

(a) 0° phase shift. (b) 60° phase shift. (c) 120° phase shift. (d) 180° phase shift.

Figure 4.46: The Effect of Feed Phase at 2.6535 GHz for the Opposite Face Model.

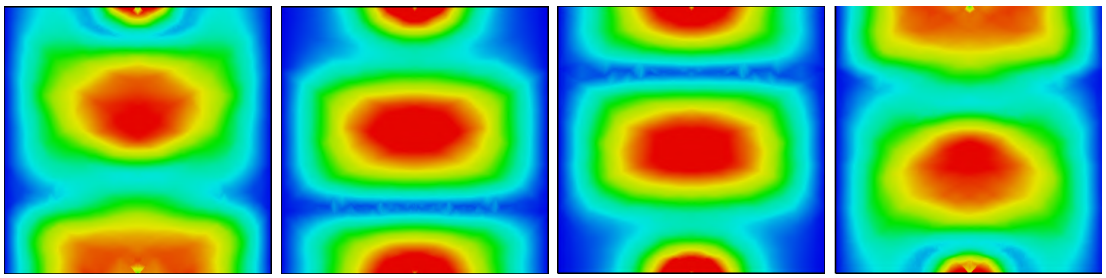

(a) 90° phase shift. (b) 150° phase shift. (c) 210° phase shift. (d) 270° phase shift.

Figure 4.47: The Effect of Feed Phase at 2.588 GHz for the Opposite Face Model.

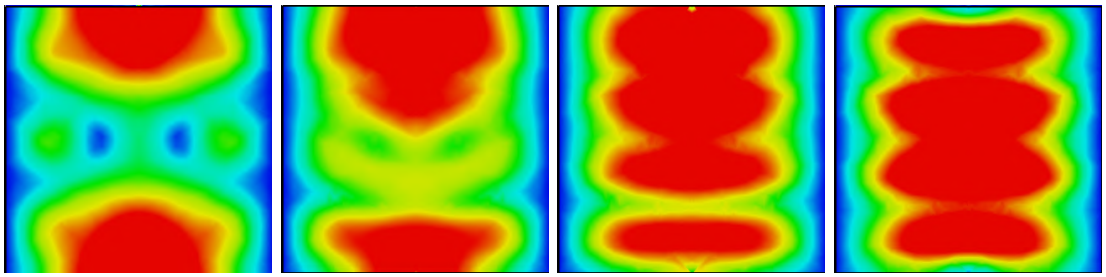

(a) 0° phase shift. (b) 60° phase shift. (c) 120° phase shift. (d) 180° phase shift.

Figure 4.48: The Effect of Feed Phase at 2.421 GHz for the Opposite Face Model.

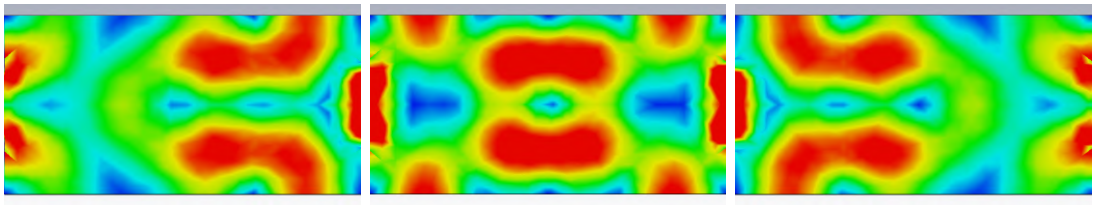

(a) 90° phase shift. (b) 60° phase shift. (c) 120° phase shift.

Figure 4.49: The Effect of Feed Phase at 2.499 GHz for the Opposite Face Model.

Other Frequencies

At 2.421 GHz, there appear to be set hotspot locations within the cavity, with different loci becoming accentuated depending on the feed phase shift. At 0° and 180°, the configuration is quite symmetrical and for the phase shift iterations in between, the hotspots nearest the leading waveguide are more accentuated. There is no obvious hotspot movement, as seen in *Figure* 4.48.

At 2.499, there appears to be a combination of hotspot movement and orientation shift and the change in hotspot orientation seen in *Figure* 4.48. This pattern can be seen in *Figure* 4.49.

At 2.635 GHz, there is clear hotspot movement, like that exhibited at 2.588 GHz, again between 90° and 180°. This is shown in *Figure* 4.50. Upon further investigation, it was determined that this pattern of hotspot movement was evident for the frequencies between 2.55 GHz and 2.7 GHz, the upper limit of the frequency in the sweep, apart from the resonant peak at 2.6535 GHz. In all cases, the hotspot moved straight from the lagging source to the leading source. However, for all other circumstances, hotspot movement was not possible if the phase difference between the sources was the only altered variable.

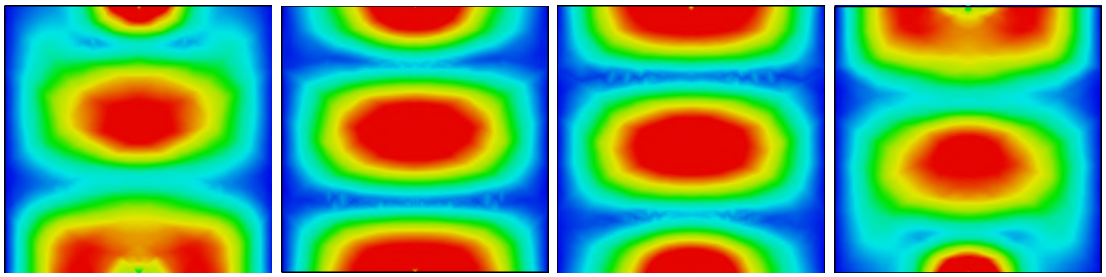

(a) 90° phase shift. (b) 150° phase shift. (c) 210° phase shift. (d) 270° phase shift.

Figure 4.50: The Effect of Feed Phase at 2.635 GHz for the Opposite Face Model.

4.6 Conclusion

This chapter presented the results of the investigation outline in Chapter 3, the Methodology. The testing of the software packages, the verification of the simulation model, the characterisation of the resonant cavity and the manipulation of the hotspot positions within the cavity were discussed.

It was concluded that the software packages CST Studio Suite Student Edition and Altair's FEKO, even though they use different solver methods, yielded the same solution to a simulation problem. SuperNEC was abandoned because of its inability to utilise a waveguide port as a source and for the difficulty in changing the geometry of the model.

FEKO was used to verify the simulation platform by simulating the electric near fields inside a microwave oven and comparing them to the measured field. This was accomplished successfully, and it was concluded that FEKO was a suitable simulation platform and yielded results that were comparable to real-world situations for electromagnetic resonance.

A test model of a rectangular resonant cavity was created in CST and FEKO and characterised to determine the ideal frequency band of operation and the characteristic resonant modes. 4 modes were identified. The frequency of the feed to the cavity was swept to examine hotspot movement through frequency. It was observed that in the range of 2.6–2.7 GHz, progressive hotspot movement occurred. However, for most of the frequency range, the near field pattern morphed between its resonant modes without much linear hotspot movement.

An examination of the effect of introducing a phase difference between two waveguide ports was conducted to observe any hotspot movement. It was found for the instances of waveguides being orientated on the same face, and for waveguides positioned on adjacent faces, phase shifting did not cause any hotspots to move as desired. It was observed, however, when the waveguides were orientated on opposite faces, that for frequencies

above 2.55 GHz, the feed phase did influence the position of the major hotspots in the sense that a progressive introduction of phase shift resulted in the progressive movement of the hotspots in question. This was only evident for the model containing waveguides on opposite faces and did not hold at the resonant peak within the band.

Additionally, it was determined that the behaviour of the resonant cavity is very sensitive to dielectric influence, and the resonant characteristics are different depending on the body of dielectric inside the chamber.

Chapter 5

Conclusion

5.1 Summary

This investigation pertained to the feasibility of controlling the position of electromagnetic hotspots at microwave frequencies within a resonant cavity for applications in clinical thermal ablation.

The methodology focused on a simulation-based solution and was subdivided into 4 sections:

- The software testing section, where the simulation platforms, CST Studio, FEKO and SuperNEC were compared against each other for their solution to a benchmark model.
- The verification section, where the software was tested against a real-world resonant cavity, a microwave oven, for realistic accuracy.
- The characterisation of an ideal resonant cavity model, where the resonant properties of a simple rectangular chamber were investigated, along with the influence of dielectric absorbing bodies.
- The field manipulation section, where additional sources were introduced to the model and the effects of frequency sweeping and the introduction of a phase difference between the sources upon hotspot position.

It was concluded that CST Studio and FEKO yield the same results through simulation, which were verified when compared to the near field pattern evident inside the microwave oven. After characterisation of the resonant cavity, it was concluded that for a specific frequency range, 2.6–2.7 GHz, incremental changes in feed frequency caused a similar

incremental shift in the position of the main hotspots of the system. For the phase shifting investigation, it was concluded that only in the frequency band of 2.55–2.7 GHz, for the model containing two waveguide sources on opposite faces, was progressive hotspot movement evident, and only when the feed phase difference was situated between 90° and 270°.

5.2 Research Questions

This section discusses the results of the investigation as they pertain to the answering of the research question.

"Can the position of an electromagnetic hotspot at microwave frequencies be controlled consistently and feasibly within a resonant cavity?"

The research question was broken down into 4 sub-questions which are answered individually as follows:

- Can a microwave frequency electromagnetic hotspot be effectively modelled in a resonant cavity?

Yes. It was determined at the beginning of the investigation that the electric near field within a bounded resonant cavity could be effectively simulated using a variety of solver techniques. In all instances, the simulation results yielded areas in the three-dimensional interior of the cavity which exhibited high electric field intensity and low electric field intensity, as is characteristic of the electromagnetic near field. These pockets of high electric field intensity were evaluated as the system's hotspots.

- Can the resonance and field pattern of the model be changed by adding another microwave source?

Yes. As seen in *Chapter* 4, the field pattern inherent in the chamber at a specific single frequency was different depending on the orientation of the two waveguides in relation to each other. However, the pattern evident at the resonant peaks remains by and large similar, possibly indicating that when the cavity is excited with the natural resonant frequency of the system, the orientation of the waveguides or even the number of waveguides does not influence the near field pattern.

- Can altering the phase and frequency of each source change the electromagnetic field pattern within the resonant cavity and hence, change the hotspot positions?

Yes. Given that the near field is inherently dependant on the excitation frequency, shifting the frequency does change the near field pattern. In many cases, however, this

does not result in a progressive change in hotspot position, but rather a morphing of the near field pattern. This included changing the size, shape and number of hotspots instead of simply the position of the existing hotspots. Only for a relatively narrow range of frequencies was progressive hotspot movement evident.

For the phase shifting investigation, it was discovered in most cases that altering the phase difference between two sources had no effect on the near field pattern at all, so no hotspot alteration of any kind was evident. Only in the case of opposing waveguides was the near field influenced by the addition of a phase difference. Then, for most tests thereafter, it was further determined that, like with the frequency shifting, the hotspots were morphed instead of moved. Again, only for a specific frequency band was progressive hotspot movement evident. Thus, on the question of whether the system's hotspots could be moved progressively, the answer in the technical sense is yes, however, only under specific circumstances.

- Is the change of hotspot position consistent and feasible for the application of clinical microwave thermal ablation?

No. As discussed previously, the movement of the hotspots through frequency and phase difference is not consistent and relies upon specific circumstances. Additionally, it was determined that the addition of dielectric material in the chamber had a great effect on the resonance of the system. All investigations into the movement of hotspots were conducted in free space, lacking any absorbing bodies. With the addition of dielectric, energy absorption takes place, altering the behaviour of the field, changing the resonant frequencies of the system. The cause of concern here is that all patients are different and will exhibit different dielectric properties.

If the necessary parameters to achieve hotspot movement with the presence of a specific body of dielectric were determined, the modification of the properties of the dielectric body, for instance, a different patient, might change the natural resonance of the system sufficiently that a completely new set of parameters, feed frequency, waveguide orientation etc., would need to be implemented to achieve progressive hotspot movement. Therefore, even though the movement of a set of hotspots in a resonant cavity is theoretically possible, it is infeasible for the highly precise field application of thermal ablation.

5.3 Future Recommendations

Several additional avenues can be explored regarding this research. Firstly, this investigation centred around the use of a standard rectangular resonant cavity with a

rectangular waveguide feed at frequencies centred around 2.45 GHz, as this is the basis for microwave oven heating. Therefore, the eigenfrequencies of the cavity were calculated and the hotspots of the system at different frequencies were discovered through simulation. Further research into the geometric shape of the resonant cavity and the feed mechanism can be undertaken to focus more on the design of a system that would result in a specific hotspot location or pattern. Therefore, the desired hotspot pattern could be designed for.

Additionally, the parameters that were altered in this investigation to attempt to move the hotspots were feed frequency and phase difference between sources, like an antenna array. An extra avenue could be modulating the physical geometry of the system like the metallic stirrer approach to the early microwave ovens. For example, the angle of one of the walls, or the length of the cavity. The addition of a modular wall or set of walls could be a worthwhile avenue to investigate.

The use of more directive sources could be investigated. The waveguide source is very useful at launching a plane wave directly into the resonance cavity. Further research into the use of a directive antenna within a resonant cavity could be conducted.

The final future recommendation is to consider the 'reverse problem'. Considering that the current method of microwave thermal ablation uses an interstitial antenna to create a hotspot over the tumour, the question becomes how to create the same hotspot without the antenna. Consider a bounded metallic surface surrounding the patient and the antenna. When the antenna is fed, electromagnetic radiation radiates from it and induces a current distribution on the surrounding metallic surface. If that same current distribution could be induced on the surface externally, according to three-dimensional Green's Theorem, the same hotspot could be created without the need for the antenna at all. An investigation into the feasibility of this could be conducted.

5.4 Conclusion

The investigation presented in this dissertation aimed to determine whether the position of electromagnetic hotspots inside a resonant cavity could be consistently controlled using feed frequency and phase and whether such a method was feasible for the thermal ablation of tumours. It was concluded that while theoretically, the hotspot positions could be controlled under certain circumstances, this approach, as outlined in the investigation, was not feasible for use in high precision and unique applications like microwave thermal ablation.

References

[1] C. Brace, "Thermal tumor ablation in clinical use," *IEEE Pulse*, vol. 2, pp. 28–38, Sep. 2011.

[2] L. S. Poulou, E. Botsa, I. Thanou, P. D. Ziakas, and L. Thanos, "Percutaneous microwave ablation vs radiofrequency ablation in the treatment of hepatocellular carcinoma.," *World journal of hepatology*, vol. 7, pp. 1054–63, May 2015.

[3] E. Maloney and J. H. Hwang, "Emerging hifu applications in cancer therapy," *International Journal of Hyperthermia*, vol. 31, no. 3, pp. 302–309, 2015.

[4] N. T. Wright, "Quantitative models of thermal damage to cells and tissues," in *Heat Transfer and Fluid Flow in Biological Processes* (S. M. Becker and A. V. Kuznetsov, eds.), ch. 3, pp. 59 – 76, Boston: Academic Press, 2015.

[5] D. S. Lu, S. S. Raman, P. Limanond, D. Aziz, J. Economou, R. Busuttil, and J. Sayre, "Influence of large peritumoral vessels on outcome of radiofrequency ablation of liver tumors," *Journal of Vascular and Interventional Radiology*, vol. 14, no. 10, pp. 1267–1274, 2003.

[6] D. Dupuy and M. Shulman, "Current status of thermal ablation treatments for lung malignancies," *Seminars in interventional radiology*, vol. 27, pp. 268–75, 09 2010.

[7] B. D. Horbaniuc, "Refrigeration and air-conditioning," in *Encyclopedia of Energy* (C. J. Cleveland, ed.), pp. 261–289, New York: Elsevier, 2004.

[8] E. Schena, P. Saccomandi, and Y. Fong, "Laser ablation for cancer: Past, present and future," *Journal of Functional Biomaterials*, vol. 8, no. 2, 2017.

[9] A. R. Clark, *A Study Guide forElectromagnetics.* Poynting Innovations (Pty) Ltd, 1.0 ed., 2004.

[10] S. W. Ellingson, *Electromagnetics, Volume 1*, vol. 1, ch. 1, pp. 1–17. VT Publishing, 2018.

[11] P. A. Mello, J. S. Barin, and R. A. Guarnieri, "Microwave heating," in

Microwave-Assisted Sample Preparation for Trace Element Analysis (Érico Marlon de Moraes Flores, ed.), ch. 2, pp. 59 – 75, Amsterdam: Elsevier, 2014.

[12] S. Z. Li and A. Jain, "Electromagnetic radiation," in *Encyclopedia of Biometrics*, pp. 254–254, Boston, MA: Springer US, 2009.

[13] J. John W. Jewett and R. A. Serway, *Electromagnetic Waves*, ch. 34, pp. 952–968. 10 Davis Drive, Belmont, CA: David Harris, 7th ed., 2008.

[14] A. R. Clark and A. P. C. Fourie, *Antennas in Practice*. Poynting Innovations (Pty) Ltd, 1.4 ed., 2002.

[15] C. A. Balanis, *Antenna Theory, Analysis and Design*, ch. 2, pp. 25–127. John Wiley & Sons, Inc., 4 ed., 2016.

[16] S. M. Mikki and Y. M. M. Antar, "A theory of antenna electromagnetic near field—part i," *IEEE Transactions on Antennas and Propagation*, vol. 59, pp. 4691–4705, Dec 2011.

[17] J. D. Kraus, *Antennas*, ch. 2, pp. 17–86. Tata McGraw-HUI Publishing Company Limited, 2 ed., 1988.

[18] Wikipedia, "Far and near fields." `https://commons.wikimedia.org/wiki/File:FarNearFields-USP-4998112-1.svg`. [Online] Accessed: 2021-06-30.

[19] H. Esfahlani, S. Karkar, and H. Lissek, "Acoustic metasurface," in *6th International Conference on Metamaterials, Photonic Crystals and Plasmonics*, 08 2015.

[20] C. A. Balanis, *Antenna Theory, Analysis and Design*, ch. 6, pp. 285–385. John Wiley & Sons, Inc., 4 ed., 2016.

[21] L. P. Kollár and G. Tarján, "Basics of vibration," in *Mechanics of Civil Engineering Structures* (L. P. Kollár and G. Tarján, eds.), Woodhead Publishing Series in Civil and Structural Engineering, ch. 8, pp. 299–343, Woodhead Publishing, 2021.

[22] S. Z. Li and A. Jain, "Electromagnetic resonance," in *Encyclopedia of Biometrics*, pp. 254–254, Boston, MA: Springer US, 2009.

[23] M. Mehdizadeh, "Chapter 2 - fundamentals of field applicators and probes at radiofrequencies and microwave frequencies," in *Microwave/RF Applicators and Probes (Second Edition)* (M. Mehdizadeh, ed.), pp. 34–67, Boston: William Andrew Publishing, second edition ed., 2015.

[24] J. Tang and F. Resurreccion, "Electromagnetic basis of microwave heating," in

Development of Packaging and Products for Use in Microwave Ovens (M. W. Lorence and P. S. Pesheck, eds.), ch. 1, pp. 3 – 38e, Woodhead Publishing, 2009.

[25] G. Shimonov, A. Koren, G. Sivek, and E. Socher, "Electromagnetic property characterization of biological tissues at d-band," *IEEE Transactions on Terahertz Science and Technology*, vol. 8, pp. 155–160, March 2018.

[26] H. Zhang and A. K. Datta, "Coupled electromagnetic and termal modeling of microwave oven heating of foods," *Journal of Microwave Power and Electromagnetic Energy*, vol. 35, no. 2, pp. 71–85, 2000.

[27] L. Campañone, C. Paola, and R. Mascheroni, "Modeling and simulation of microwave heating of foods under different process schedules," *Food and Bioprocess Technology*, vol. 5, pp. 738–749, 01 2011.

[28] K. Pitchai, "Electromagnetic and heat transfer modeling of microwaveheating in domestic ovens," Master's thesis, University of Nebraska at Lincoln, 2011.

[29] C. J. Coleman, "On the microwave hotspot problem," *The Journal of the Australian Mathematical Society. Series B. Applied Mathematics*, vol. 33, no. 1, p. 1–8, 1991.

[30] P. G. Huray, "Time varying fields," in *Maxwell's Equations*, ch. 7, pp. 203–246, IEEE, 2010.

[31] W. C. Gibson, "The method of moments," in *The Method of Moments in Electromagnetics*, ch. 3, pp. 33–62, CRC Press, 1 ed., 2008.

[32] B. C. Archambeault B., Ramahi O.M., "Method of moments," in *EMI/EMC Computational Modeling Handbook*, ch. 4, pp. 69–82, Springer, 1998.

[33] W. C. Gibson, "Integration," in *The Method of Moments in Electromagnetics*, ch. 9, pp. 255–270, CRC Press, 1 ed., 2008.

[34] W. C. Gibson, "The fast multipole method," in *The Method of Moments in Electromagnetics*, ch. 8, pp. 209–254, CRC Press, 1 ed., 2008.

[35] M. Sadiku, "A simple introduction to finite element analysis of electromagnetic problems," *IEEE Transactions on Education*, vol. 32, pp. 85–93, May 1989.

[36] B. C. Archambeault B., Ramahi O.M., "The finite element method," in *EMI/EMC Computational Modeling Handbook*, ch. 5, pp. 83–104, Springer, 1998.

[37] B. C. Archambeault B., Ramahi O.M., "The finite-difference time-domain method," in *EMI/EMC Computational Modeling Handbook*, ch. 3, pp. 35–67, Springer, 1998.

[38] Z. Rahimi, *The Finite Integration Technique (FIT) and the Application in Lithography Simulations*. PhD thesis, University of Erlangen-Nuremberg, 06 2011.

[39] J. Petráček and J. Luksch, "Bidirectional eigenmode propagation algorithm for 3d waveguide structures," in *2011 13th International Conference on Transparent Optical Networks*, pp. 1–4, June 2011.

[40] Dassault Systèmes SE, *CST Studio Suite 2020 Manual*, 2020.

[41] Altair, "Altair feko." https://www.altair.com/feko/. [Online] Accessed: 2021-04-30.

[42] Altair, *Altair FEKO 2021.0.3 User Guide*, 2021.

[43] "Cst studio suite - free electromagnetic simulation software." https://www.3ds.com/products-services/simulia/products/cst-studio-suite/student-edition/. [Online] Accessed: 2021-04-30.

[44] EMWorks, "Hfworks - antenna and electromagnetic simulation software." https://www.emworks.com/product/hfworks. [Online] Accessed: 2021-07-01.

[45] G. J. Burke, A. J. Poggio, J. C. Logan, and J. W. Rockway, "Numerical electromagnetic code (nec)," in *1979 IEEE International Symposium on Electromagnetic Compatibility*, pp. 1–3, Oct 1979.

[46] D. Nitch, *SuperNEC: MOM-UTD Hybrid User Reference Manual*. Poynting Software (Pty) Ltd.

[47] MathWorks, "Matlab." https://www.mathworks.com/products/matlab.html. [Online] Accessed: 2021-05-04.

[48] Autodesk, "Inventor." https://www.autodesk.co.za/products/inventor/overview. [Online] Accessed: 2021-06-30.

[49] M. Soltysiak, M. Celuch, and U. Erle, "Measured and simulated frequency spectra of the household microwave oven," in *2011 IEEE MTT-S International Microwave Symposium*, pp. 1–4, June 2011.

[50] everythingRF, "Wr340 — wg9a — r26 - rectangular waveguide size." https://www.everythingrf.com/tech-resources/waveguides-sizes/wr340. [Online] Accessed: 2021-05-24.

[51] D. M. Pozar, *Microwave Engineering*, ch. 3, pp. 110–119. John Wiley & Sons, Inc., 4 ed., 2012.

[52] D. M. Pozar, *Microwave Engineering*, ch. 6, pp. 284–287. John Wiley & Sons, Inc., 4 ed., 2012.

[53] T. Williams, "Shielding," in *EMC for Product Designers (Fifth Edition)* (T. Williams, ed.), ch. 15, pp. 435–457, Newnes, fifth edition ed., 2017.

[54] D. W. P. Thomas, A. Denton, T. Konefal, T. M. Benson, C. Christopoulos, J. F. Dawson, A. C. Marvin, and J. Porter, "Characterisation of the shielding effectiveness of loaded equipment enclosures," in *International Conference and Exhibition on Electromagnetic Compatibility, 1999. EMC York 99. (Conf. Publ. No. 464)*, pp. 89–94, July 1999.

[55] M. Bingle, E. Burger, U. Jakobus, and J. J. van Tonder, "Theory and application of an mlfmm/fem hybrid framework in feko," in *2011 IEEE International Conference on Microwaves, Communications, Antennas and Electronic Systems (COMCAS 2011)*, pp. 1–3, Nov 2011.

[56] COMSOL, "Perfect electric conductor." `https://doc.comsol.com/5.5/doc/com.comsol.help.rf/rf_ug_radio_frequency.07.11.html`. [Online] Accessed: 2021-04-29.

[57] T. Williams, "Emc," in *Instrumentation Reference Book (Fourth Edition)* (W. Boyes, ed.), ch. 45, pp. 797–871, Boston: Butterworth-Heinemann, fourth edition ed., 2010.

Appendix A

NEC2 Hotspot Plotter

A.1 Introduction

This appendix presents the workings of a MATLAB based application for plotting the 3D iso-surface data of electromagnetic near field simulations in NEC2. The program uses data stored in a generic NEC2 output file, meaning it can be used in conjunction with any NEC2 simulator. This program was used to plot the internal hotspots of a resonant cavity in the initial stages of the investigation, to establish a benchmark simulation of the NEC2 solver. A brief background of NEC2 will be discussed in *Section A.2* and the parameters of the program will be discussed at follows: how the app works in *Section A.3*, the interface in *Section A.4*, the input and output profiles in *Section A.5* and the shortcomings and future recommendations in *Section A.6*.

A.2 NEC2

NEC2, or Numerical Electromagnetic Code 2 is an electromagnetic modelling system for wireframe antennas. It uses the method of moments solver [1]. NEC2 is an updated version of NEC, which was developed in the 1970's. It is the most commonly used version of NEC in the public domain that does not require a license. The NEC engine essentially uses text files as its input and output. It requires a '.nec' file as an input, which is a text file containing the geometry of the structure, important information such as frequency and excitation and the requested outputs. The engine outputs another text file, a '.out' file, which contains all relevant input data as well as the simulated requests.

A.3 Working

The application is divided into two sections, the loading of a NEC file and the plotting of the near field data. It uses one of the functions native to SuperNEC, *snres*, to extract relevant data from a NEC file. *snres* Effectively allows the user to load an output NEC file and extract usable data, such as structure data, near field data, far field data, frequency etc. Upon opening a file, *snres* extracts to the NEC data from it and the model is loaded into the application. When a plot of the data is requested, the near field data is loaded from the model into a 4-dimensional array, containing x, y and z coordinates and the corresponding near field data which is further divided into the x, y and z components of both the magnitude and phase of the field at that point. Since only the magnitude was needed, this data alone was combined into a total near field contribution. Thereafter, MATLAB's *isosurface* [2] function was used to plot the data as a 3-dimension surface. This function computes geometry data based around an *isovalue*, or threshold. It effectively connects all the data points matching the *isovalue* in the input data set and maps it to a geometric representation. It also uses an interpolation function so there are no gaps in the mapped surface if the discreet dataset does not contain an exact match to the *isovalue*. The *isovalue* itself is user controlled. The value can either be set as a value in V/m, or as a precentage of max. In either case, the opposite parameter is displayed, so if a percentage is set, the program will also output what value this represents, and vice versa. The structure of the NEC file is also loaded, so the wireframe can be displayed. The user can then elect to plot the structure or not, or plot the structure with a set transparency. The plot window is then updated, and the isosurface geometry of the set *isovalue* is plotted on a set of 3D axes, along with the wire structure with the desired transparency. The plot window can be updated at will to display different values or models. The plot window is also subject to all standard MATLAB plot functions, such as to save as an image, copy as a vector graphic, return view to home, pan, rotate and zoom.

A.4 Interface

The interface of the application was designed in MATLAB 2020, using the native app designer. *Figure A.1* shows the user interface of the application. As shown, there is a model tree on the left, which can show the models that have been loaded. There are two push buttons for loading a model and plotting the data, along with a tick box for plotting the structure. A slider that controls the opacity of the structure and a numerical input box where the threshold value can be set. The main area of the interface is taken up by the plot area. In this case of *Figure A.1*, the model's name was 'benchmark.out',

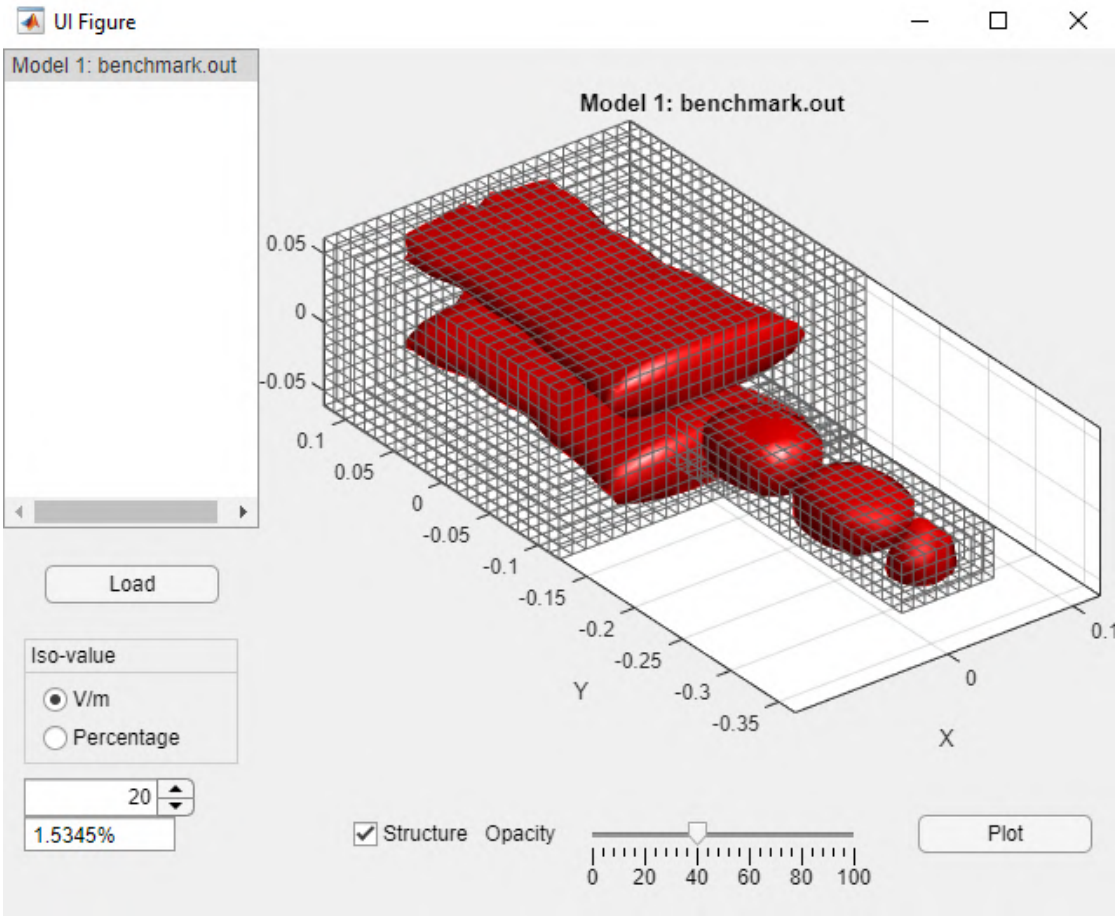

Figure A.1: Application Interface with Loaded Model and Plotted Data.

the *isovalue* set to 20 V/m and the structure plotted with 40% opacity.

A.5 I/O

The application was designed to accept any NEC2 output file as an input. A NEC2 output file is essentially a text file with an '.out' file extension that contains all the information about the NEC simulation. This includes the model geometry in terms of the start and end coordinates of every segment used, all requests and frequencies used, wire junctions, segmentation data, plate data, cylinder data, structural impedance, environment information, input parameters, wire current and charges and all other requests, such as near field data, far fields, etc. All electromagnetic data is stored in magnitude and phase pairs for each component, x, y and z. The file includes different formatting for much of the data and various text headings and white spaces, hence, the *snres* function is used to extract the data from the file. Note that the application only works if a single frequency was simulated, and only with near field data. The program uses the data to

output a visual representation of the near field of the simulation, or the 'hotspots' of the system, as shown in *Figure A.1*. It is also possible to access the organised NEC data extracted by *snres* directly from the MATLAB command window while the application is running, for other applications of the data.

A.6 Future Recommendations

The biggest addition to the application would be the ability to load a file which has multiple frequencies and plot the data of any simulated frequency. Currently, the application runs into errors if the file contains more than a single frequency. This functionality was not developed as it was not necessary in the initial benchmark simulations of the investigation. Additionally, it would be useful to be able to plot a specific component of the near field in isolation, instead of only the total field. Thirdly, a phase plotter in addition to the magnitude would be useful for certain applications, along with the magnitude and phase of the magnetic near field. Lastly, extra error checks should be implemented so that if a common error would occur, a message about the problem is displayed to the user, who can then amend the issue, instead of a MATLAB error pausing the program.

A.7 Conclusion

An introduction to the MATLAB based program created to plot the 3D hotspots of a resonant cavity has been presented. The application's working and interface were discussed, along with future recommendations to improve upon its capability. The application formed an important role in the initial investigation of comparing NEC2 solvers against other electromagnetic solver software.

References

[1] G. J. Burke, A. J. Poggio, J. C. Logan, and J. W. Rockway, "Numerical electromagnetic code (nec)," in *1979 IEEE International Symposium on Electromagnetic Compatibility*, pp. 1–3, Oct 1979.

[2] MathWorks, "isosurface." `https://www.mathworks.com/help/matlab/ref/isosurface.html`. [Online] Accessed: 2021-06-24.

Appendix B

Comparison of Electromagnetic Field Solvers

B.1 Introduction

This appendix focuses on the simulation of resonant near field problems within the computational electromagnetic programs, CST Studio Suite and FEKO by Altair. Specific emphasis is given to the solver methods available, a comparison of the outputs from the various solver methods and the simulation times for each solution. The problem in question is an electric near field problem involving the resonance within a rectangular resonant cavity. The following aspects of the investigation will be discussed: the capabilities of each program considering the available license in *Section B.2*, an overview of the applicable solver methods in *Section B.3*, an overview of the computer specifications used for simulation in *Section B.4*, the parameters of the model to be solved in *Section B.5*, the metrics used for the comparison in *Section B.6*, a comparison of the outputs of each simulation in *Section B.7*, and the simulation time of each solution in *Section B.8*.

B.2 Licences and Capability

The University of the Witwatersrand, Johannesburg, has access to a full FEKO license, so the full functionality of FEKO could be utilised. FEKO has many applications and uses many different solver methods for these applications. It has the capability to use frequency domain, time domain and asymptotic solvers and makes resonant cavity simulations easier by the inclusion of the waveguide port feed method, which launches a plane wave of the appropriate frequency straight down the waveguide.

FEKO can stand alone as its own software, requiring no additional programs for the computer aided design (CAD) process or for solving and optimising simulations. However, it can import models and mesh structures from other CAD programs and export solutions in various formats. Additionally, FEKO has the ability to solve each process in parallel, depending on the number of central processing unit (CPU) cores the computer possesses. If the computer makes use of a graphics processing unit (GPU), it offers GPU Acceleration instead of parallel CPU processing.

No University license was available for CST Studio Suite, however, Dassault Systèmes, the company which owns CST, does provide a free student version of the software with various limitations. The full version of CST Studio Suite has nine different solvers: the Asymptotic, Eigenmode, Filter Designer 2D, Filter Designer 3D, Frequency Domain, Integral Equation, Multilayer, Time Domain and Hybrid Solver Task solvers. However in the student version, only the Frequency Domain and Time Domain solvers are available. There is also a limitation on the size of the structure's mesh, and importing and exporting is restricted.

B.3 Solver Methods

The scope of the problem was an electric near field problem for a resonant cavity with a waveguide feed. FEKO and CST Studio Suite Student can both handle this problem using a variety of methods. In FEKO, the frequency and time domain techniques are relevant and include a method of moments (MoM), finite element method (FEM), multilevel fast multipole method (MLFMM) and finite difference time domain (FDTD) solvers. Of these, only the MoM and MLFMM solvers could be used for the particular problem, as the FDTD solver does not support the use of a waveguide port for a feed mechanism, and the FEM solver can only be used to solve dielectric problems, not a perfect electric conductor (PEC) structure in free space.

CST Studio Suite Student Edition includes only the Frequency Domain and Time Domain solvers. The frequency domain solver is based in FEM, and the time domain solver utilises the finite integration technique (FIT) solver, which is similar to FDTD, and a transmission line matrix (TLM) solver, which was not considered. Therefore, between the two programs, an array of solvers were available: MoM, MLFMM, FEM and FIT. Note that MLFMM is not a different solver method to MoM, it is simply a mechanism for speeding up simulation times.

B.4 Computer Properties

This section discusses the specifications of the computer used to run the simulations. The computer's CPU, motherboard, random access memory (RAM), GPU, hard drive and operating system are discussed. The computer was constructed instead of purchased as a unit in 2013, and has undergone various upgrades.

CPU

The computer's processor is an Intel product: the Intel(R) Core(TM) i7-4770 CPU. It is a 4th generation i7 processor. It has 1 socket, 4 cores, 8 threads, and operates at a base frequency of 3.40 GHz, with a max frequency of 3.90 GHz. Additionally, it has an 8 MB cache.

Motherboard

The computer's motherboard is the B85M-G by ASUSTeK Computer Inc. It operates ideally with the CPU and has a stable BIOS.

RAM

The computer's motherboard is only compatible with DDR3 RAM and has 4 slots. All slots are filled with 8 GB sticks of RAM, resulting in 32 GB of DDR3 RAM. All memory operates at 1600 MHz.

GPU

The GPU in the computer is the NVIDIA GeForce GTX 750. It has 512 CUDA cores, a base frequency of 1020 MHz, and a boost frequency of 1085 MHz. In terms of memory, it has 1024 MB of GDDR5 memory with an interface width of 128 bit and a memory clock of 5 Gbps.

Hard Drive

The computer has 2 hard drives, a solid state drive (SSD), which is used as the system disk, and a hard disk drive (HDD), which is used for file storage. The SSD has a capacity of 466 GB and the HDD has a capacity of 932 GB. The operating system and all programs are installed on the SSD. All documents and files are stored on the HDD.

Operating System

The computer operates Windows 10 Pro. The latest version of windows used for this investigation was 21H1, with a build number of 19043.1110. However, the computer has virtualisation enabled and runs an Ubuntu LTS 20.04 command line interface through the Windows Subsystem for Linux (WSL).

B.5 Simulation Parameters

The parameters of the simulation were constant for all simulations. A rectangular resonant cavity with a standard rectangular waveguide port was the model used. The problem was conducted at microwave frequencies centred around 2.45 GHz, covering a bandwidth of 500 MHz, from 2.2 GHz, to 2.7 GHz. The standard WR340 waveguide was used owing to the frequency range, as it is ideally used between 2.2 and 3.3 GHz. The cavity was modelled at triple the dimensions of the waveguide. The dimensions of the structure are shown in *Table B.1*. The system was modelled as PEC in a free space environment, with a waveguide port as a feed.

Table B.1: Dimensions of ideal rectangular cavity.

	Cavity	**Waveguide**
Width (mm)	259.08	86.36
Length (mm)	259.08	86.36
Height (mm)	129.54	43.18

The parameters investigated were the power radiated from the feed, the near field inside the cavity and the simulation time. The near field was investigated in terms of relative field pattern, as a 2D contour plot and a 3D iso-surface plot. This enabled an accurate measure of how similar each result was for each solver method.

Each simulation time was taken from the log files. To avoid biasing, each simulation was run on its own, with no other active applications, giving the processes primary allocation of the RAM and the CPU or GPU. For FEKO, which can solve using parallel CPU processes or GPU acceleration, the model was solved using each as a comparison. To speed up simulation times across the board, electric and magnetic symmetry planes were utilised. Additionally, in CST's frequency domain solver, adaptive mesh refinement was used.

B.6 Comparison Metrics

This section discusses which simulation metrics were compared between CST Studio and FEKO. The comparison encompassed examining three frequencies within the range: 2.2, 2.45 and 2.7 GHz. These were the upper and lower limits, and the centre frequency for the range of 2.2–2.7 GHz. An interval of 10 MHz was used for the sweep, meaning 51 data points were needed.

Additionally, the characteristic modes were simulated to evaluate the resonance of the structure. These can be determined analytically using *Equation (B.1)* [1]. These modes describe the resonant peaks of the system.

$$f_{mnl} = \frac{ck_{mnl}}{2\pi\sqrt{\mu_r\epsilon_r}} \tag{B.1a}$$

$$k_{mnl} = \sqrt{\left(\frac{m\pi}{a}\right)^2 + \left(\frac{n\pi}{b}\right)^2 + \left(\frac{l\pi}{d}\right)^2} \tag{B.1b}$$

Where:

f_{mnl} = cavity resonant frequency for mode TE_{mnl} [Hz]
k_{mnl} = wave number corresponding to mode TE_{mnl}
c = speed of light $[2.998m \times \cdot\mathrm{s}^{-1}]$
a, b, d = dimensions of the cavity [m]

And

$$\frac{1}{\sqrt{\mu_r\epsilon_r}} = 1$$

for free space problems.

Four characteristic modes are apparent in the frequency range, the first two of which, as determined in the investigation, resided at 2.3856 GHz and 2.4547 GHz. The electric field around these frequencies was also examined. As numerical anomalies can occur around resonant peaks, this investigation would serve to compare the resonance tolerance of each software.

A frequency range of 10 MHz around these points was used; 5 MHz on either side. The frequency range for mode 1 was 2.3806–2.3906 GHz, and for mode 2, 2.4497–2.4597 GHz. With a frequency step of 100 kHz, there were 101 iterations.

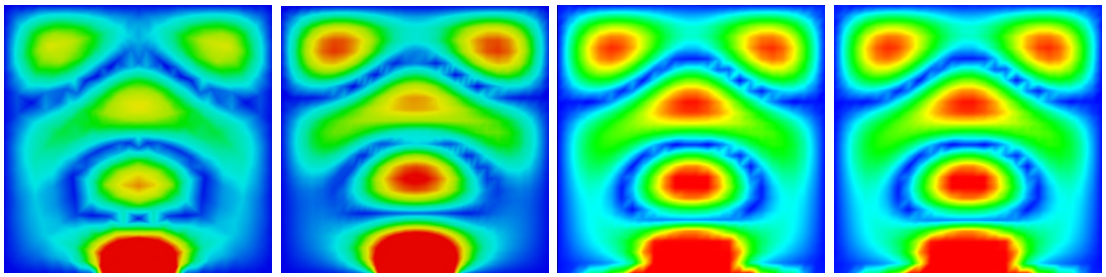

(a) CST FEM. (b) CST FIT. (c) FEKO MoM. (d) CST MLFMM.

Figure B.1: Comparison of CST Studio and FEKO at 2.2 GHz.

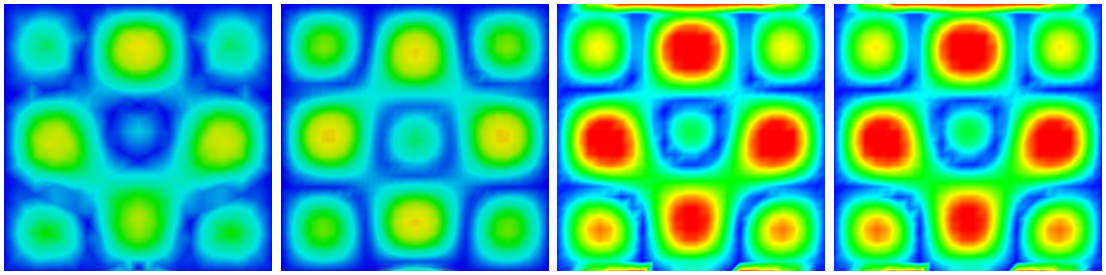

(a) CST FEM. (b) CST FIT. (c) FEKO MoM. (d) CST MLFMM.

Figure B.2: Comparison of CST Studio and FEKO at 2.45 GHz.

B.7 Solution Comparison

This section presents a comparison of the outputs from CST Studio and FEKO. The results of both the frequency sweep and the characteristic modes are examined.

B.7.1 Frequency Sweep

Initially, the 2.2, 2.45 and 2.7 GHz electric fields were examined with CST Studio's frequency and time domain solvers, and FEKO's MoM and FMM solvers. This comparison is shown in *Figures* B.1, B.2 and B.3. In CST's time domain solver, a warning was flagged that the maximum number of pulse widths had been simulated without the residual energy reaching steady state. This could imply an accuracy issue. To resolve this warning, the maximum pulses criterion was increased from 20 up to 250. This criterion then achieved the designated energy accuracy of -40 dB, but increased simulation time substantially.

Clearly, the resulting patterns from all the solvers are very similar. It was noted that in each case, FEKO's maximum field value was higher. The same field maximum was used for each program: 150 V/m for the 2.2 GHz simulations, 300 V/m for the 2.45 GHz simulations, and 500 V/m for the 2.7 GHz simulations. Both CST Studio and FEKO were set up such that average electric field was displayed. This indicated that some

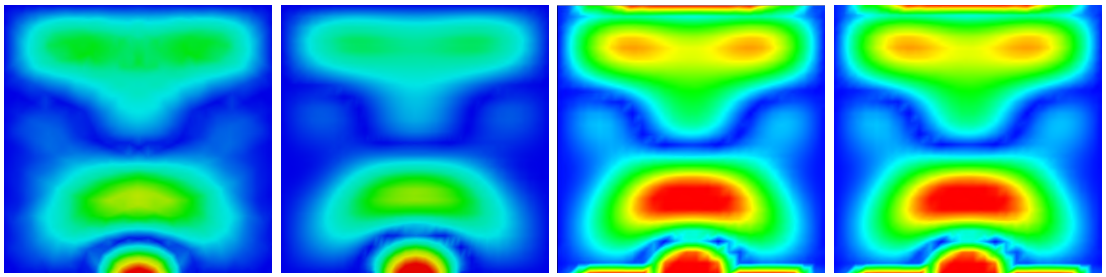

(a) CST FEM. (b) CST FIT. (c) FEKO MoM. (d) CST MLFMM.

Figure B.3: Comparison of CST Studio and FEKO at 2.7 GHz.

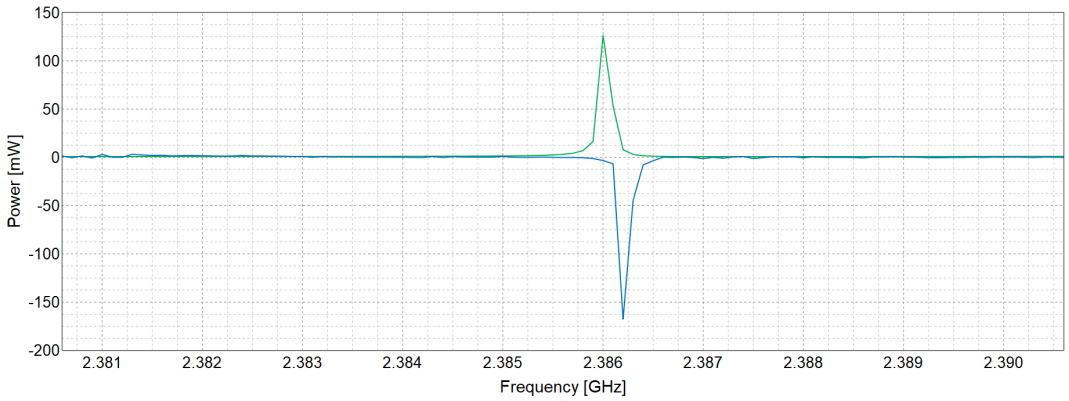

Figure B.4: Radiated Power for Mode 1 in FEKO

scaling factor was evident between the feeding mechanism of the programs. It was not possible to calculate this scaling factor as the student edition of CST Studio does not support data export, which would have been crucial in calculating the scaling factor.

B.7.2 Characteristic modes

This section presents to results of the investigation of the near field around the resonant peaks. The power and near field patterns are examined separately.

Power

Initially, the radiated power of each system was evaluated. The resonant modes were expected to present as peaks in the radiated power. This is because of the increased amplitude of the field when it is in resonance. The radiated power in FEKO for the mode 1 and mode 2 simulations are shown in *Figures* B.4 and B.5 respectively.

In both images, the green line represents the power data for the MoM solution and the blue line represents the MLFMM solution. Clearly the results are very similar. In *Figure* B.4, the MoM power spike is at 2.3860 GHz and the MLFMM spike is at 2.3862 GHz. There could be a numerical anomaly in the MLFMM data as the power

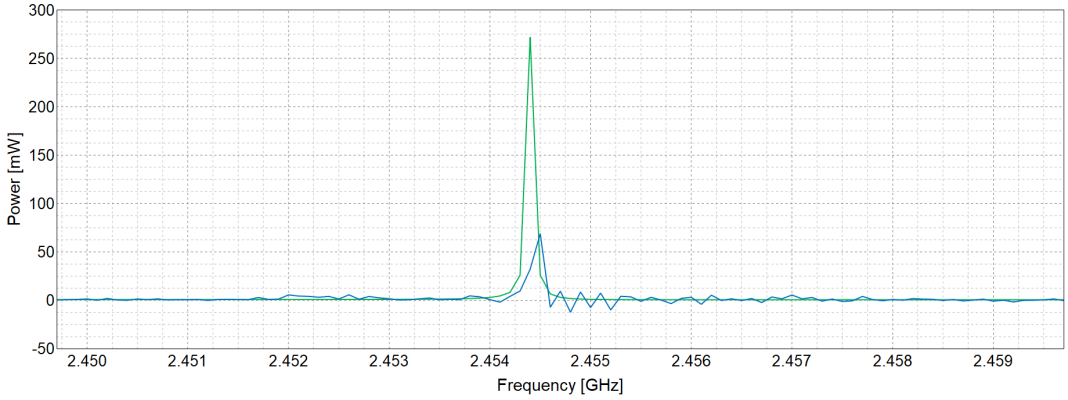

Figure B.5: Radiated Power for Mode 2 in FEKO

spike is negative. Upon inspection of the output file, a convergence error occurred at 2.3862 GHz. The solution would not converge and so the lowest residual error was selected. This could explain the negative spike. Or, the power at that frequency had a prominent reactive component, causing the overall magnitude of the power to become negative. This could also be because of convergence error.

Irrespective of the convergence warning, the resonant peak was clearly simulated very similarly by the MoM solver and the FMM solver, being only $\approx$ 200 kHz apart and only $\approx$ 400 kHz above the analytic value of 2.3856 GHz.

In *Figure B.5*, the MoM spike occurs at 2.4544 GHz and the MLFMM spike occurs at 2.4545 GHz. No warnings or convergence errors occurred in this instance. These results are very similar to each other, being only $\approx$ 100 kHz apart and $\approx$ 200 kHz below the analytically determined value of 2.4547 GHz.

The accepted power for CST Studio's frequency and time domain solvers are presented. The accepted power for mode 1 is shown in *Figure B.6*. There is a clear spike in power at 2.3867 GHz. This is well within the range of the analytically calculated mode at 2.3856 GHz, being only $\approx$ 1.1 MHz higher. It is, however, not as close as the FEKO solutions. Additionally, there appears to be some power oscillation after the actual resonant peak.

The accepted power for mode 2 is shown in *Figure B.7*. In the initial simulation, the frequency seemed too low, so the range was moved 5 MHz up. The presented range is 2.4547–2.4647 GHz. There appears to be no distinct peak. The maximum of the range is at 2.4588 GHz, and the minimum is at 2.4612 GHz. There is another peak at 2.4625 GHz. To determine where the actual resonant mode was, the near field patterns had to be examined.

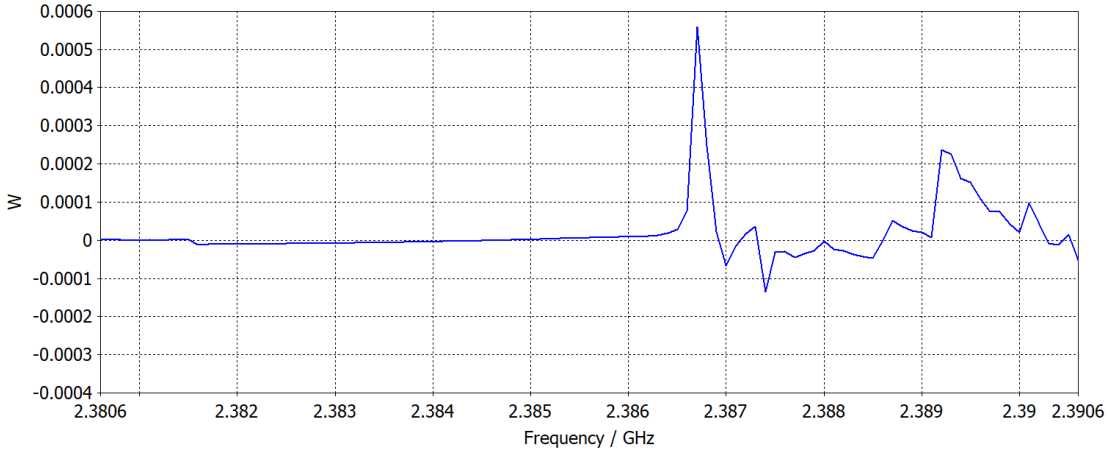

Figure B.6: Accepted Power for Mode 1 in CST

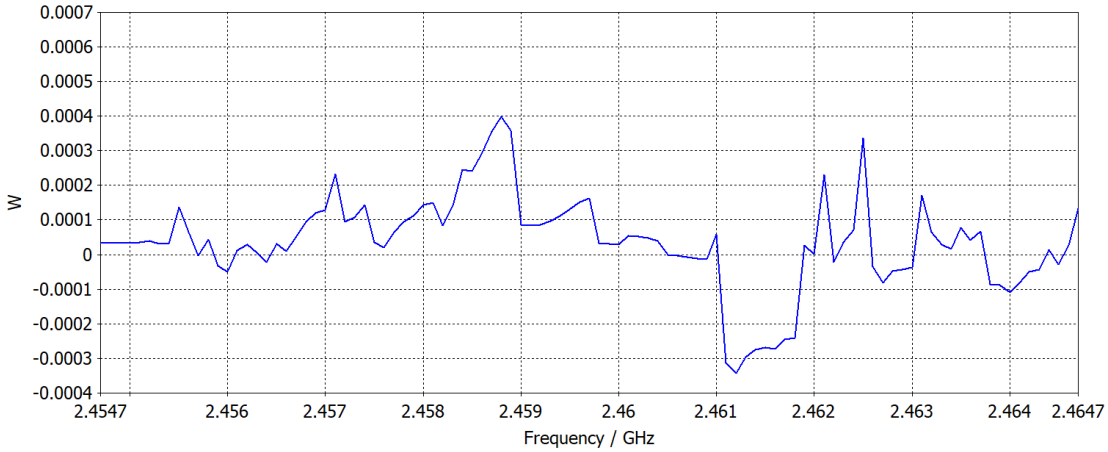

Figure B.7: Accepted Power for Mode 2 in CST

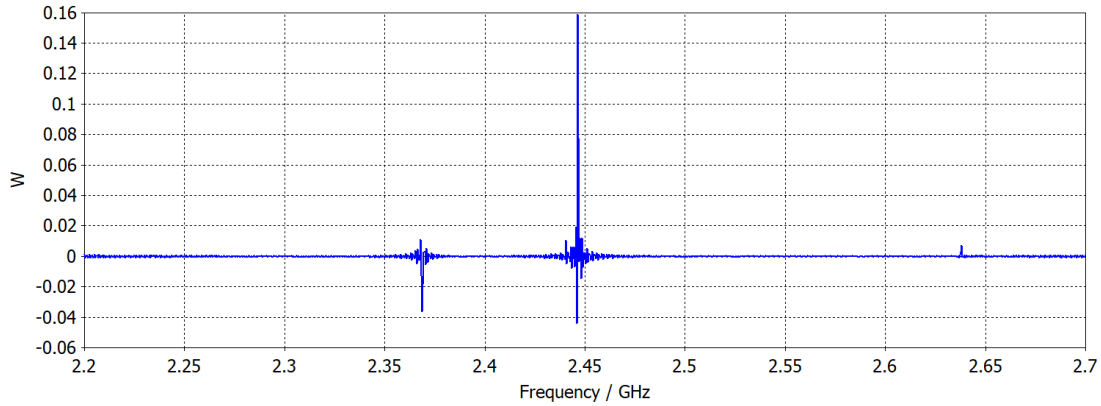

Figure B.8: Accepted Power for Time Domain Solver in CST

The accepted power calculated in the time domain simulations for both modes was identical and spanned over the full range of 2.2–2.7 GHz, as shown in *Figure B.8*. This could be a characteristic of the time domain FIT solver, as it is useful for broadband problems. Clearly there are two major spikes, one at 2.3685 GHz, and the other at 2.4465 GHz. The third mode was not evident in the simulation, nor was it evident at all throughout the investigation. The 4th mode, which analytically is expected at 2.6514 GHz was evident as a far less prominent peak at 2.6380 GHz.

The two relevant peaks were outside the initial near field simulation range, so new ranges had to be simulated. For mode 1, the simulation range moved from 2.3806–2.3906 GHz to 2.3635–2.3735 GHz. For mode 2, the simulation range was move from 2.4497–2.4597 GHz to 2.4415–2.4515 GHz. Additionally, the power plot seems to oscillate. This could be owing to the time signal used to excite the cavity. Additionally, the maximum number of pulses was again increased from 20 up to 250.

Near Field Pattern

The near field at each of the resonant peaks was examined. The frequencies corresponding with the peaks in the power plots were investigated first. Mode 1 was found in FEKO at 2.3682 GHz for the MLFMM simulation and at 2.3680 GHz for the MoM solver, as per the power spikes. This is shown in *Figure B.9*. In CST, mode 1 was found at 2.3867 GHz with the frequency domain solver and at 2.3685 GHz with the time domain solver, as as shown in *Figure B.10*. This was expected from the power plot.

All four results yielded very similar patterns, three of which were located within 500 kHz of each other. The outlier in frequency was the time domain solution as it was solved in the time domain, instead of the frequency domain like the other solvers. This was a positive results in the handling of resonance for all the solvers.

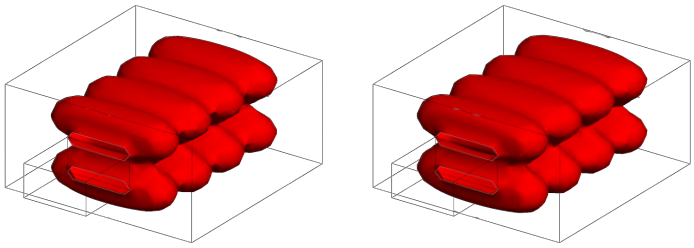

(a) MLFMM 2.3682 GHz. (b) MoM 2.3860 GHz.

Figure B.9: Near Field Pattern for Mode 1 in FEKO.

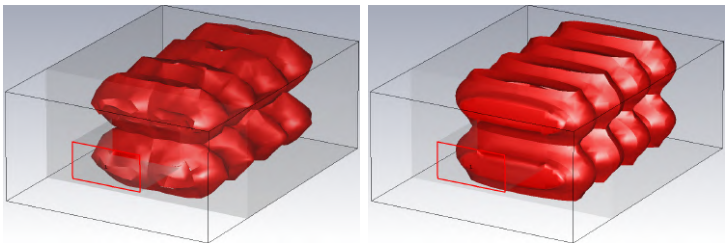

(a) FEM 2.3867 GHz. (b) FIT 2.3685 GHz.

Figure B.10: Near Field Pattern for Mode 1 in CST.

In FEKO, mode 2 was found at 2.4545 GHz with the MLFMM solver, and at 2.4544 GHz with the MoM solver, as expected. The characteristic columns of the TE_{303} mode are shown in *Figure* B.11. In CST Studio, using the time domain solver, the second mode was found at 2.4465 GHz as expected. With the frequency domain solver, as previously mentioned, there was no distinct power peak. The near field columns associated with the mode were found at 2.4554 GHz, as shown in *Figure* B.12. This corresponds to the very first peak in *Figure* B.7. It is a minor peak and not expected of a resonant mode.

All the near field patterns again were very similar. The three frequency domain solvers exhibited the resonant mode within 900 kHz of each other. Again, the time domain solution was a slightly lower frequency. Note that even though the time domain solutions were found at lower frequencies, they were always within a few MHz of the other results.

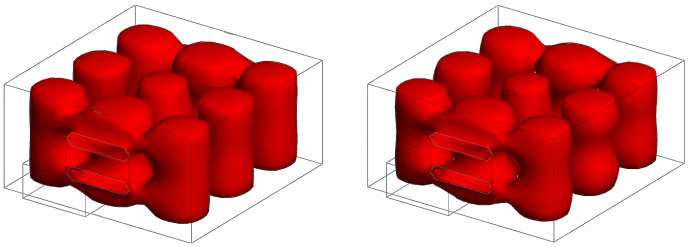

(a) MLFMM 2.4545 GHz. (b) MoM 2.4544 GHz.

Figure B.11: Near Field Pattern for Mode 2 in FEKO.

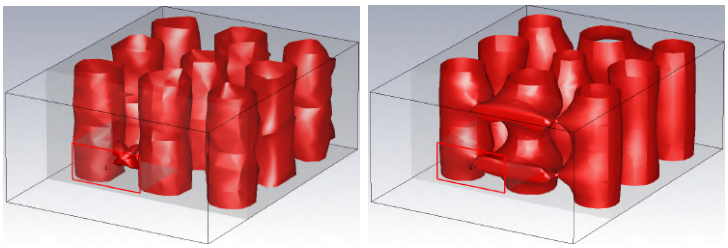

(a) FEM 2.4554 GHz. (b) FIT 2.4465 GHz.

Figure B.12: Near Field Pattern for Mode 2 in CST.

It was determined that the FEKO MoM solver was the most accurate. It relies on no iterative process, so has no convergence error or energy residuum issues. It also presented results that were closest to the analytically calculated results around the resonance of the system.

For the overall range of frequencies, all programs and solvers yielded similar results, however around resonance, FEKO's MoM solver was determined to be the most accurate in terms of the frequency of the peak. This could be explained by the fact that the MoM solver is a direct matrix solver, whereas FMM and CST's FEM use iterative processes to converge a result. This, while speeding up simulation time, does lend a small unrepeatable aspect and a degree of error as the solution is ultimately an approximation. This was particularly evident simulating mode 2, where CST's FEM solver did not display a power spike at the resonant peak.

However, the simulation band was very narrow in the modal simulations. When a broader frequency sweep was conducted with the same small interval, the results were more accurate, showing distinct peaks at all the modes. That investigation was not presented here as a uniformity of simulation parameters was desired.

Additionally, with FDTD solvers and CST's FIT solver, while the power plot was more precise than it was with the FEM solver, it was less accurate. The actual peaks were at a slightly lower frequency than expected. This could be because a time based solver simply takes a transform of a time signal response, which is evident by the oscillatory nature of the power plot. This makes the method very effective for broadband sweeps, but less so for very precise frequency intervals. However, the FIT solver did simulate the resonance patterns accurately. The patterns were aligned to the expected frequencies from the simulated power, even though the frequencies were slightly shifted.

B.8 Simulation Time

The simulation times for each solution were stored in the log file of each simulation. In the case of CST studio, the simulation time had to be calculated from the start and stop times in the log file. In FEKO, the total solver time was explicitly given. The results are tabulated in *Table B.2*.

Table B.2: Solver Times of CST Studio and FEKO.

	CST Studio		**FEKO**			
Time (s)	FEM	FIT	FMM	FMM (GPU)	MoM	MoM (GPU)
Sweep	26	92	1236.027	1608.910	3532.031	4633.558
Mode 1	57	127	2085.865		5359.777	
Mode 2	54	130	2596.062		5753.350	

In FEKO, both a parallel CPU matrix solving approach and a GPU acceleration approach are available. It was noted that the parallel CPU solution resolved faster than the GPU solution for FEKO. This was unexpected, as [2] showed significantly faster simulation times with the use of a GPU in FEKO. This could be due to a poorer GPU having been used in this investigation, or that in [2], only characteristic modal analysis (CMA) was investigated. CMA is a different solution configuration altogether. Alternatively, the GPU accelerator could have been set up incorrectly.

Because of the poor GPU performance, only the parallel CPU solver was utilised for the characteristic modes. For the FEKO results, MLFMM provided simulation times of less than half MoM solution times. CST Studio provided by far the lowest simulation times.

The FEKO solution provides electric field data, electric flux density and specific absorption rate (SAR) data. The magnetic near fields were excluded from the simulation as they weren't relevant. CST provides only electric field data. Every other parameter must be specifically requested. Both programs provide data about the feed port: reflection coefficient, VSWR, etc. Power is also stipulated by both programs, however they provide different metrics. FEKO provides only radiated power, whereas CST Studio provides loss in dielectrics, loss in metals, power accepted, power outgoing the port and power stipulated. It also provides more information about the port, such as cutoff frequency and effective dielectric constant. All these could influence simulation run time, though it is unlikely that they would influence the time as much as *Table B.2*. This suggests that the simulation in CST Studio runs far faster than that in FEKO.

B.9 Conclusion

The programs CST Studio Student Edition and FEKO both provide different solver methods to simulate near field resonance problems. The comparison of both programs has been presented. The simulation times, near field patterns, and feed power were examined.

It was determined that over a range of frequencies, CST Studio and FEKO yielded very similar results. When resonance and characteristic modes were approached in frequency, the programs exhibited different numerical tolerances.

It was found that the radiated power simulated by FEKO was the most precise and accurate, particularly with the pure MoM solver. The FMM solver didn't converge on one occasion. The time domain solver from CST proved to be very precise, but the frequencies of the modes were lower than expected. The frequency domain solver from CST Studio was precise and accurate for one of the modes, but didn't yield a clear result for the other mode.

In terms of the near field pattern itself, all the programs yielded very similar results. All exhibited the expected characteristic modal pattern.

For simulation time, CST Studio clearly yielded the lowest simulation time. The frequency domain solver was determined to be faster than the time domain solver, as the FIT pulse width had to be increased to accommodate accuracy. The GPU methods was by far the slowest and was discarded for the resonance simulations. In FEKO, it was determined that MLFMM does yield faster results, but with a potential cost to accuracy.

In conclusion, both programs have their pros and cons when simulating resonance. To achieve the best results, a fast solution could be provided by CST Studio and verified by FEKO. Both programs are viable for soving resonance problems.

References

[1] D. M. Pozar, *Microwave Engineering*, ch. 6, pp. 284–287. John Wiley & Sons, Inc., 4 ed., 2012.

[2] D. J. Ludick, E. Lezar, and U. Jakobus, "Characteristic mode analysis of arbitrary electromagnetic structures using feko," in *2012 International Conference on Electromagnetics in Advanced Applications*, pp. 208–211, Sep. 2012.

Bibliography

Alpert, Y. and E. Jerby (Apr. 1999). "Coupled thermal-electromagnetic model for microwave heating of temperature-dependent dielectric media". In: *IEEE Transactions on Plasma Science* 27.2, pp. 555–562. ISSN: 1939-9375. DOI: 10.1109/27.772285.

Arbenz, P. and R. Geus (1999). "Eigenvalue Solvers for Electromagnetic Fields in Cavities". In: *High Performance Scientific and Engineering Computing*. Ed. by Hans-Joachim Bungartz, Franz Durst, and Christoph Zenger. Berlin, Heidelberg: Springer Berlin Heidelberg, pp. 363–373. ISBN: 978-3-642-60155-2.

Bertram, John M. et al. (Feb. 2006). "Antenna design for microwave hepatic ablation using an axisymmetric electromagnetic model". In: *BioMedical Engineering OnLine* 5.1, p. 15. ISSN: 1475-925X. DOI: 10.1186/1475-925X-5-15.

Bhardwaj, N. et al. (2009). "A comparative histological evaluation of the ablations produced by microwave, cryotherapy and radiofrequency in the liver". In: *Pathology* 41.2, pp. 168–172. ISSN: 0031-3025. DOI: https://doi.org/10.1080/00313020802579292.

Bienstman, P. et al. (Feb. 2001). "Analysis of cylindrical waveguide discontinuities using vectorial eigenmodes and perfectly matched layers". In: *IEEE Transactions on Microwave Theory and Techniques* 49.2, pp. 349–354. ISSN: 1557-9670. DOI: 10.1109/22.903096.

Birla, Sohan et al. (Jan. 2010). "Effect of Magnetron Frequency on Heating Pattern in Domestic Oven". In: *International Microwave Power Institute's 44th Annual Symposium*.

Eleftheriades, G.V. et al. (Oct. 1994). "Some important properties of waveguide junction generalized scattering matrices in the context of the mode matching technique". In: *IEEE Transactions on Microwave Theory and Techniques* 42.10, pp. 1896–1903. ISSN: 1557-9670. DOI: 10.1109/22.320771.

Jakobus, U. et al. (Dec. 2008). "Tailoring FEKO for microwave problems". In: *IEEE Microwave Magazine* 9.6, pp. 76–85. ISSN: 1557-9581. DOI: 10.1109/MMM.2008.929557.

Ludick, D. J., E. Lezar, and U. Jakobus (Sept. 2012). "Characteristic mode analysis of arbitrary electromagnetic structures using FEKO". In: *2012 International Conference on Electromagnetics in Advanced Applications*, pp. 208–211. DOI: 10.1109/ICEAA.2012.6328622.

Monteiro, J. et al. (Oct. 2011). "Simulating the electromagnetic field in microwave ovens". In: *2011 SBMO/IEEE MTT-S International Microwave and Optoelectronics Conference (IMOC 2011)*, pp. 493–497. DOI: 10.1109/IMOC.2011.6169274.

Raj, John et al. (Feb. 2020). "Modeling of Microwave Heating of a Rotating Object in Domestic Oven". In: URL: https://www.researchgate.net/publication/268393048_Modeling_of_Microwave_Heating_of_a_Rotating_Object_in_Domestic_Oven.

Santos, T. et al. (Nov. 2010). "3D Electromagnetic Field Simulation in Microwave Ovens: a Tool to Control Thermal Runaway". In.

Schena, Emiliano et al. (July 2016). "Fiber Optic Sensors for Temperature Monitoring during Thermal Treatments: An Overview". In: *Sensors* 16, p. 1144. DOI: 10.3390/s16071144.

Shamis, Yury et al. (Mar. 2011). "Specific Electromagnetic Effects of Microwave Radiation on Escherichia coli". In: *Applied and environmental microbiology* 77, pp. 3017–22. DOI: 10.1128/AEM.01899-10.

Singhal, Ankur et al. (Apr. 2019). "Approach for Efficiency Enhancement of Microwave Ovens". In: *International Journal of Advanced Trends in Computer Science and Engineering* 8, pp. 265–270. DOI: 10.30534/ijatcse/2019/27822019.

Stutzman, Warren L. and Gary A. Thiele (2013). "Antenna Theory and Design". In: 3rd ed. John Wiley & Sons, Inc. Chap. 11, pp. 465–536. ISBN: 978-0-470-57664-9.

Warren, Craig et al. (Jan. 2017). "Comparison of time-domain finite-difference, finite-integration, and integral-equation methods for dipole radiation in half-space environments". In: *Progress In Electromagnetics Research M* 57, pp. 175–183. DOI: 10.2528/PIERM17021602.